TABLE OF CONTENTS

Section		Page	
I.	INTRODUCTION	1	1/A14
II.	(AlGa)As LASERS	3	1/B2
	A. Introduction	3	1/B2
	B. Material Properties	4	1/B3
	1. Electroreflectance Studies of Macroscopic Nonuniformities	4	1/B3
	2. Cathodoluminescence Study of Microscopic Nonuniformities	4	1/B3
	C. Analysis of Stripe Configuration	16	1/C1
	D. Laser Diode Properties	17	1/C2
	E. Reliability	23	1/C8
	1. Longer-Wavelength Lasers	23	1/C8
	2. Shorter-Wavelength Lasers	25	1/C10
III.	RED-EMITTING Ga(AsP)/(InGa)P HETEROJUNCTION LASERS	32	1/D3
	A. Introduction	32	1/D3
	B. Structures	32	1/D3
	C. Device Evaluation	35	1/D6
	1. Current-Voltage Characteristics	35	1/D6
	2. Spontaneous Carrier Lifetime	40	1/D13
	3. Spontaneous Emission	41	1/D14
	4. Pulsed Laser Characteristics	42	1/E1
	5. CW Laser Operation	46	1/E5
	D. Discussion	48	1/E7
IV.	LONG-WAVELENGTH (InGa)(AsP) QUATERNARY LASERS	52	1/E12
	A. Introduction	52	1/E12
	B. LPE Growth Technique	52	1/E12
	1. Lattice Mismatch	54	1/E14
	2. InP Substrate Dissociation	56	1/F2
	3. Indium Carry-Over	58	1/F4
	C. Contacts	61	1/F7
	D. Device Properties	61	1/F7
	1. General Properties	61	1/F7
	2. Temperature Dependence of Laser Characteristics	64	1/F10
	E. Reliability	70	1/G2
V.	CONCLUSIONS	72	1/G4
REFERENCES		74	1/G6
APPENDIXES			

NAS 1.26 3045

NASA Contractor Report 3045

COMPLETED
ORIGINAL

1.1 Micrometer and Visible Emission Semiconductor Diode Lasers

I. Ladany, C. J. Nuese, and H. Kressel

CONTRACT NAS1-14349
OCTOBER 1978

NASA

12

NAS 1.26:3045

NASA Contractor Report 3045

1.1 Micrometer and Visible Emission Semiconductor Diode Lasers

I. Ladany, C. J. Nuese, and H. Kressel
RCA Laboratories
Princeton, New Jersey

Prepared for
Langley Research Center
under Contract NAS1-14349

NASA
National Aeronautics
and Space Administration

**Scientific and Technical
Information Office**

1978

Blank Page

PREFACE

This final report covers the work performed at RCA Laboratories during the period January 1, 1977 to November 30, 1977 under contract No. NAS1-14349. The Laboratory Director is H. Kressel, the Group Head is C. J. Nuese, and the Project Scientist is I. Ladany. Staff members and support personnel who have contributed to this report, in addition to the authors, and the area of their contribution are listed below.

T. R. Furman	-	(AlGa)As growth, device fabrication,
D. P. Marinelli	-	device studies
G. H. Olsen*	-	VPE growth of Ga(AsP)/(InGa)P,
T. J. Zamerowski	-	materials studies
F. Hawrylo	-	LPE growth of (InGa)(AsP), device
M. Harvey	-	fabrication
M. Ettenberg*	-	Device characterization, lifetests
D. Gilbert	-	
A. Kan	-	
E. R. Levin*	-	Cathodoluminescence studies
J. T. McGinn	-	TEM studies

*Member Technical Staff

Blank Page

SUMMARY

The (AlGa)As, Ga(AsP), and (InGa)(AsP) alloy systems have been investigated with the objective of extending laser operation to both shorter (visible) and longer (infrared) wavelengths than those provided by generally available (AlGa)As lasers (~0.8 μm). In the (AlGa)As system, cw operation at room temperature has been obtained at a wavelength of 7260 Å, which is the shortest value yet reported for this system. The reliability of such short-wavelength devices has been studied for diodes operating in the incoherent mode. It was found that zinc-doped diodes had significant degradation, while germanium-doped devices showed none. Since zinc doping was found to be essential for successful operation, a combination of the two dopants, Zn and Ge, was investigated. It was found that devices containing both dopants also showed no degradation, the Ge acting to suppress the deleterious influence of Zn. A discussion is given of the implication of these results on short-wavelength (AlGa)As devices.

For longer-wavelength diodes of (AlGa)As ($\lambda \sim 0.8$ μm), a facet coating of Al_2O_3 was shown to significantly improve the reliability by eliminating facet damage. Coated lasers show little degradation for 22,000 hours, so far, and require no periodic increases in operating current to maintain stable output. Uncoated lasers in a controlled ambient have accumulated about 28,000 hours of life to date, although an appreciable decrease in output has occurred.

In order to extend the capability of (AlGa)As, several material and structural parameters were examined in detail. A study of materials inhomogeneity in (AlGa)As showed, in addition to larger scale variations, a microscopic system of small patches (6-20 μm) corresponding to a fluctuation in composition of about 1 mole percent. Because of its importance to laser devices fabricated here, an experimental and theoretical study was carried out to determine the effect of stripe width, threshold current and p-layer doping, on the threshold current of oxide-isolated stripe-contact (AlGa)As lasers. Good predictions were obtained for stripe widths down to 6-8 μm; for narrower stripes, a rapid increase in threshold current was found to occur, which was not consistent with any present calculations.

Emission at wavelengths of 7000 Å and below was obtained in double-heterojunction laser structures of Ga(AsP)/(InGa)P prepared by vapor-phase

epitaxy. Thorough material and device studies were carried out, and showed no evidence of misfit dislocations introduced during growth, very good alloy uniformity, and a spontaneous carrier lifetime in the 5-8 ns range (comparable to what is obtained in the (AlGa)As system at 8000 Å). At 6800 Å, a threshold current density of 6.6 kA/cm^2 was obtained, and at 7000 Å this dropped to 3 kA/cm^2. CW operation was obtained at 10°C at 7000 Å; however, rapid facet damage was seen in uncoated units. In the incoherent mode the operating life was found to be moderate, 2000 hours having been accumulated to date.

For long-wavelength laser operation, exploratory research was carried out in the quaternary (In,Ga)(As,P) system using liquid-phase expitaxy. Growth techniques, problems of In pullover, substrate dissociation, and reduction of misfit dislocations were evaluated, and are discussed. A new contact process based on Au-Ge-Zn alloys has been developed. LEDs made from this material had a total output efficiency of 2%. The lowest lasing threshold current was 5 kA/cm^2 at 1.11 μm, while differential quantum efficiencies as high as 36% were obtained from one facet. Only incoherent lifetests were made, but for the presently available times of 6000 hours, most of the diodes show no degradation.

LIST OF ILLUSTRATIONS

Figure		Page
1.	(a) SE- and (b) CL-images of same region of Ge-doped $Al_{.23}Ga_{.68}As$ layer	7
2.	Y-modulation CL-line scans in field of Fig. 1. Scale of relative CL efficiency is shown for upper trace	8
3.	CL distribution in Zn-doped layer	9
4.	(a) SE- and (b) CL-images of Te-doped layer	10
5.	(a) SE- and (b) CL-images of cleaved edge of specimen containing 4 thick, graded (AlGa)As layers, (c) Y-modulation CL-line scan in same region	12
6.	Comparison of electron probe data and SEM CL-efficiency for sample containing 4 graded (AlGa)As layers	13
7.	Variation of CL-efficiency of $Al_xGa_{1-x}As$ with mole fraction of Al(x)	13
8.	Calculated internal quantum efficiency as a function of x, the mole fraction of Al in (AlGa)As. (The L minima are neglected in this calculation.)	16
9.	Ratio of stripe laser threshold current to broad-area laser threshold current for oxide-isolated stripe lasers. These curves are obtained from calculations that take account of carrier-out diffusion and current leakage, but neglect optical absorption. x_o is defined by $\frac{mkT}{R_s J_o q}$ where $m \sim 2$, R_s is the p-layer sheet resistivity, and J_o is the broad-area threshold current density	18
10.	Mobility in (AlGa)As as a function of x, the mole fraction of Al, for a fixed acceptor concentration	18
11.	Typical stripe laser configuration	19
12.	The required Al fraction, x, in the confining (heterojunction) regions and in the recombination region in order to provide low threshold lasing at the indicated wavelength	19
13.	Emission spectrum of a short-wavelength cw laser	20
14.	Power vs current characteristic of a short-wavelength laser	21
15.	Far-field pattern of same laser as that used in Figs. 5, 13 and 14	21
16.	Temperature dependence of emission energy and threshold current for the laser described in Figs. 13, 14 and 15	22
17.	Reflectivity as a function of t/λ_o where t is the film thickness and λ_o is the wavelength in air. The solid curve shows the calculated reflectivity, assuming n = 1.72 for Al_2O_3 and n = 3.6 for GaAs	24

LIST OF ILLUSTRATIONS

Figure		Page
18.	Lifetests of coated diodes for constant current operation. Performance of an uncoated diode, maintained in a protected dry ambient, is also shown	25
19.	Incoherent normalized life test data of two groups of Ge-doped diodes. The solid lines show time-smoothed average values, whereas the shaded portion defines the region between the diodes with the highest and the lowest outputs. The emission energy is indicated in the figure	28
20.	Same data as in Fig. 19, for three groups of zinc-doped diodes	28
21.	Same data as in Figs. 19 and 20, for two groups of diodes doped with zinc and germanium	29
22.	TEM of a high-Al laser structure	31
23.	Room-temperature energy-bandgap values of $GaAs_{1-x}P_x$ and $In_yGa_{1-y}P$ for lattice-matched structures	33
24.	(a) Cross-sectional representation of structure used to prepare low-threshold Ga(AsP)/(InGa)P heterojunction lasers. (b) (100) clevage plane cross-section of Ga(AsP)/(InGa)P vapor-grown laser structure. Thickness of Ga(AsP) recombination region is 0.22 μm, in agreement with the same value derived from capacitance-voltage measurements on this sample	34
25.	Cross-sectional transmission electron micrograph of Ga(AsP)/(InGa)P heterojunction laser. Absence of misfit dislocations is due to lattice-matching alloy compositions used here	36
26.	Auger SIMS scans of In, Ga, As, and P through the 3000 Å-thick $GaAs_{0.62}P_{0.38}$ recombination region and the $In_{0.31}Ga_{0.69}P$ confining layers of vapor-grown double-heterojunction laser structure	37
27.	Current-voltage characteristic of 7000 Å Ga(AsP)/(InGa)P heterojunction laser diode at ambient temperatures of 300, 313 and 330 K. Values of A_o and J_o are given in Table 1	38
28.	Carrier lifetime determined by luminescence decay measurements vs $(1/J)^{1/2}$. Slope of curves near origin yield value of radiative recombination coefficient B_r, as indicated in Eqs. (2) and (3)	41
29.	Emission spectra from 6800 Å laser at room temperature for several different values of current density	42
30.	Laser spectra of 6800 Å laser at ambient temperature of 22, 40 and 70°C	43
31.	Temperature dependence of laser emission energy for 6800 and 7000 Å heterojunction lasers. Slope value, $\Delta h\nu/\Delta T = -5.7 \times 10^{-4}$ eV/K	44

Figure		Page
32.	Total power emission (from both facets) vs pulsed current amplitude for representative high quality 6800 and 7000 Å lasers at room temperature	45
33.	Temperature dependence of threshold current density and differential quantum efficiency for 6800 and 7000 Å Ga(AsP)/(InGa)P heterojunction lasers	45
34.	Power emitted as a function of current for a double-heterojunction Ga(AsP)/(InGa)P laser operating pulsed and cw at a heat sink temperature of 10°C	47
35.	Relative light output vs operating time of four Ga(AsP)/(InGa)P heterojunction diodes operating between 2500 and 5000 A/cm^2 at room temperature. Emission was monitored from one edge of the stripe-contact diodes (13 μm stripe width)	47
36.	Cross-sectional (011) TEM micrograph of Ga(AsP)/(InGa)P heterojunction structure tilted to <111> to accentuate vacancy loops due to phosphorus dissociation during crystal growth	50
37.	LPE growth technique using a multiple-bin graphite boat with sliders	53
38.	Graph depicting epitaxial growth process	53
39.	(InGa)/(AsP) quaternary alloys. Lattice constants are shown by dashed lines	54
40.	X-ray topograph showing misfit dislocations between InP confining layers and the InGaAsP recombination region	55
41.	Lattice-mismatch dislocation arrays delineated with A-B etchant	56
42.	InP substrate dissociation (a) and (c): 66X; (b) and (d): 825X. (1 hr at 670°C in H_2)	57
43.	Reduced dissociation with InP substrate covered (30 min at 650°C in H_2). Magnification: 1120X	58
44.	InGaAsP layers shown in x-ray topograph (b). "Worm-like" tracks cannot be observed under normal optical microscopy (a)	59
45.	Surface appearance of an undissociated substrate passed through In "wipe" melt for 20 s	60
46.	Typical forward-bias I-V characteristic for a standard (InGa)(AsP)/InP heterojunction structure 1 mA/div. vertical; 200 mV/div. horizontal	61
47.	Schematic representation of lattice-matched heterojunction laser structure using quaternary (InGa)(AsP) active layer and InP confining layers	62
48.	<110> cross-section of (InGa)(AsP)/InP LPE laser structure delineated with A-B etch	63

LIST OF ILLUSTRATIONS (Continued)

Figure | Page

49. Emitted power from one edge of a spontaneous emitter (LED) as a function of drive current 63

50. (a) Power-current dependence for the 5000 A/cm^2 laser. (b) Longitudinal mode structure from the 5000 A/cm^2 laser 66

51. Lateral and transverse far-field patterns of sample 829 67

52. (a) Ratio of J_{th} at 70°C to that at 0°C for (InGa)(AsP)/InP laser at 1.1 μm. (b) Ratio of η at 70°C to that at 0°C for the same (InGa)(AsP)/InP laser 68

53. (a) Ratio of threshold current at 70°C to that at 22°C for (AlGa)As heterojunction lasers vs the magnitude of the composition step. Data with error bars are from Goodwin, et al., as the ratio between 65 and 10°C. (b) Ratio of laser efficiency at 70 and 22°C for (AlGa)As heterojunction 68

54. Ratio of laser threshold current at 70 and 22°C for (InGa)(AsP)/InP double-heterojunction lasers vs the room-temperature emission wavelength. The curve is based on experimental observations of such ratios for (AlGa)As/GaAs lasers 69

55. Life test results on (InGa)(AsP)/InP LED's 70

56. Life tests on another (InGa)(AsP)/InP wafer. Diodes operated as LEDs 71

LIST OF TABLES

Table		Page
1.	Characteristics of $Al_xGa_{1-x}As$ LPE specimens	5
2.	Characteristics of Diodes Used in Incoherent Life Tests	26
3.	Heterojunction Current-Voltage Characteristics	39
4.	LPE (InGa)(AsP)/InP Lasers	65

SECTION I

INTRODUCTION

This report describes research at RCA Laboratories that was devoted to the extension of laser diode technology toward both shorter and longer wavelengths than those presently available with conventional (AlGa)As lasers ($\lambda \sim 0.75$ to 0.9 μm). The goal of shorter-wavelength operation was approached through increased Al concentrations in (AlGa)As alloys grown by LPE (Liquid-Phase Epitaxy), as well as through the development of vapor phase epitaxially (VPE) grown Ga(AsP)(InGa)P heterojunction lasers. For longer wavelengths ($\lambda > 1.0$ μm), quaternary heterojunction structures of (InGa)(AsP)/InP were grown by LPE.

Several new developments have resulted from the work under this contract. In the (AlGa)As system, cw operation has been obtained to wavelengths as short as 7260 Å at room temperature, although with an unsatisfactory operating life so far. Exploration of the reasons for this has led to the identification of a new degradation mode, which does not appear in lasers designed for 8000-8700 Å. Structures were prepared to eliminate this degradation mode, and their success has been demonstrated experimentally.

A comprehensive study was carried out of the threshold dependence of oxide-defined stripe-contact lasers on stripe width. Design formulas were obtained relating the threshold current to the stripe width, doping of the p-type layers under the stripe, and the broad-area threshold current density.

A study also was made of the homogeneity of (AlGa)As layers using two different techniques. Variations of alloy composition were found on a scale of 6-20 μm; in addition, more gradual, and larger scale variations also exist.

Although the further development of (AlGa)As lasers can satisfy many short-term and long-term optoelectronic applications, some significant advantages can be gained by developing laser and LED sources that operate at wavelengths larger than that obtainable with (AlGa)As. In particular, silica fibers, of wide interest for optical fiber communications, have lower attenuation, reduced pulse dispersion, and increased radiation hardness at wavelengths between 1.1 and 1.3 μm. For this reason, alloys of (InGa)(AsP), lattice-matched to InP substrates, were used to prepare heterojunction lasers and LEDs. The

development of the LPE growth technology for these structures and the characteristics of the devices so prepared, are discussed in detail in the final technical sections of this report.

SECTION II

(AlGa)As LASERS

A. INTRODUCTION

RCA Laboratories has been engaged in research on (AlGa)As lasers for a number of years. A part of this effort has been supported by NASA Langley Research Center, in particular, improved reliability and the efforts concerning the improvement in technology and the extension of emission wavelengths toward the visible region of the spectrum. In the paragraph below we briefly summarize state of our technology at the beginning of the present effort, as reported in previous NASA Contract reports.

In order to reduce the emission wavelength, the prime requirement is to increase the Al concentration in the recombination region and in the two adjoining layers. This makes it more difficult to obtain adequate conductivity with the usual dopants, Ge and Sn, and has led to their replacement by Zn and Te, respectively.

The standard configuration used in our devices is based on the oxide-isolated stripe, both because of its simplicity and because of its demonstrated long life at the most widely used wavelengths ($\lambda \gtrsim 8000$ Å). It is well known that the threshold current density of stripe lasers generally exceeds that of a broad-area diode, made from the same wafer, by a factor of at least 2 to 3. In previous reports we had attempted to account for this effect solely on the basis of current leakage at the stripe edges, but agreement with experiment was not good.

The effect of the direct-indirect bandgap cross-over on laser threshold was investigated, and it was concluded that cw operation into the 7200-7300 Å range should be possible. CW operation was obtained to wavelengths as short as $\sim$ 7400 Å. The "vertical" laser design requirements were developed, yielding threshold current dependence on cavity dimensions, refractive index step and emission wavelength.

In the following sections, we report on the work done and progress attained in various areas in the course of the present contract.

B. MATERIAL PROPERTIES

Although the characteristics of (AlGa)As heterojunction lasers are adequate for many applications, it had been noticed in the past that laser materials were not entirely uniform in all of their properties. For example, diodes from the same wafer do not have identical behavior; moreover, this nonuniformity becomes more severe as the Al concentration is increased for the shorter-wavelength devices. We therefore decided to investigate the microscopic and macroscopic fluctuations in uniformity of typical (AlGa)As layers.

1. Electroreflectance Studies of Macroscopic Nonuniformities

One technique, pursued at the Belfer Graduate School of Science under subcontract to RCA, was based on electrolyte electroreflectance. With a sensitivity to composition change of $\Delta x = 0.002$ and a spatial resolution of 100 μm, wafers were scanned to obtain contour maps of alloy composition. A full report of this study is included in Appendix A, where it can be seen that the wafer surface consists of large, fairly uniform regions, bordered by areas where the composition changes by about 2 mole percent over a few tenths of millimeters.

To characterize *microscopic* nonuniformities in our liquid-phase epitaxial (LPE) layers, a cathodoluminescence study in the scanning electron microscope (SEM) was carried out at RCA Laboratories (in collaboration with E. R. Levin). The following section describes this work in detail.

2. Cathodoluminescence Study of Microscopic Nonuniformities

Cathodoluminescence (CL) is known to be a very sensitive function of III-V alloy properties [1-6], and we therefore have employed CL observations

---

1. A. Onton, M. R. Lorenz, J. M. Woodall and R. J. Chicotka, J. Cryst. Growth 27, 166 (1974).
2. D. B. Holt, in *Quantitative Scanning Electron Microscopy*, D. B. Holt, M. D. Muir, P. R. Grant and I. M. Boswarva, eds. (Academic Press, New York, 1974), Chapter 10.
3. D. F. Kyser and D. B. Wittry, in *The Electron Probe*, T. D. McKinley, K.F.J. Heinreich and D. B. Wittry, eds. (Wiley & Sons, New York, 1964), p 691; D. F. Kyser and D. B. Wittry, J. Appl. Phys. 35, 2439 (1966).
4. D. B. Wittry, Appl. Phys Lett. 8, 142 (1966).
5. H. C. Casey, J. Electrochem. Soc. 114, 153 (1967).
6. H. Johansen and F. B. Herrmann, Kristall u. Technik 7, 1135 (1972).

in scanning electron microscopy to study a group of thin LPE layers of (AlGa)As alloys.

The material was grown using our standard multiple-bin [7] LPE technique. In this process, it is possible that one melt may contaminate the next, thus causing the growth of multilayered structures with slight variations in alloy composition. This problem was avoided in the present work by studying principally wafers containing only a single LPE layer, grown from a boat with only one (AlGa)As solution. However, it has been convenient for calibration purposes to also employ one wafer containing several (AlGa)As LPE layers, grown in a multiple-bin boat. The specimen parameters are summarized in Table 1. All values of x were determined by electron probe microanalysis (EPMA).

TABLE 1. CHARACTERISTICS OF $Al_xGa_{1-x}As$ LPE SPECIMENS

	Single Layers	4-Layer Specimen
Layer Thickness (Nominal)	1 μm	9 μm
Substrate Doping	Cr	Si
Layer Doping	Ge, Te or Zn $\approx 10^{18}/cm^3$	Te $\approx 10^{18}/cm^3$
Avg. Mole Fraction Al (x)	0.32 - 0.47	0.22 - 0.30

Observations were made on a Cambridge Instrument Company, Model S4-10 scanning electron microscope, equipped with the Cambridge CL detector. In the CL-mode, the total (integrated) CL output was utilized. The CL signal was not spectrum analyzed. A photomultiplier (PM) tube with GaAs photocathode (RCA Type C31034) was employed for most of these observations. This PM has a flat spectral response over a wide range of wavelengths extending through the visible and into the near IR. Thus, the intensity of the total CL signal could be utilized as an experimental parameter, even though the CL emission peak varies with specimen composition [1] from about 7500 Å for $x \lesssim 0.22$ to about 6700 Å for $x \lesssim 0.34$. Some qualitative CL observations also were made with an S1 photocathode (RCA PM Type 7102), which has a response that

7. H. F. Lockwood and M. Ettenberg, J. Cryst. Growth 15, 82 (1972).

varies considerably over the spectral range of interest, but extends farther into the IR. In both cases, the photocathodes were cooled, the C31034 to -50°C, and the 7102 to -100°C, to optimize the red response [8] and to reduce dark current and noise.

To obtain measurements of the CL intensity, the beam was line-scanned across the specimen, and the CL signal displayed in "Y-modulation", i.e., with the CL intensity shown as a vertical (Y) displacement rather than a brightness modulation on the CRT face. Since the principal interest in this work was in comparing intensities at different points of nonuniform distributions, all CL-intensity measurements were made on a relative basis, i.e., with one point of a specimen selected as a reference. Generally, no attempt was made to measure or compare "absolute" intensity levels.

Figure 1 shows SE- and CL-images of a Ge-doped layer of $Al_{.32}Ga_{.68}As$. The CL-image exhibits a distribution of small, irregularly-shaped regions of alternating bright and dark contrast, with distances between successive maxima (or minima) generally in the range 6-20 μm. The surface contains a number of clearly-definable features, including an extended system of growth steps. However, these physical features do not correlate with the CL fluctuations: the growth steps do not coincide with boundaries of the bright areas, and the small round features are all but lost in the larger-area CL variations. The dark line AB is a defect not readily discernible in SE contrast.

In Fig. 2 the CL-intensity distribution along two horizontal lines of Fig. 1 is displayed in Y-modulation. In the upper trace, the intersection of the scan line (AC) and the dark feature (AB) is marked by a sharp minimum in CL intensity at A. It can be seen that the local CL intensity variations represent peak-to-peak excursions of about 10% in CL efficiency.

Some variations in CL efficiency within the substrates were observed, as has been reported.[2] However, these changes are more gradual and occur over much larger distances than the local fluctuations in Fig. 1. Thus the small-area variations must be associated with the LPE layers and not with the substrate material. CL contrast variations somewhat similar to the effects in the LPE layers have been observed [3] in Czochralski- and float zone-grown

8. M. Cole and D. Ryer, Electro-Optical Systems Design, 6/72, p 16-19.

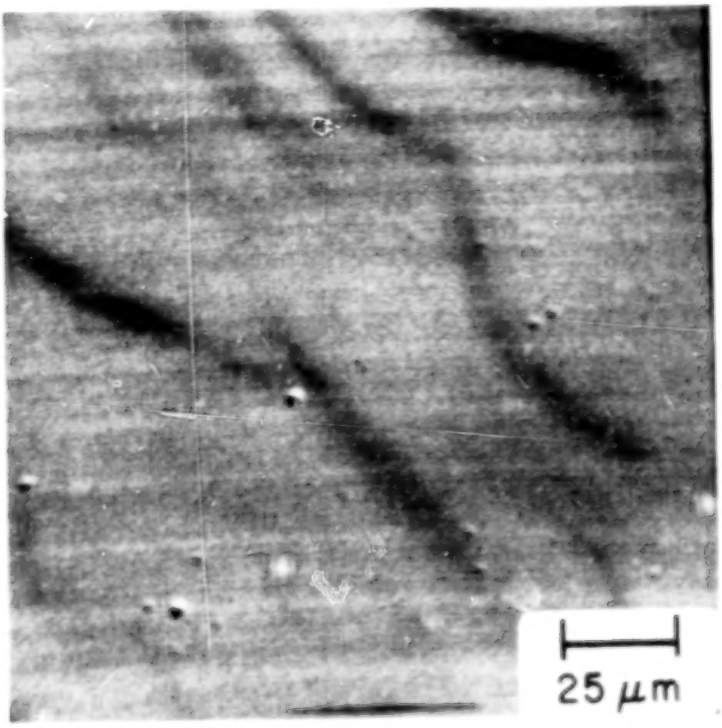

(a)

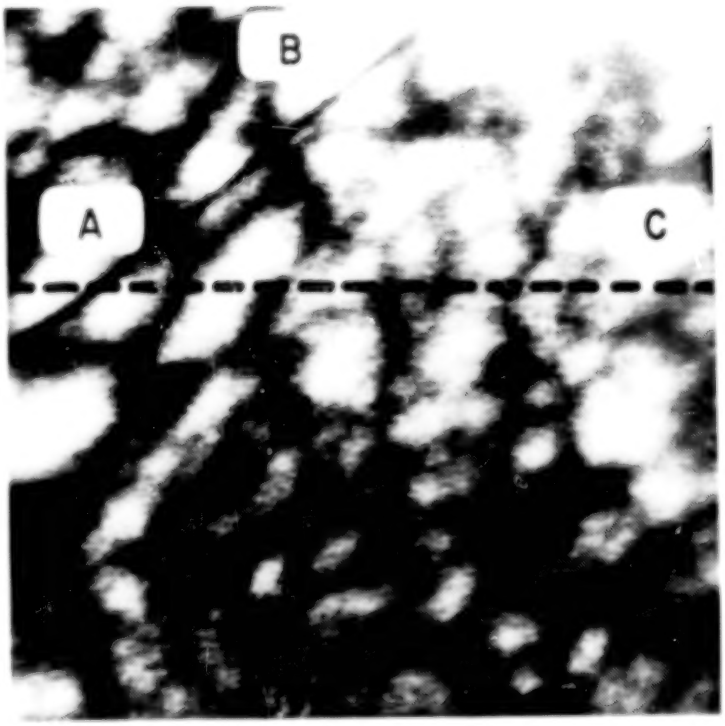

(b)

Figure 1. (a) SE- and (b) CL-images of same region of Ge-doped $Al_{.23}Ga_{.68}As$ layer.

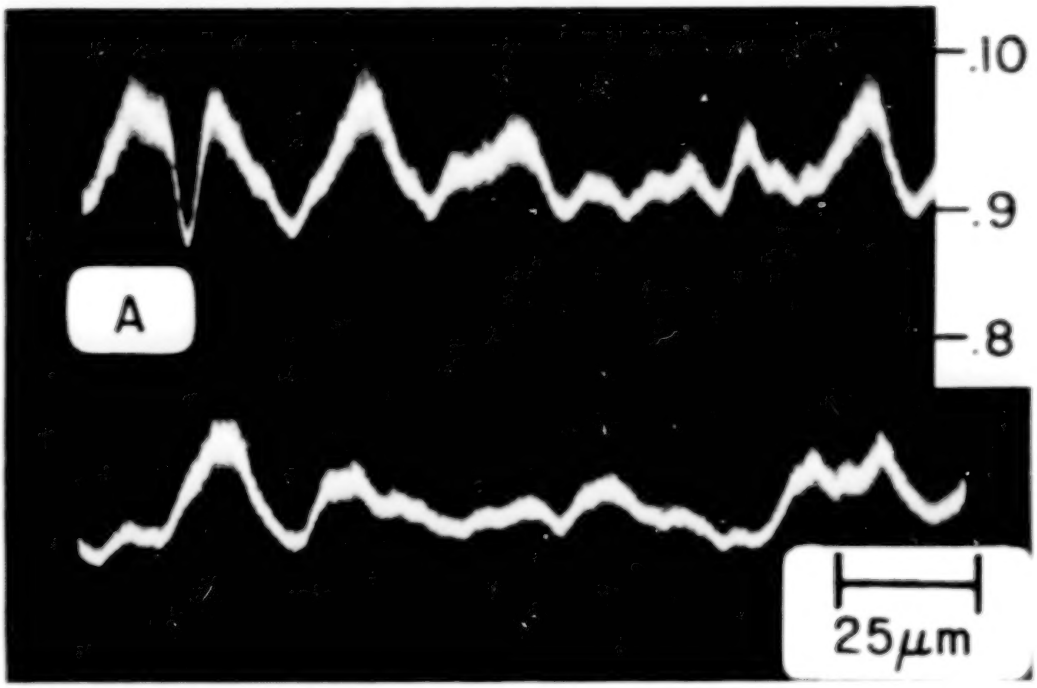

Figure 2. Y-modulation CL-line scans in field of Fig. 1. Scale of relative CL efficiency is shown for upper trace.

Te-doped GaAs crystals, but these variations, too, are over generally larger spacings.

Observations also were made on layers grown in the same way as the specimen of Fig. 1, but with Te or Zn instead of Ge used as the dopant impurity. CL maps of Zn-doped sample and a Te-doped sample are shown in Fig. 3 and 4, respectively. The similarity of the three Figs. (1, 3, and 4) is obvious. This suggests that the CL fluctuations are not caused by the deliberately-introduced impurity, which changes from specimen to specimen. Moreover, for the fluctuations to be due to the dopant, all three samples not only would have had to encounter similar perturbations during growth, but also would have required the action of a process independent of the identity, the position in the host lattice, and the segregation coefficient of the dopant. In the case of Zn doping, diffusion is rapid at the growth temperature and the contrast patches should be smoothed out compared to the other two dopants. This behavior is not observed.

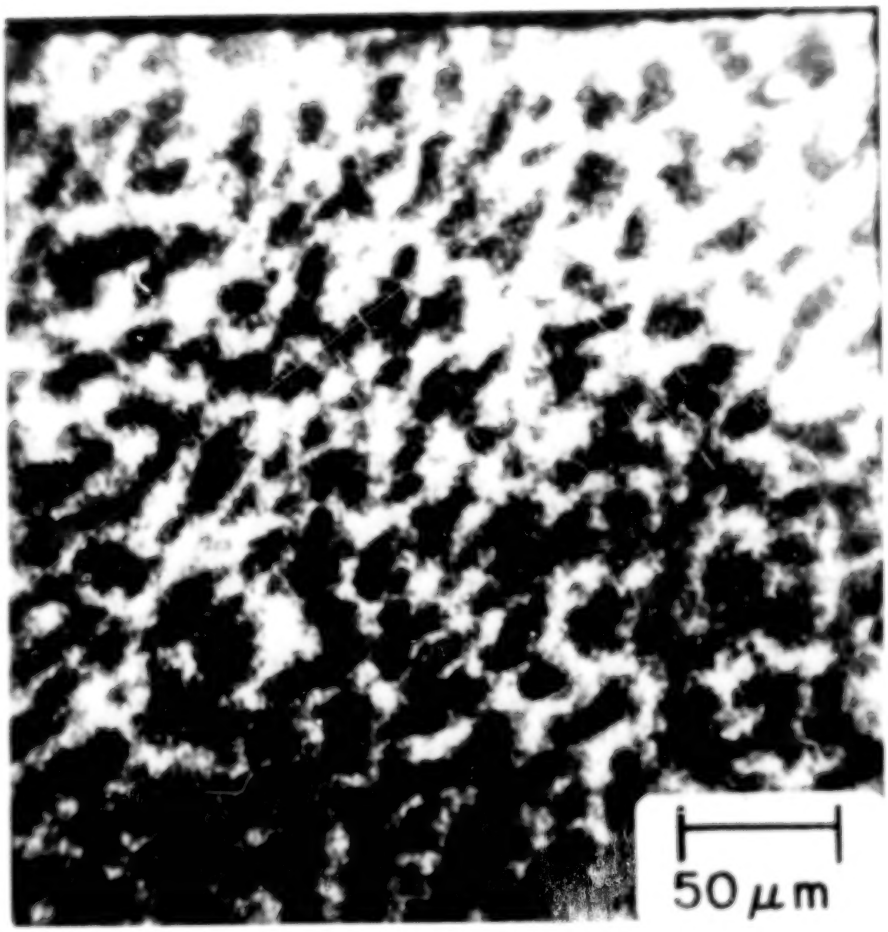

Figure 3. CL distribution in Zn-doped layer.

The CL efficiency also is influenced by defects and compositional changes [2, 6, 8]. It is unlikely that the patchy contrast is induced by defects, since the patches appear over the whole specimen surface, whereas defects produce sharp, localized CL-images. On the other hand, a fluctuation in alloy composition appears as the only effect among those cited that could well account for the local CL intensity variations. Changes in the band structure shift both the emission spectrum [1] and the ratio of radiative to non-radiative recombination. Also, the number of electron-hole pairs generated for a fixed beam voltage and current increases as the band-gap becomes smaller. The relationship between CL-intensity and alloy composition is deduced experimentally in the next section.

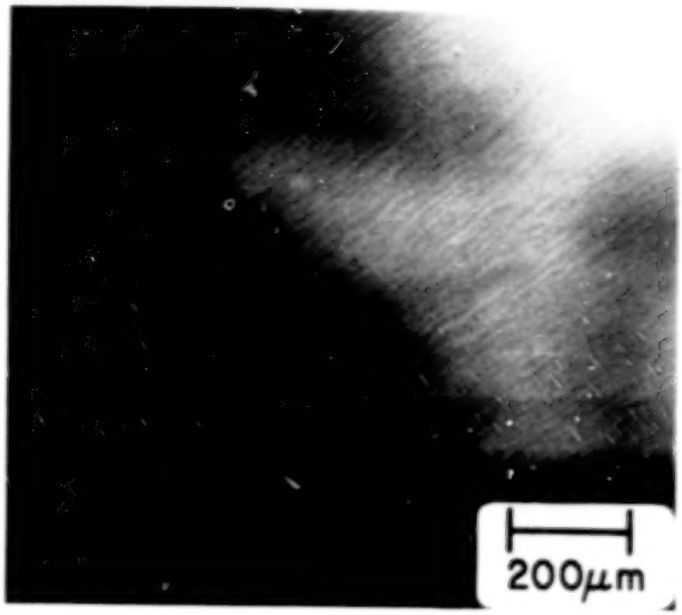

(a)

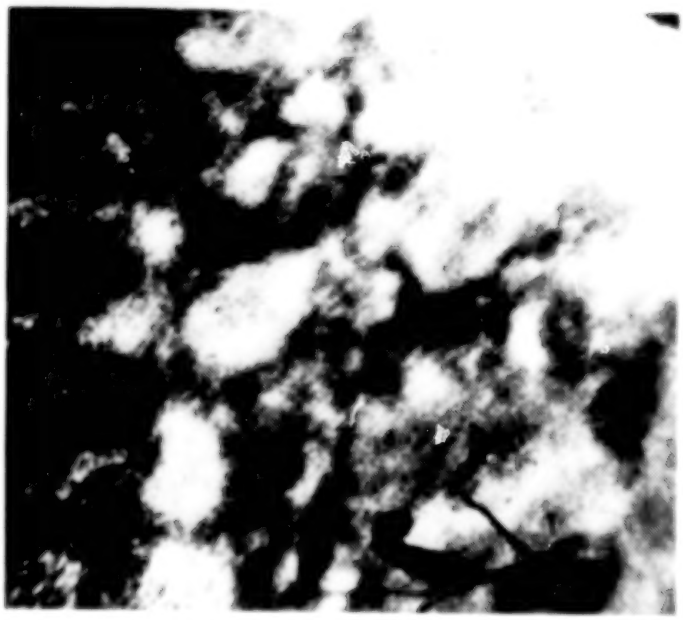

(b)

Figure 4. (a) SE- and (b) CL-images of Te-doped layer.

Figure 5 shows (a) SE- and (b) CL-mode images of a specimen containing four graded (AlGa)As layers grown on a Si-doped substrate. The surface shown is a cleaved edge. Marked variations in CL efficiency are evident across the graded layers and at the epitaxial layer-substrate interface. The CL-intensity distribution is not greatly affected by the surface topography, which contains many cleavage striations. The four graded layers and a cap layer (not of interest in the present work) also can be seen in SE contrast. A Y-modulation CL line scan across the center of this region is shown in Fig. 5 (c). The CL-efficiency varies considerably across each of the graded layers, with the overall CL-intensity decreasing with layers farther from the substrate. The efficiency everywhere in the graded layers is higher than in the substrate and in the cap layer.

Compositions of the alloys within the graded layers were obtained by electron probe microanalysis (EPMA) of a shallow (11°) angle-lapped portion of the specimen. The upper part of Fig. 6 reproduces a chart recording of the Al Kα x-ray signal (counts/sec) as a function of position across the graded layers. In addition to such line scans, careful point-to-point determinations of Al concentration were made by EPMA, with references to known materials and ZAF (atomic number, absorption and fluorescence by x-ray spectral lines of matrix elements) corrections. The variations in Al Kα intensity in the figure correspond to Al content in the range $0.22 < x < 0.30$. The lower curve of Fig. 6 is a smoothed-out Y-modulation CL line scan displayed on the same horizontal scale, which here refers to actual specimen dimension parallel to the direction of layer growth (perpendicular to surface). The scale for CL-efficiency is normalized, in this case to the intensity in the cap layer.

The close correlation exhibited in Fig. 6 between Al concentration and CL efficiency suggests that a definite relationship can be established between these quantities. Figure 7 shows such a relationship, derived from CL-intensity measurements and the EPMA determinations of Al concentration. While there is some scatter in the plotted points, the CL intensity appears to vary linearly with Al content in this range of compositions. The solid portion of the line comprises the region over which direct correlations are made.

The rapid change of CL efficiency with composition supports the idea that the patchy CL contrast in the thin LPE layers may be attributed to

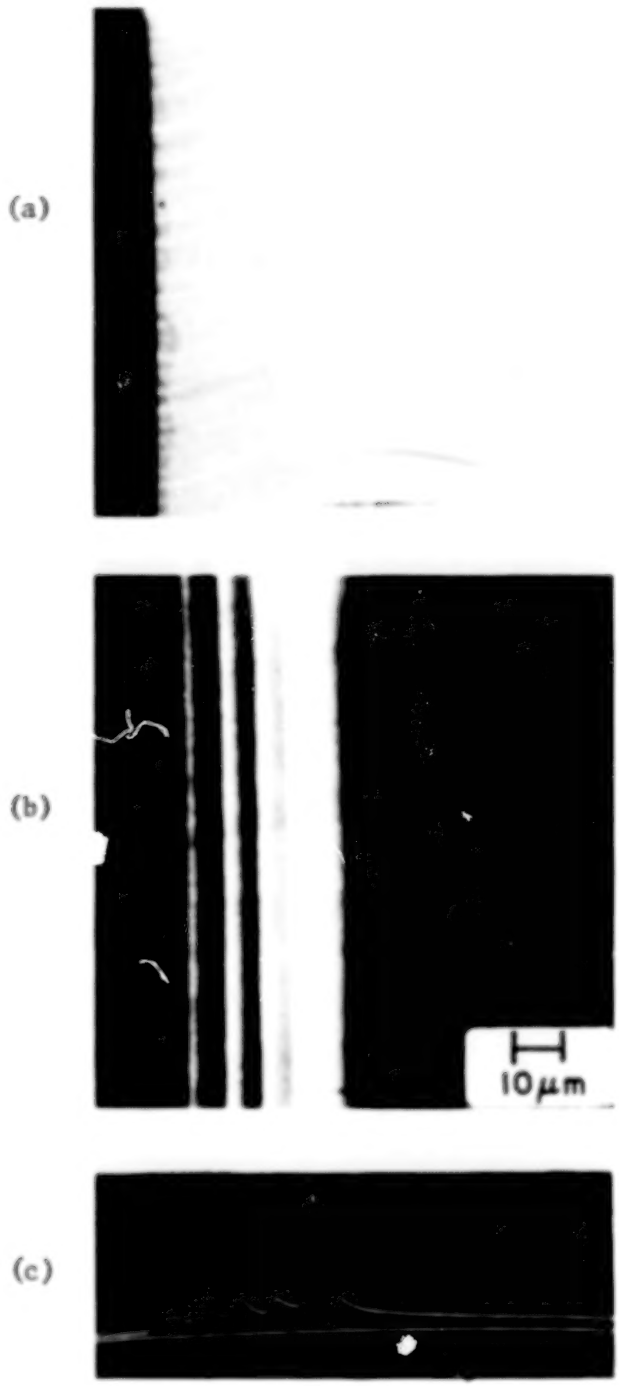

Figure 5. (a) SE- and (b) CL-images of cleaved edge of specimen containing 4 thick, graded (AlGa)As layers, (c) Y-modulation CL-line scan in same region.

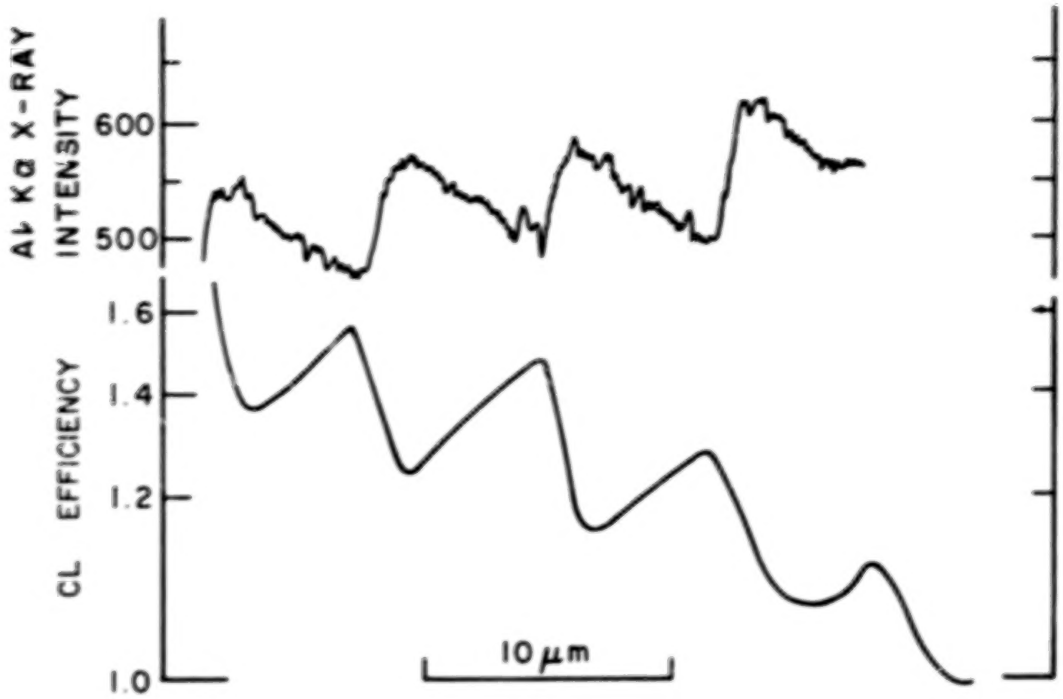

Figure 6. Comparison of electron probe data and SEM CL-efficiency for sample containing 4 graded (AlGa)As layers.

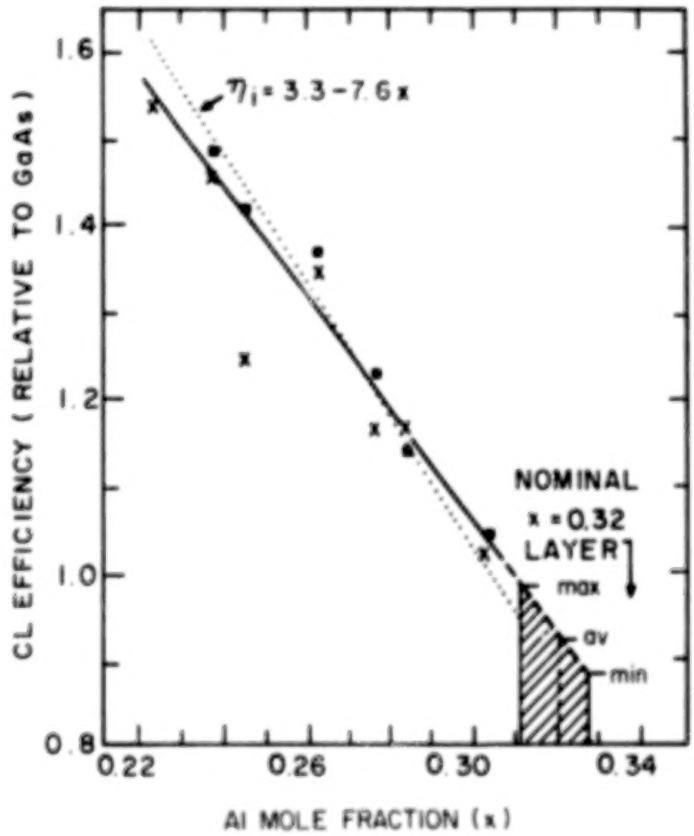

Figure 7. Variation of CL-efficiency of $Al_xGa_{1-x}As$ with mole fraction of Al(x).

local variations in the Al distribution. A quantitative estimate of the Al nonuniformity can be obtained by extrapolation of the relation in Fig. 7. Taking the nominal composition of the layer in Fig. 1 (x = 0.32 as determined by EPMA) as the average point about which the Al concentration varies, and indicating the range of CL intensities represented, it is seen that the shaded region of Fig. 7 characterizes the extent of variations within the layer. According to this interpretation, the Al content varies between $x \sim 0.311$ and $x \sim 0.327$, a range $\Delta x \sim 0.016$ or nearly one atomic percent.

The resolution of CL observations is determined principally by the size of the region of interaction between the incident electrons and the specimen, and the range of diffusion of the beam-excited carriers. A simplified picture is that the beam-specimen interaction takes place in a sphere with a diameter equal to the primary electron range. For GaAs, the range of 17 keV electrons is about 1.3 μm. Thus, the initial CL excitation is contained within the LPE layer (~ 1 μm thick) of the single-layer specimens. However, some CL signal also arises from radiative recombination of beam-excited carriers diffusing out of this region. Since the substrate is heavily-absorbing GaAs:Cr, most carriers diffusing to the epilayer-substrate interface recombine nonradiatively. The effective diffusion length of the single-layer specimens is much reduced, approaching $t/\sqrt{3}$ in the limit of small layer thickness (t) and large surface recombination velocity [9]. Thus, the CL signal arises from a region not much larger than the primary interaction diameter. In fact, the resolution evident at feature AB in Fig. 1 is $\leq$ 2 μm.

Several additional factors must be examined in connection with the assumption, tacitly contained in the foregoing discussion, that the composition fluctuations in the single-layer specimens can be determined by use of a relation based on multilayer specimens. First, during the growth of the multilayer sample, the impurity segregation coefficient may change. This could occur both because the temperature change is greater than for the single layers, and because Al is gradually depleted from the melt. However, as the photoluminescence (and presumably CL) vary relatively slowly with doping near

9. A. Many, Y. Goldstein and N. B. Grover, *Semiconducting Surfaces* (North Holland Publ. Co., Amsterdam, 1965).

the levels (10^{18} cm^{-3}) of our specimens, this effect appears not to be important. A second factor is that the CL fluctuations observed in the (thin) single-layer samples may be smaller than they would be in the absence of substrate losses. This effect is related to the reduction of overall CL intensity level by nonradiative recombination in the substrate, as discussed previously. Finally, the CL efficiency may be a nonlinear function of the excitation level [3]. However, the CL-intensity measurements of both the single- and multi-layer specimens were made with beam currents of the same magnitude. Further, the qualitative features of the CL contrast do not change with differing conditions of beam voltage and current.

The conclusion that the CL intensity variations are related to composition changes in the LPE layers is strongly supported by data from a previous investigation. In the range of alloy composition studied, the proximity of the indirect bandgap begins to affect the proportion of carriers that recombine radiatively. Estimates [10] of this effect show that the internal efficiency η_i may be reasonably represented by a linear function of the Al fraction x (for $x \gtrsim 0.2$), as shown in Fig. 8; this relationship can be expressed in the form

$$\eta_i = c - 7.6x$$

where c is a normalization constant. A plot of this relation, with c chosen to place η_i equal to the CL efficiency at $x = 0.27$, is given by the dotted line in Fig. 7. The close correspondence between the slopes of η_i and the CL data suggest that these two quantities are controlled by the same mechanism.

We note that a typical composition step at the laser heterojunction, $\Delta x \gtrsim 0.2$, is more than an order of magnitude larger than the fluctuations found in this work. Similar fluctuations, if they occur in laser diodes, are therefore only small perturbations on that step. However, fluctuations in the junction plane within the recombination region can be important in affecting local gain and loss values, and thus, can produce nonuniformities that impact modal purity.

---

10. I. Ladany, H. Kressel and C. J. Nuese, NASA Contractor Report CR-2823, April 1977, (The National Technical Information Service, Springfield, VA. 22161) (See, also, Ref. 16, Chapter 12.)

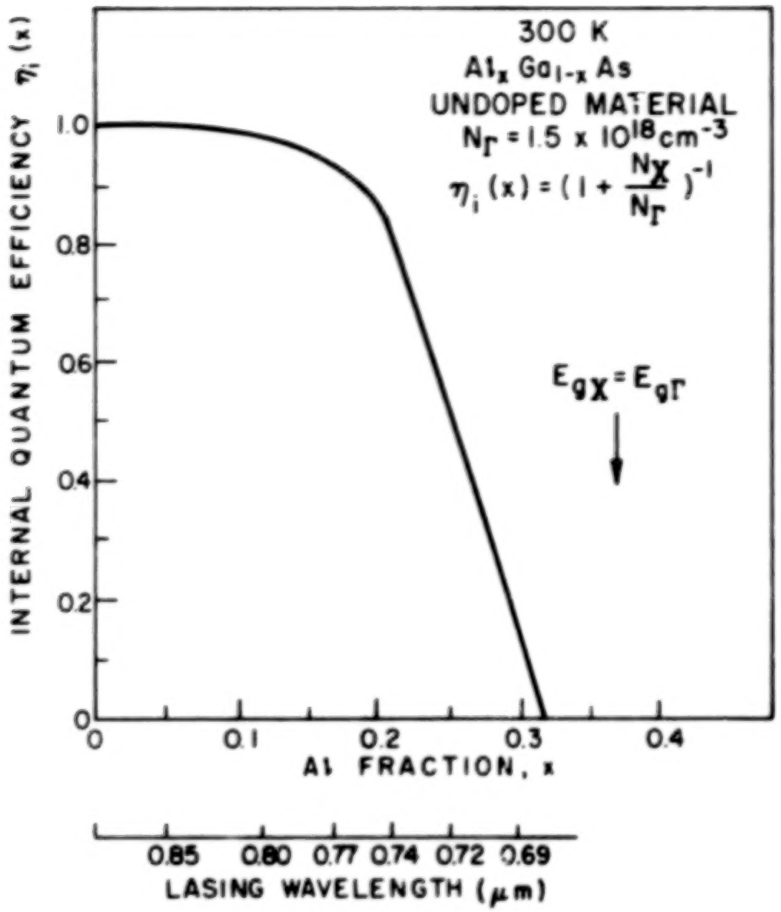

Figure 8. Calculated internal quantum efficiency as a function of x, the mole fraction of Al in (AlGa)As. (The L minima are neglected in this calculation).

C. ANALYSIS OF STRIPE CONFIGURATION

Because of its established long operating life and convenience in fabrication, the oxide-stripe configuration was used in the development of high-Al lasers. In this section we discuss work directed toward a better understanding of this important structure.

It is generally accepted that three factors determine the effect of current-confining stripes on the threshold current: (1) mode loss, (i.e., optical absorption), (2) carrier-out-diffusion within the recombination region, and (3) current leakage.

The solution of the general problem is complex, and it is difficult to obtain closed-form solutions that include optical absorption, which depends

on the specific lateral modes excited. However, if the stripe is not too narrow, (~10 μm) the principal effects include carrier-out-diffusion and current leakage and not absorption. Thus it was possible to obtain design equations including these two effects. A set of curves were constructed for the ratio of threshold current density in a stripe to that in a broad-area laser as a function of stripe width and p-layer doping. The curves of Fig. 9 provide a guide to stripe-laser design valid to stripe widths of about 10 μm. Comparing these predictions with experimental threshold measurements one can estimate the effect of other factors, including the neglected optical absorption. It was concluded that, at stripe widths approaching 4-5 μm, other effects come into play which drive up the threshold current. These are larger than could be expected from standard calculations of mode loss, and may very well be connected with the inhomogeneities discussed in the previous section. A full report of this work is given in Appendix B. For the material properties used in our devices, it appears that the optimum stripe width should be about 8 μm. Below that, an increasing penalty is exacted in terms of threshold current, although certain advantages may arise due to suppression of higher-order lateral modes.

D. LASER DIODE PROPERTIES

As discussed in previous reports, Zn and Te are preferred dopants for shorter-wavelength lasers. A difficulty caused by the use of Ge is illustrated in Fig. 10, which shows the mobility in Ge-doped $Al_xGa_{1-x}As$ as a function of x for a constant free-carrier concentration in the layer. Clearly, high-doping levels cannot be achieved using Ge in Al-rich layers. The effect of substituting Zn for Ge on device properties will be discussed in later sections of this report.

A diagram of a typical laser structure used in this work is shown in Fig. 11. The p-type GaAs "cap" layer is doped with either zinc or germanium. From a consideration of the required refractive index change, and from data accumulated in a number of trials, the required Al concentration in both regions can be determined as a function of the emission wavelength, as shown in Fig. 12. These curves only deal with the index change and bandgaps required for radiation and carrier confinement.

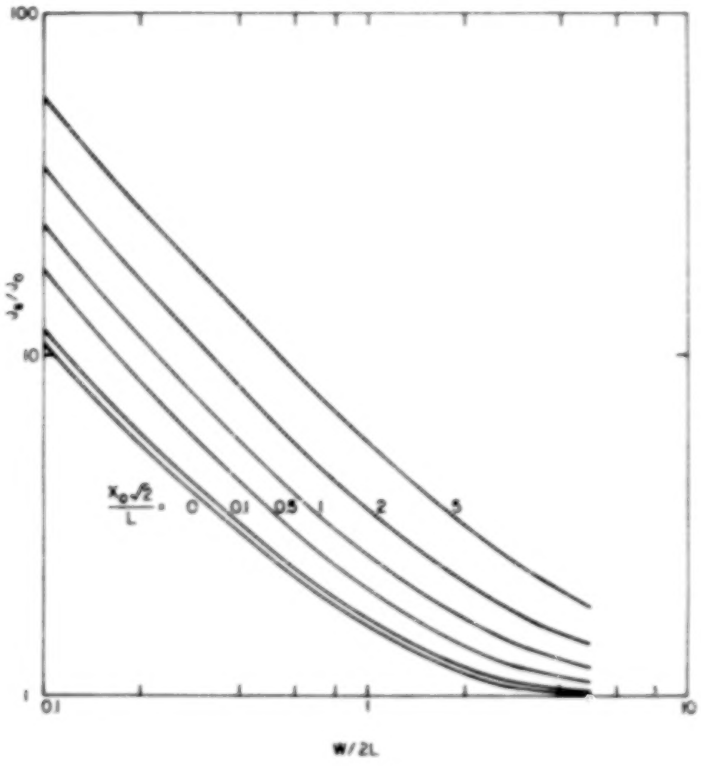

Figure 9. Ratio of stripe laser threshold current to broad-area laser threshold current for oxide-isolated stripe lasers. These curves are obtained from calculations that take account of carrier-out diffusion and current leakage, but neglect optical absorption. x_o is defined by $\frac{mkT}{R_s J_o q}$ where m ~ 2, R_s is the p-layer sheet resistivity, and J_o is the broad-area threshold current density.

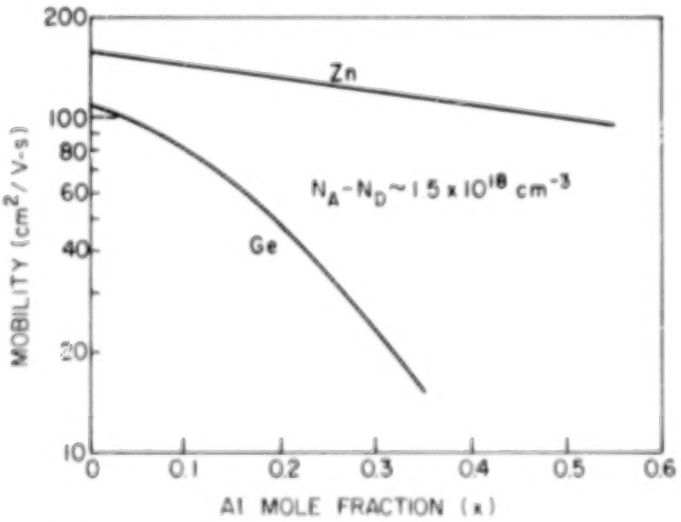

Figure 10. Mobility in (AlGa) As as a function of x, the mole fraction of Al for a fixed acceptor concentration.

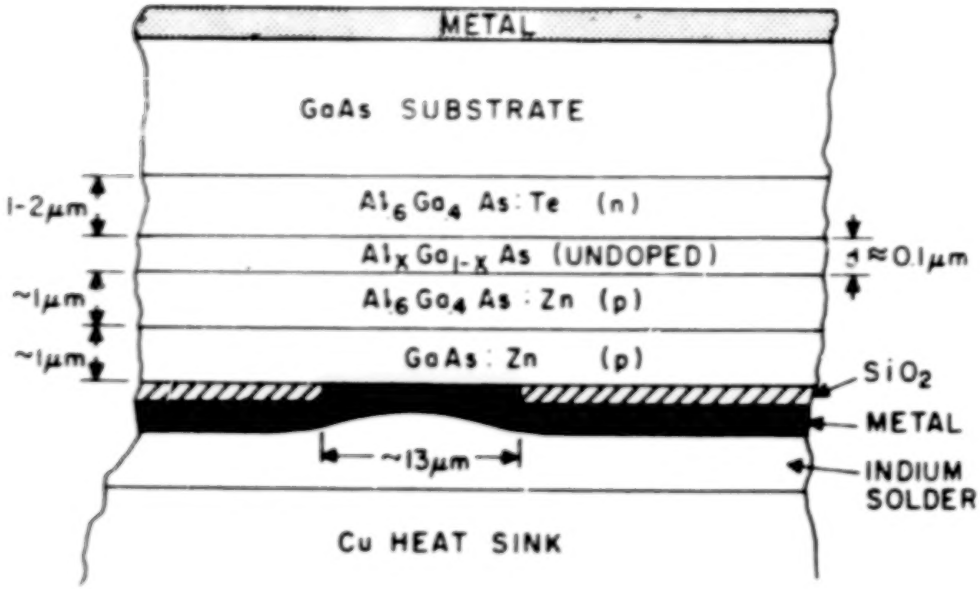

Figure 11. Typical stripe laser configuration.

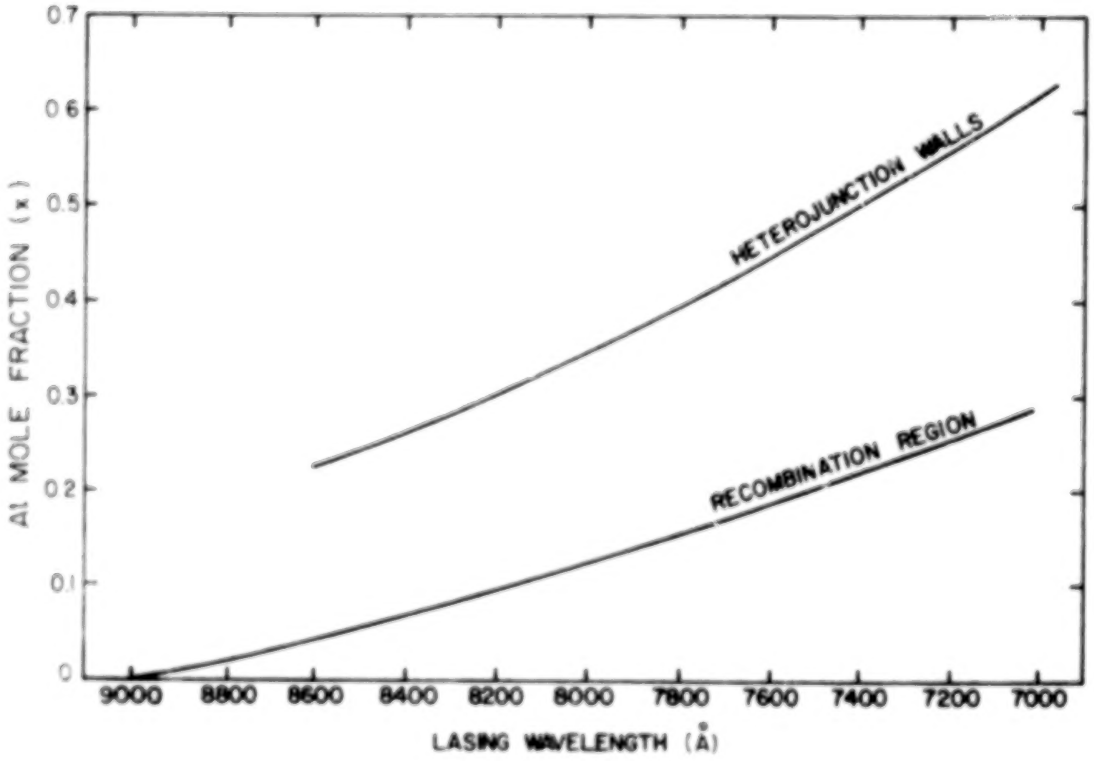

Figure 12. The required Al fraction, x, in the confining (heterojunction) regions, and in the recombination region in order to provide low threshold lasing at the indicated wavelength.

The performance of our best short-wavelength lasers is described using Figs. 13 through 16. The emission spectrum of the shortest cw room-temperature laser yet reported is shown in Fig. 13. It is a conventional pattern showing several longitudinal modes clustered around 7260 Å. The power output as a function of current of such a laser is shown in Fig. 14. The cw differential quantum efficiency is only about 2.5%, whereas for longer-wavelength devices, the value is at least 6%. The far-field beam width (full width to 1/2 power) of 50° shown in Fig. 15 is indicative of strong radiation confinement. Strong carrier confinement is also shown by the curve in Fig. 16, which shows a threshold increase by a factor of about 2 for a temperature change from 20°C to 75°C. Thus, the only significant difference between the initial performance of the short-wavelength laser and long-wavelength lasers is the lower power efficiency, which is not unreasonable considering the reduced internal efficiency in alloys with x = 0.265 (see Fig. 8). The operating life of these lasers, however, is still relatively short, a subject that is discussed in the following section.

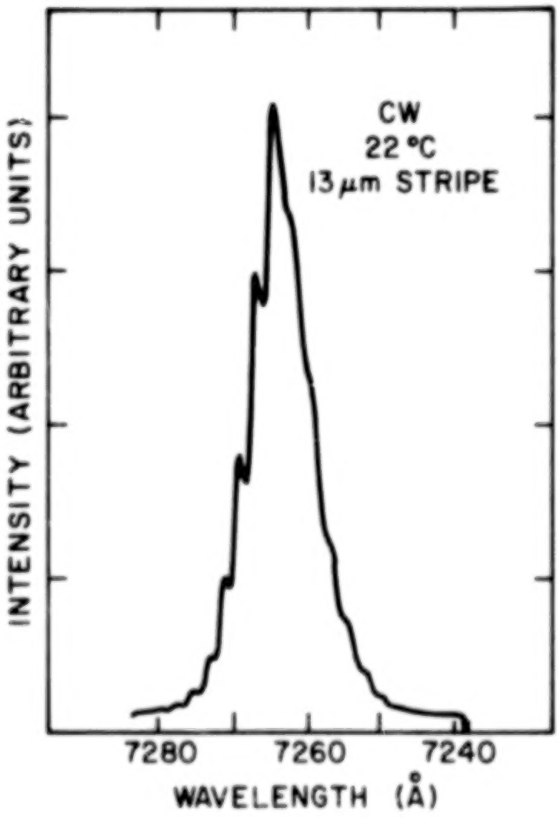

Figure 13. Emission spectrum of a short-wavelength cw laser.

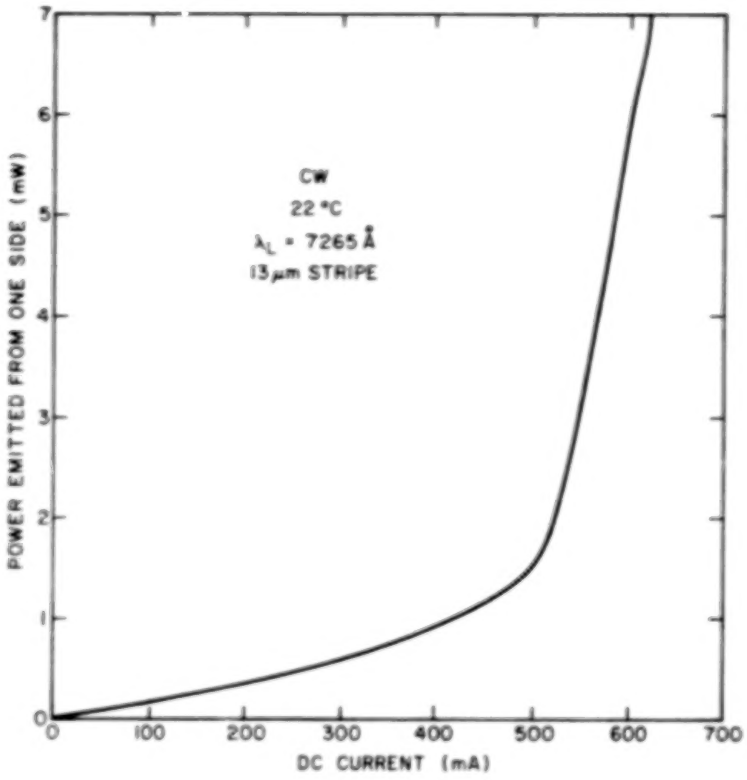

Figure 14. Power vs current characteristic of a short wavelength laser.

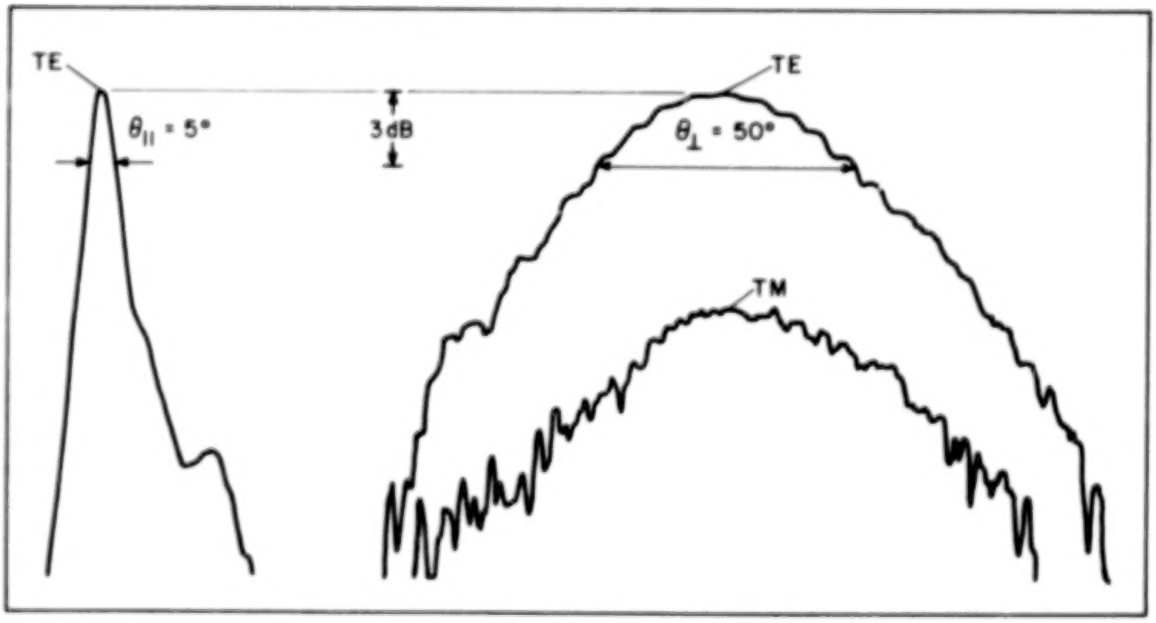

Figure 15. Far-field pattern of some laser as that used in Figs. 5, 13 and 14.

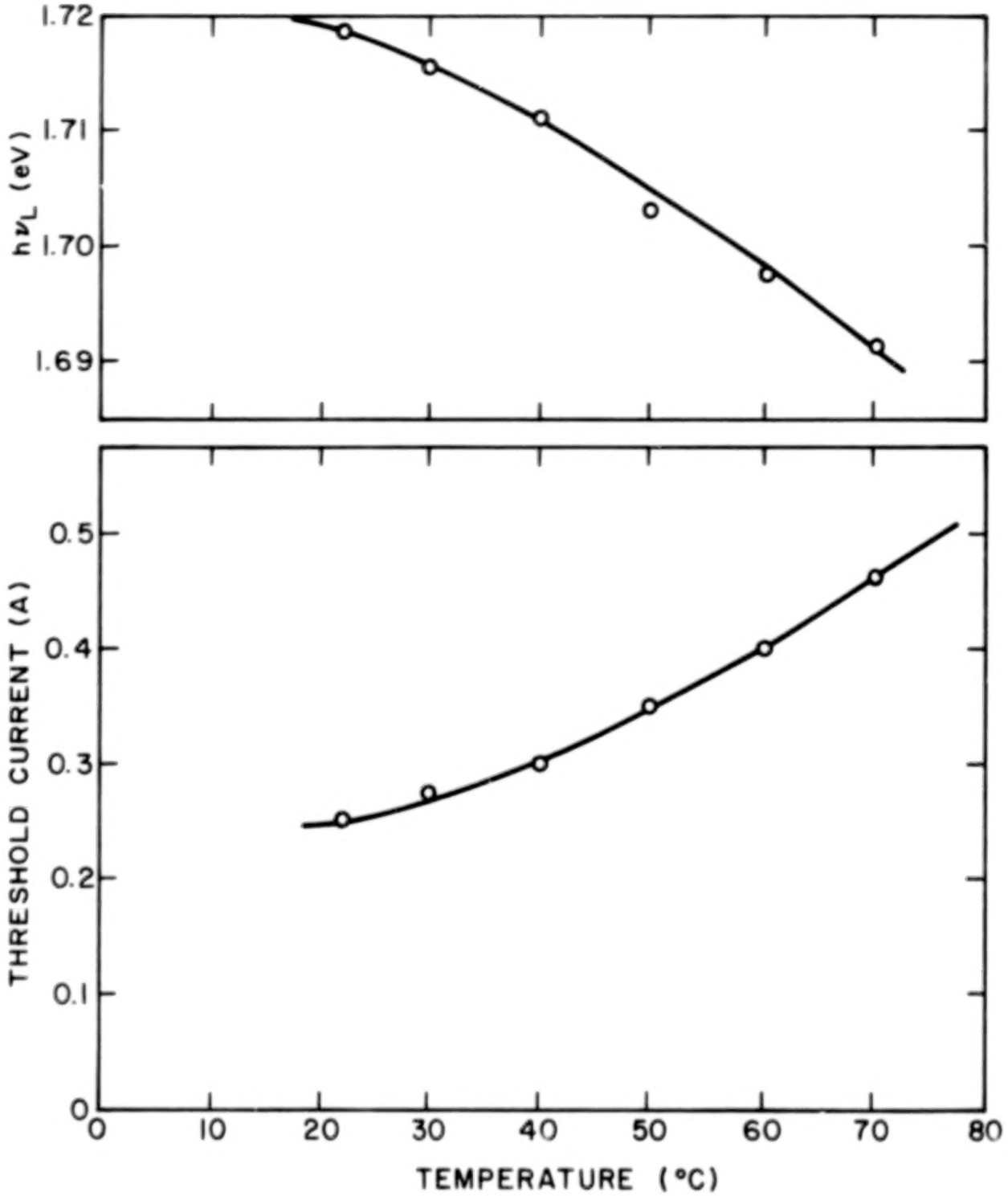

Figure 16. Temperature dependence of emission energy and threshold current for the laser described in Figs. 13, 14 and 15.

E. RELIABILITY

Work in this area is conveniently presented by dividing the discussion into two subsections: one dealing with longer-wavelength material ($\lambda \gtrsim 8000$ Å), and the other with lasers emitting in the 7000-8000 Å range.

1. Longer-Wavelength Lasers

The general use of Al_2O_3 coatings for preventing facet damage (or "erosion") was discussed in previous reports. It is particularly advantageous to make the thickness of these coatings equal to one half of the wavelength in the material because the facet reflectivity is unchanged. An effective way of determining the required thickness for a given reflectivity is to measure the outputs from the two facets of a laser, one of which is coated with the particular film being investigated. For the power ratio from the two sides of the laser one can derive the following equation [11]:

$$\frac{P_1}{P_2} = \left(\frac{R_2}{R_1}\right)^{1/2} \left(\frac{1 - R_1}{1 - R_2}\right) .$$

Here P_1 refers to the power emitted from facet 1 with reflectivity R_1, and P_2 is the power from facet 2 with reflectivity R_2. This equation assumes that for $R_1 = R_2$, the power ratio will be unity, which is usually the case. Owing to various factors, the power from the two facets when $R_1 = R_2$ may be unequal, but these perturbations can be avoided by accepting data only from units with equal (uncoated) power outputs.

Another difficulty arises for very low reflectivities, when the laser may switch to a different mode distribution. Nevertheless, if carefully used, the method is effective in evaluating coatings. Figure 17 gives a plot of reflectivity of Al_2O_3 films vs t/λ_o, the ratio of the film thickness to the wavelength in air. From such a plot one obtains the index, $n_{Al_2O_3} = 1.72$.

---

11. M. Ettenberg, H. S. Sommers, Jr., H. Kressel, and H. F. Lockwood, Appl. Phys. Lett. 18, 571 (1971).

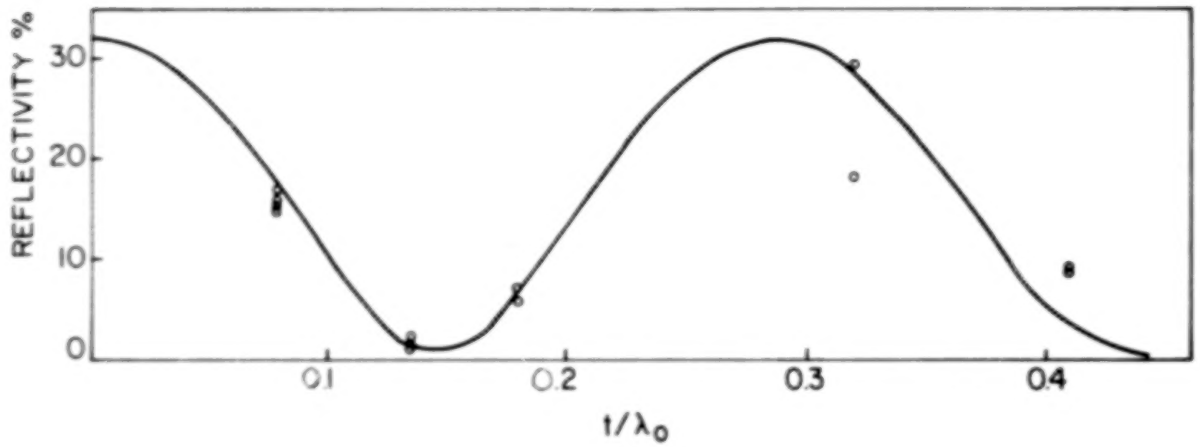

Figure 17. Reflectivity as a function of t/λ_o where t is the film thickness and λ_o is the wavelength in air. The solid curve shows the calculated reflectivity, assuming n = 1.72 for Al_2O_3 and n = 3.6 for GaAs.

Life tests of representative coated units are shown in Fig. 18. Also shown are similar data for an uncoated unit operating in a protected dry ambient. While the output of this diode decreased in an irregular manner, it nevertheless continues to lase (actually having accumulated over 28,000 hours so far). The coated units show only a slight decrease in output for operating times in excess of 22,000 hours, a result which is consistent with many other life tests currently in progress. One diode in this series failed abruptly at 7000 hours, with no evidence of facet damage. We have not observed this behavior in any previous studies; it may be due to an internal degradation process or to a current "spike" which entered our life-test rack.

The mechanism responsible for the improvement in coated cw laser life reported here is believed to be different from that operating in high-power pulsed lasers, where it was established [11] that catastrophic facet damage can be reduced by means of facet coatings of such thickness that the reflectivity is less than that of the uncoated facet. In the case of facet "erosion", the damage is eliminated by protecting the crystal surface with films that have little or no effect on the catastrophic damage threshold. Although the facet erosion mechanism is not yet well defined, it is most likely caused by high optical flux acting on a free surface, with the ambient playing an

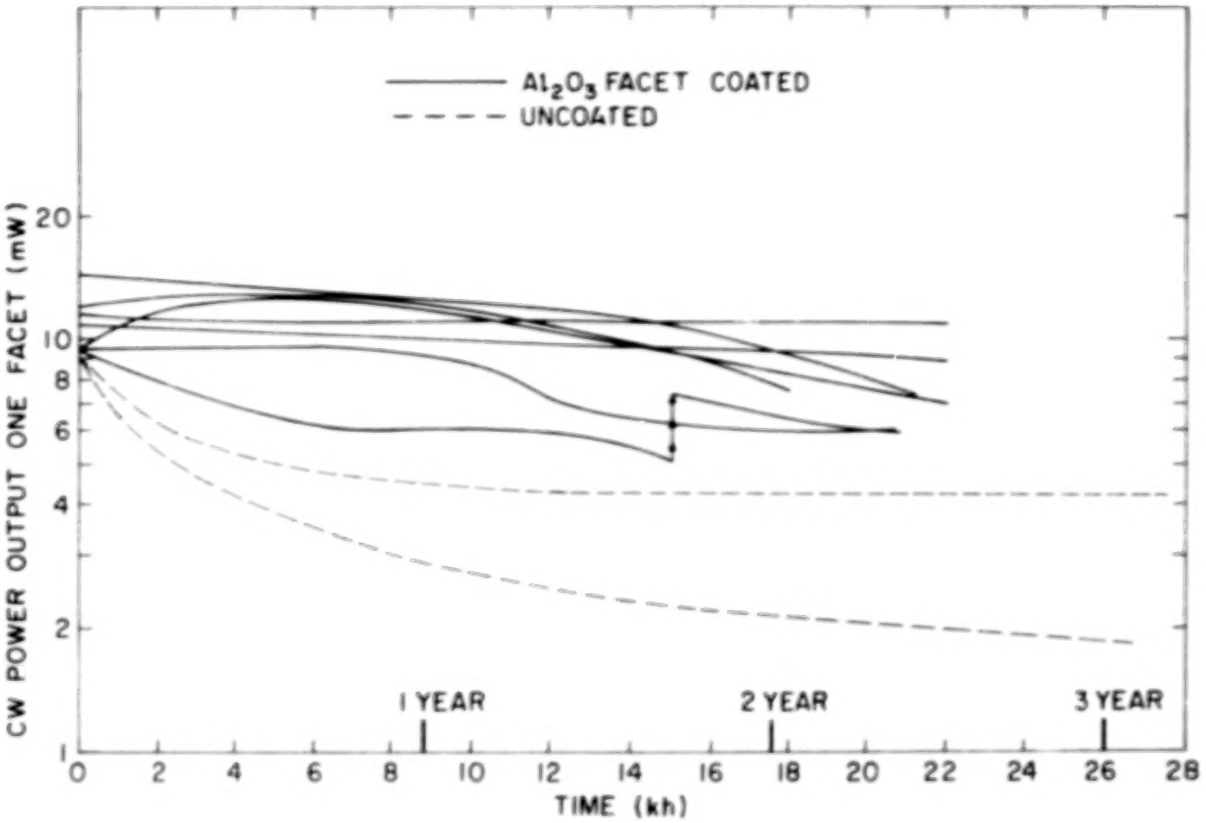

Figure 18. Lifetests of coated diodes for constant-current operation. Performance of an uncoated diode, maintained in a protected dry ambient, is also shown.

accelerating role in the process. Oxidation of the (AlGa)As is a strong possibility. A report of this work has been published, and is given as Appendix C.

In order to accelerate the evaluation of diode reliability, it is advantageous to operate lasers at elevated temperatures. This process not only accelerates temperature-activated mechanisms, but also stresses the ohmic contacts. As a result of accelerated experiments at temperatures up to 100°C (described in detail in Appendix D), we conclude that the gradual degradation process does not affect room-temperature life for periods of at least 10^6 hours.

2. Shorter-Wavelength Lasers

A study of the reliability of our short-wavelength lasers has led us to the recognition of a new degradation mechanism, and the development of an effective prevention method. We now describe this work in greater detail.

All of the lasers discussed here were formed using the oxide-isolated stripe-contact process, with a stripe width of 10-15 μm. The diodes were mounted with In solder, p-side down, on Cu heat sinks (see Fig. 11). This process of fabrication is known to generally produce very reliable devices when used for material designed to emit in the 8200-8500 Å spectral region. Therefore, any change noted in the present study is not related to either the method of junction definition or the diode assembly technique.

The Al fraction x in the recombination region determines the emission wavelength, and the Al fraction y required in the two confining layers can be read from the curve shown in Fig. 12. Material parameters used in these devices are summarized in Table 2.

TABLE 2. CHARACTERISTICS OF DIODES USED IN INCOHERENT EMISSION LIFE TESTS

Dopant in P-(AlGa)As	Mole Fraction Al* x	y	Peak Emission Energy (eV)	Threshold Current Density (K A/cm^2)
Ge	0.2	0.5	1.62	2.7
Ge	0.24	0.5	1.65	4.8
Zn	0.1	0.48	1.51	1.1
Zn	0.19	0.48	1.62	2.1
Zn	0.27	0.55	1.70	2.4
Zn + Ge	0.19	0.48	1.63	3.9
Zn + Ge	0.2	0.5	1.66	6.7

*Calculated from the melt compositions; all the structures are symmetrical, i.e., the Al concentration in both confining walls is nominally the same.

Because of the wide variation in the threshold current densities of the materials studied (which precludes convenient cw operation at room temperature in some cases), the degradation studies were conducted in the spontaneous emission mode of operation, but at a relatively high current density. Considering the contact area, the current density is calculated to be $\sim$ 4000 A/cm^2. However, some current spreading occurs below the contact, and therefore the actual current density is 1.5 to 2 times lower. For materials emitting at the

longer wavelengths, extensive degradation tests are available in the cw lasing mode, which fully confirm the similarity of the results from these two types of tests. The main difference between coherent and incoherent lifetests at longer wavelengths is probably restricted to the effect they have on the laser facet [12, 13].

In Fig. 19, we show results of incoherent lifetests on a number of diodes taken from two wafers which differ in the Al fraction in the recombination region, given by the parameter x, and the Al fraction in the confining layers adjacent to it, given by y. The dopant in the p-type (AlGa)As layer is Ge in all cases. It is to be noted that no systematic trend toward reduced output can be seen; as indicated before, lasing cw tests of diodes emitting at 1.5 eV ($\lambda \simeq 8200$ Å) show no degradation for many thousands of hours. (See Appendix C and Fig. 18.)

As pointed out earlier (see Fig. 10), it is desirable to use Zn as the dopant in p-type (AlGa)As. We have therefore tested another series of diodes in which Ge was replaced by Zn. The results of these tests are shown in Fig. 20. In these diodes, as well as in all others used in this study, there was no deliberately introduced impurity in the recombination region, although we expect some diffusion of zinc past the heterojunction. The long-wavelength data are limited in the case of zinc doping, but other test results, not included here, for zinc-type lasers emitting near 8200 Å, show cw operating lives comparable to those of Ge-type lasers.

The other two materials, designed for shorter wavelength operation show a decrease in output, the onset of this degradation occuring earlier for the shorter wavelength devices. These results are in agreement with cw lasing tests which also show a life reduction whose severity increases for the shorter wavelength emission. Since there is no observable facet damage we consider this degradation to be caused by a bulk effect (i.e., defect introduction into the recombination region).

In a third series of tests, shown in Fig. 21, similar data are given for diodes whose p-type (AlGa)As layers were double-doped with both zinc and germanium. The similarity of these results to those in Fig. 19 is striking, the

12. H. Kressel and I. Ladany, RCA Rev. 36, 230 (1975).
13. I. Ladany and H. Kressel, Appl. Phys. Lett. 25, 708 (1974).

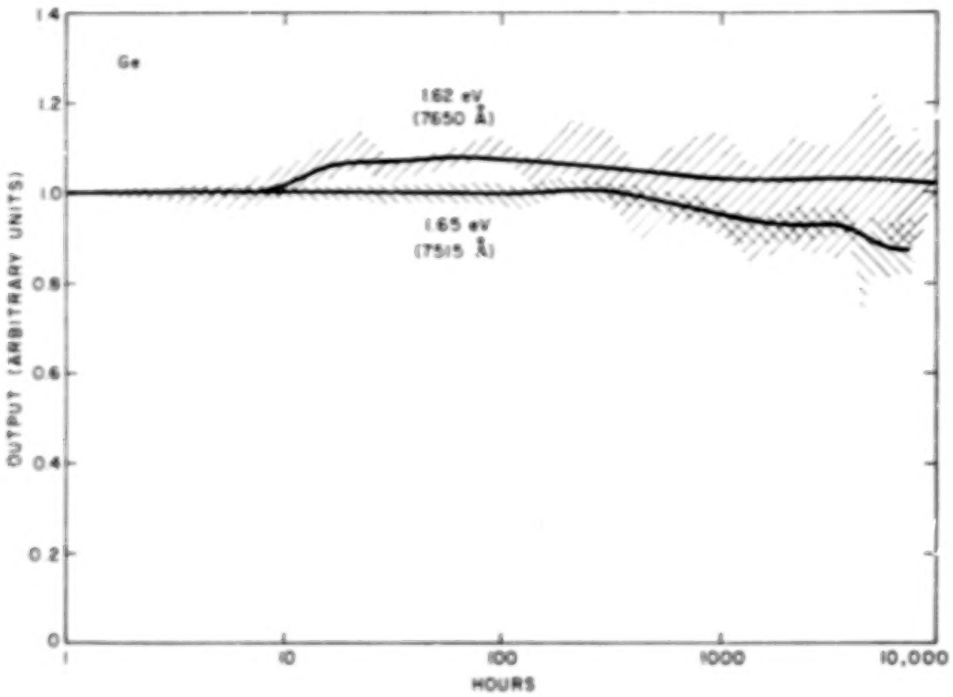

Figure 19. Incoherent normalized lifetest data of two groups of Ge-doped diodes. The solid lines show time-smoothed average values, whereas the shaded portion defines the region between the diodes with the highest and the lowest outputs. The emission energy is indicated in the figure.

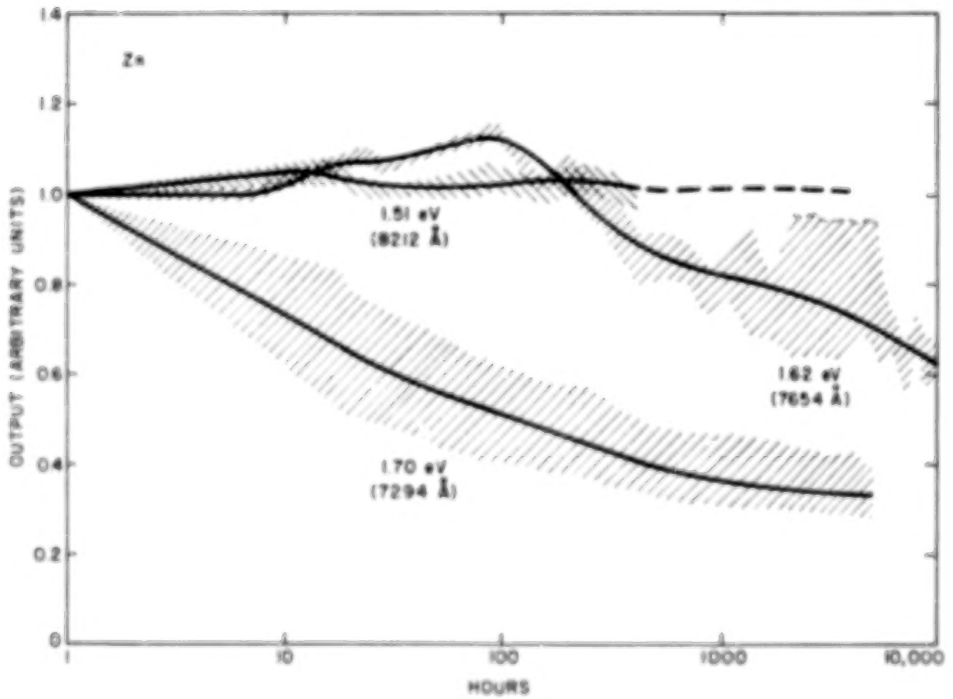

Figure 20. Same data as in Fig. 19, for three groups of zinc-doped diodes.

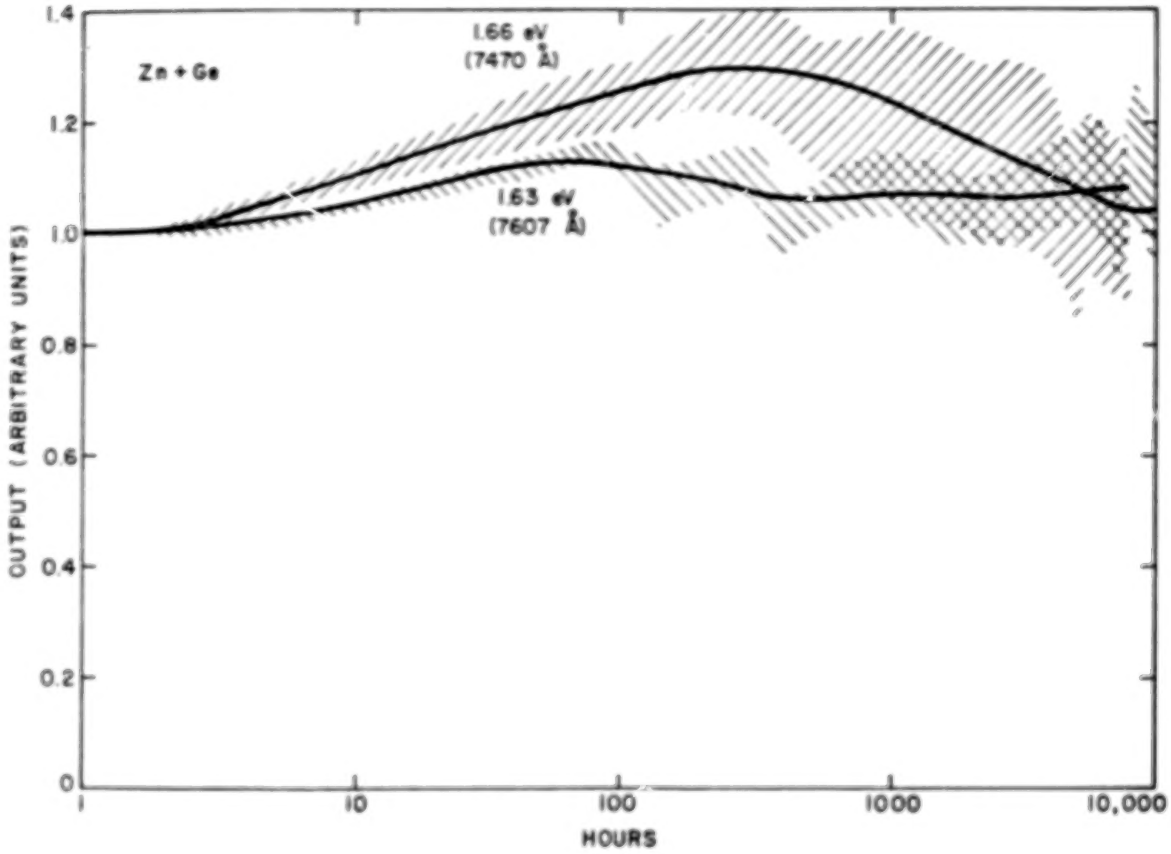

Figure 21. Same data as in Figs. 19 and 20, for two groups of diodes doped with zinc and germanium.

degradation not being evident in this case. Double-doping with these two impurities thus opens up prospects for greatly increased reliability in lasers and LED's operating at 7500 Å and below.

There are several posssible explanations for these results, and they hinge on the mechanism responsible for the start of the degradation process. It is well established that bulk degradation can occur if a dislocation network spreads from an initially present dislocation threading the active layer [14]. Although our standard growth process generally prevents the generation of these threading dislocations, this may no longer be true for the high Al concentrations used here. We have therefore examined a high Al structure ($x \simeq 0.25$ and $y \simeq 0.55$) doped with zinc in the p-type (AlGa)As layer.

14. P. Petroff and R. L. Hartman, J. Appl. Phys. 45, 3899 (1974).

The TEM, shown in Fig. 22 and provided by J. T. McGinn, is entirely free of defects at all interfaces, both at the orientation shown and when examined at other orientations.

We therefore must consider a degradation process that accounts for the generation as well as possible subsequent motion of defect-induced nonradiative centers into the active area. Since it is reasonable to suppose that zinc diffuses into the recombination region, we may imagine a process initiated by the presence of Zn in that region. However, at lower Al levels (longer wavelengths), no degradation occurs with zinc doping, nor is there any degradation in the case of double-doping, which presumably leaves the zinc diffusion unaffected.

Since changes in the p-type confining layer doping (i.e., the use of Zn vs Ge dopants) affect the degradation of our short-wavelength lasers, we may consider degradation mechanisms involving defects originating in this layer. One possibility is that point defects are generated in the layer by the energy released in nonradiative recombination [15]. For this process, a leakage current of electrons from the p-type active layer is required. Recent estimates of this electron leakage show that it can be substantial, especially for high-Al confining regions [16, 17]. Once the point defect is generated, its movement into the recombination zone and interference with radiative recombination may be accelerated by the relatively high stress occuring in this material [18].

In regard to the role of germanium additions in inhibiting the degradation process, we can make the following comments. First, Ge could be effective in preventing point-defect generation. This may be the result of a local interaction, Zn and Ge occupying different lattice sites, which reduces the probability of atomic displacement. Second, if dislocations are present, impurities can prevent their motion [19]. Although Ge was not considered especially

---

15. For a review of degradation phenomena see H. Kressel and J. K. Butler, *Semiconductor Lasers and Heterojunction LEDs* (Academic Press, 1977), chapter 16.
16. A. R. Goodwin, P. A. Kirkby, M. Pion, and R. S. Baulcomb, IEEE J. Quant Elect. QE-13, 696 (1977).
17. A. R. Goodwin, J. R. Peters, M. Pion, G. H. B. Thompson, and J. E. A. Whiteaway, J. Appl. Phys. 46, 3126 (1975).
18. Taibun Kanajima, Koichi Ishida, and Junji Matsui, Japan. J. Appl. Phys. 16, 233 (1977).
20. P. A. Kirkby, IEEE J. Quant. Elect. QE-11, 562 (1975).

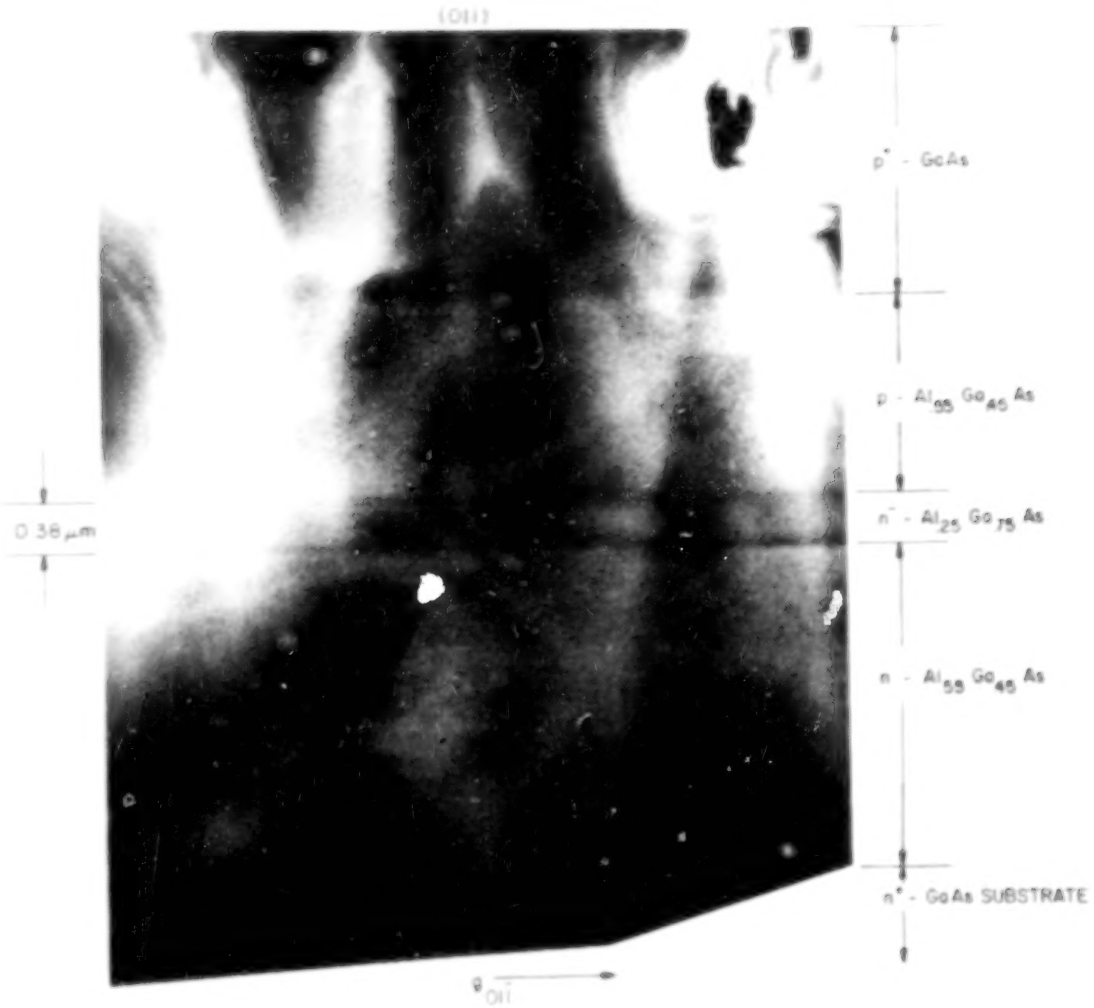

Figure 22. TEM of a high Al laser structure.

advantageous for this dislocation pinning, the complexity of the mechanism is such that this possibility cannot be excluded.

The direct application of these results to short-wavelength lasers requires caution. Thus we may not exclude the possibility that incoherent emitters and lasers degrade by different bulk processes, even though this is not the case at longer wavelengths. Until the lasing behavior of double-doped short-wavelength devices is thoroughly explored, the application of these results to cw lasing operation is only a conjecture.

SECTION III

RED-EMITTING Ga(AsP)/(InGa)P HETEROJUNCTION LASERS

A. INTRODUCTION

In the previous section, we discussed our program to develop short-wavelength lasers of (AlGa)As. This alloy system is technologically of great importance because of the ease of matching the lattice constant of adjoining epitaxial layers and because of the demonstrated performance and reliability of (AlGa)As lasers. However, the direct-indirect transition in (AlGa)As occurs at an energy of 1.92 eV, which limits practical pulsed-laser operation at room temperature to about 7000 Å, and cw operation to wavelengths still longer (probably close to the 7200-7300 Å value reported in the previous section). The Ga(AsP) alloy system has a direct-indirect transition at 1.99 eV, which should allow cw room-temperature operation with these materials to wavelengths below 7000 Å, which is well into the red portion of the spectral response of the eye. For this reason, part of our research program explored the Ga(AsP) alloy system for heterojunction lasers. The confining layers were (InGa)P, and the heteroepitaxial structures were prepared by a vapor-phase growth technology demonstrated earlier for the fabrication of GaAs/(InGa)P [20] and (InGa)As/(InGa)P [21] double-heterojunction lasers.

B. STRUCTURES

The lattice constant of $In_yGa_{1-y}P$ spans the range from 5.451 Å (for GaP) to 5.869 Å (for InP), with an energy bandgap range from 2.26 to 1.35 eV. As shown in Fig. 23 it is possible to lattice match $In_yGa_{1-y}P$ to lower-bandgap $GaAs_{1-x}P_x$ for the unique lattice-matching condition $y = 0.49(1-x)$. For the construction of heterojunction lasers, the recombination region of Ga(AsP) is in the direct-bandgap composition range, but confining layers of (InGa)P need

---

20. C. J. Nuese, M. Ettenberg, and G. H. Olsen, Appl. Phys. Lett. 25, 612 (1974).
21. C. J. Nuese, G. H. Olsen, M. Ettenberg, J. J. Gannon, and T. J. Zamerowski, Appl. Phys. Lett. 29, 807 (1976).

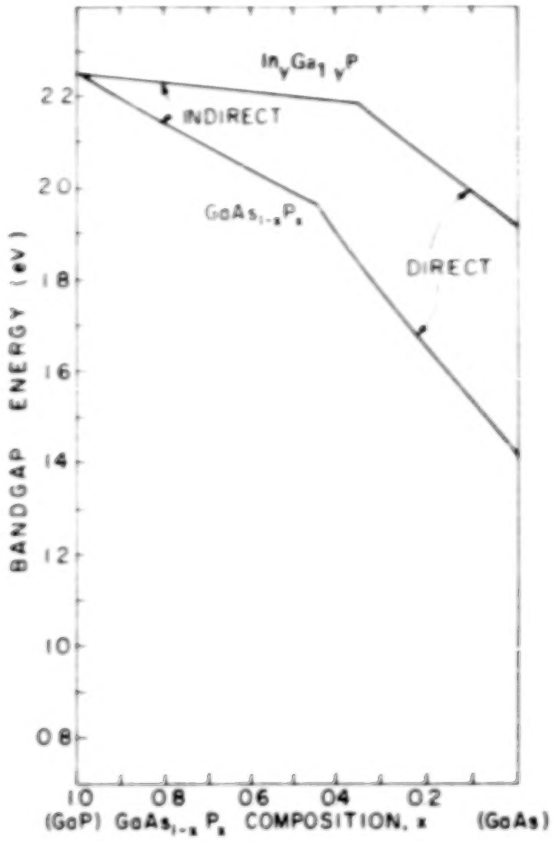

Figure 23. Room-temperature energy-bandgap values of $GaAs_{1-x}P_x$ and $In_yGa_{1-y}P$ for lattice-matched structures.

not have a direct bandgap. Figure 24(a) shows a schematic representation of a typical double-heterojunction laser cross-section. Because no lattice-matching melt-grown substrates are available for the present structure, we have used a $GaAs_{0.7}P_{0.3}$ epitaxial layer deposited on GaAs as the starting point for the fabrication process. These substrates are n-type epitaxial layers (Monsanto Co.) deposited by vapor-phase epitaxy on <100>-oriented GaAs.

The structures were grown by a vapor-phase epitaxial process described previously [20,21]. The n-type (InGa)P layer first grown over the Ga(AsP) substrate layer was sulfur doped to a level of $\sim$ 3-5 X 10^{17} cm^{-3} and provided the first of the two confining layers for the subsequently grown thin Ga(AsP) recombination region. A p-type, Zn doped (InGa)P layer ($p \sim$ 3-5 X 10^{18} cm^{-3}) constituted the second confining layer. A final surface layer of Ga(AsP):Zn was added to facilitate ohmic contact to the structure, because a reduced energy bandgap is helpful in this regard. The width of the Ga(AsP) recombination region of the best devices ranged from 0.15 to 0.22 μm. Although the

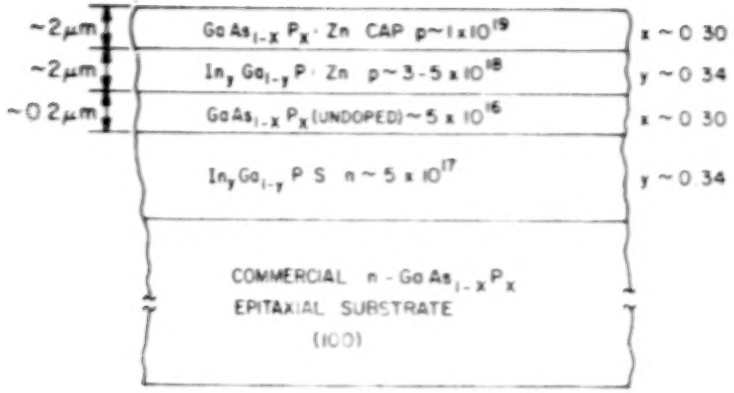

(a)

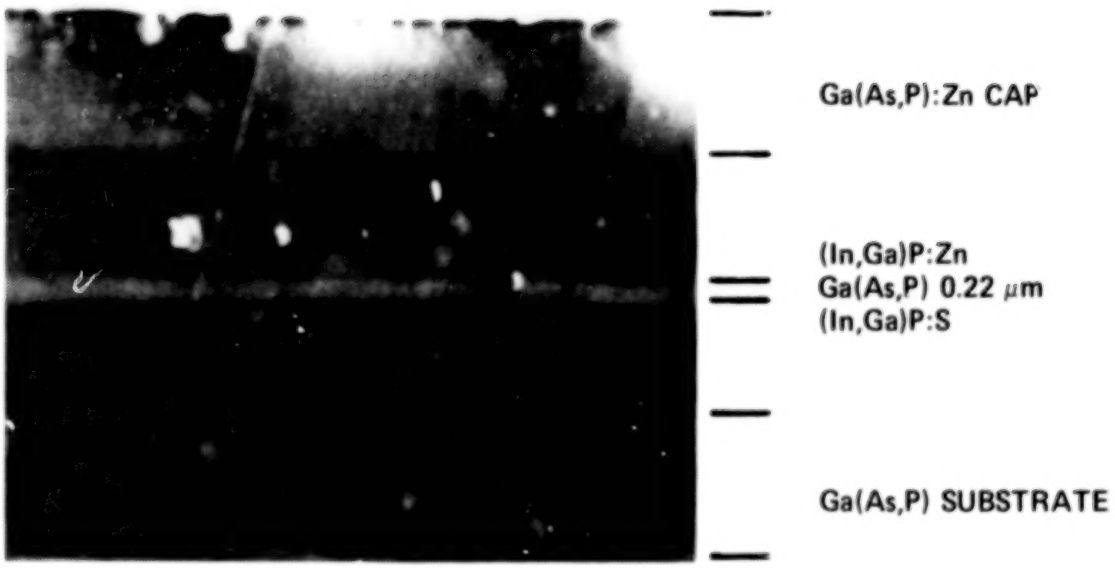

(b)

Figure 24. (a) Cross-sectional representation of structure used to prepare low-threshold Ga(AsP)/(InGa)P heterojunction lasers. (b) <100> cleavage plane cross-section of Ga(AsP)/(InGa)P vapor-grown laser structure. Thickness of Ga(AsP) recombination region is 0.22 μm, in agreement with the same value derived from capacitance-voltage measurements on this sample.

recombination region was not deliberately doped, there is evidence that Zn diffusion from the upper (InGa)P layer converted the recombination region to p-type conductivity, producing the injecting n-p heterojunction at the lower of the two Ga(AsP)/(InGa)P interfaces. This conclusion was based on scanning electron microscope observations in the EBIC (electron-beam-induced current) mode of operation, which revealed the position of the p-n interface. The junction planarity of the structures was found to be reasonable, as illustrated in Fig. 24(b).

We find no evidence of misfit dislocations introduced in the process of growing the laser structure itself because of the close lattice-parameter match maintained at the interfaces. Figure 25 shows a cross-sectional transmission electron micrograph of a laser structure, which is seen to be dislocation free. Inclined dislocations that can propagate from the Ga(AsP) substrate layer into the laser structure are not visible in this micrograph, since their density is estimated to be less than the smallest value ($\sim 10^5$ cm^{-2}) resolvable by TEM.

It is of interest to determine directly the degree of alloy uniformity achieved in the vertical (growth) direction. Figure 26 shows SIMS measurements of a device having an active region width of 0.3 μm. The interfaces are seen to be sharp within the resolution limit of the instrument.

Because of the interest in visible emission devices which press the practical limits of the Ga(AsP) system, the lasers discussed in this paper were designed for emission at about 7000 and 6800 Å at room temperature. The growth procedures for these structures were identical, except for small changes in the composition of the (InGa)P and Ga(AsP) layers to produce the desired wavelength of emission while maintaining lattice matching.

C. DEVICE EVALUATION

1. Current-Voltage Characteristics

Although not central to the issue of laser diode performance, measurements of the current-voltage characteristics provide a useful indication of heterojunction quality. Figure 27 shows the forward-bias current-voltage characteristics of a stripe-contact diode emitting at about 7000 Å. The use

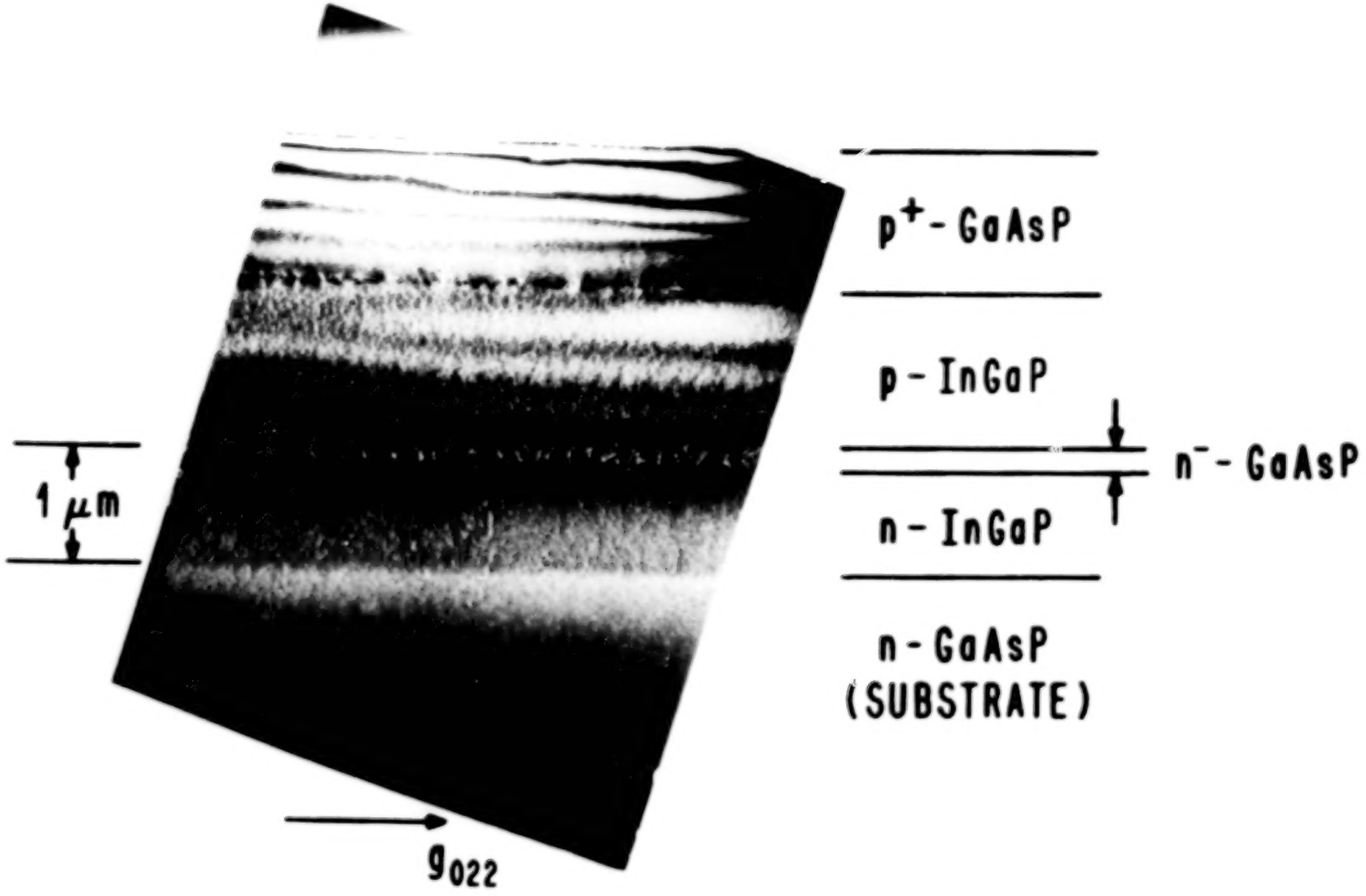

Figure 25. Cross-section transmission electron micrograph of Ga(AsP)/(InGa)P heterojunction laser. Absence of misfit dislocations is due to lattice-matching alloy compositions used here.

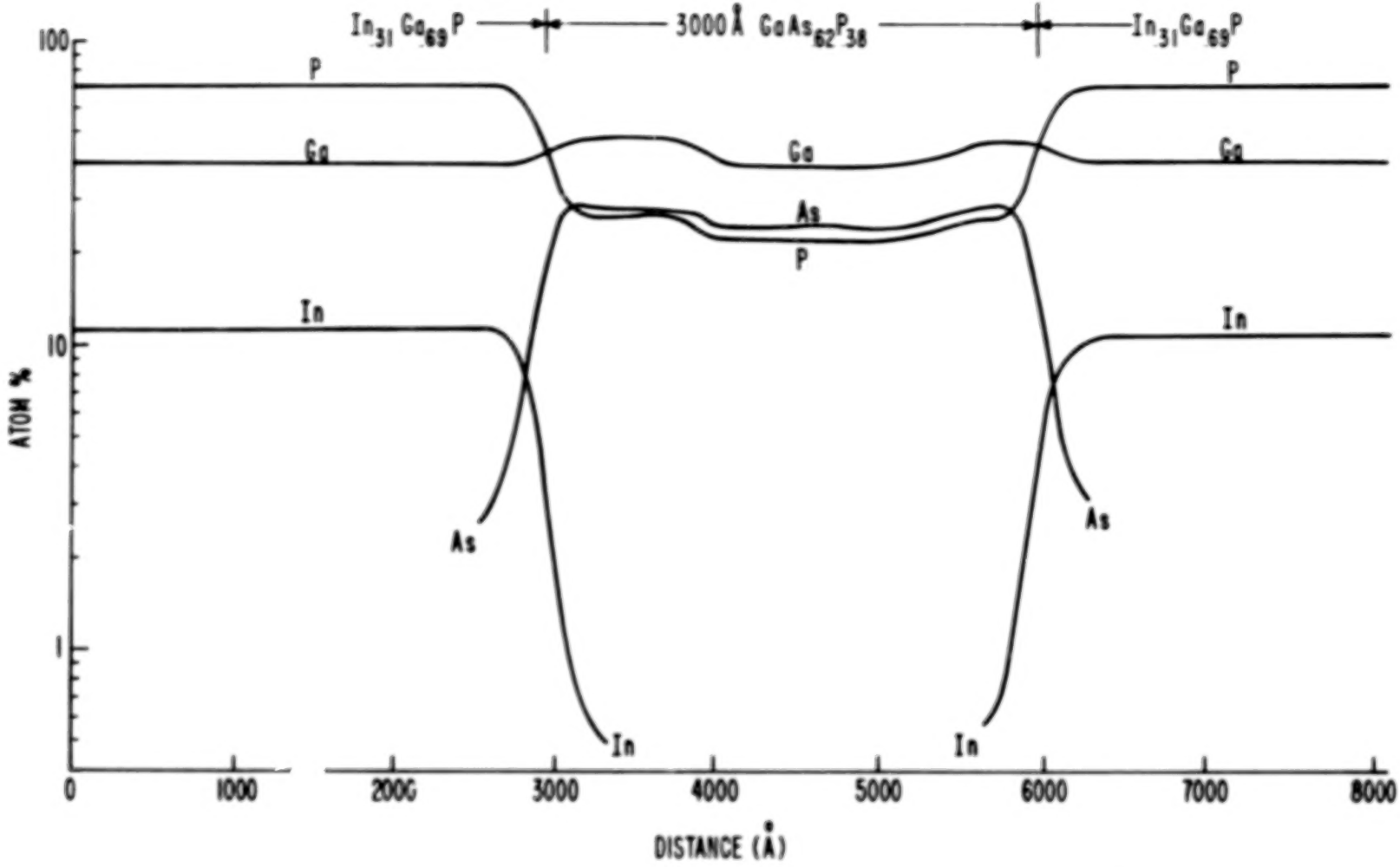

Figure 26. Auger SIMS scans of In, Ga, As, and P through the 3000 Å-thick $GaAs_{0.62}P_{0.38}$ recombination region and the $In_{0.31}Ga_{0.69}P$ confining layers of vapor-grown double-heterojunction laser structure.

37

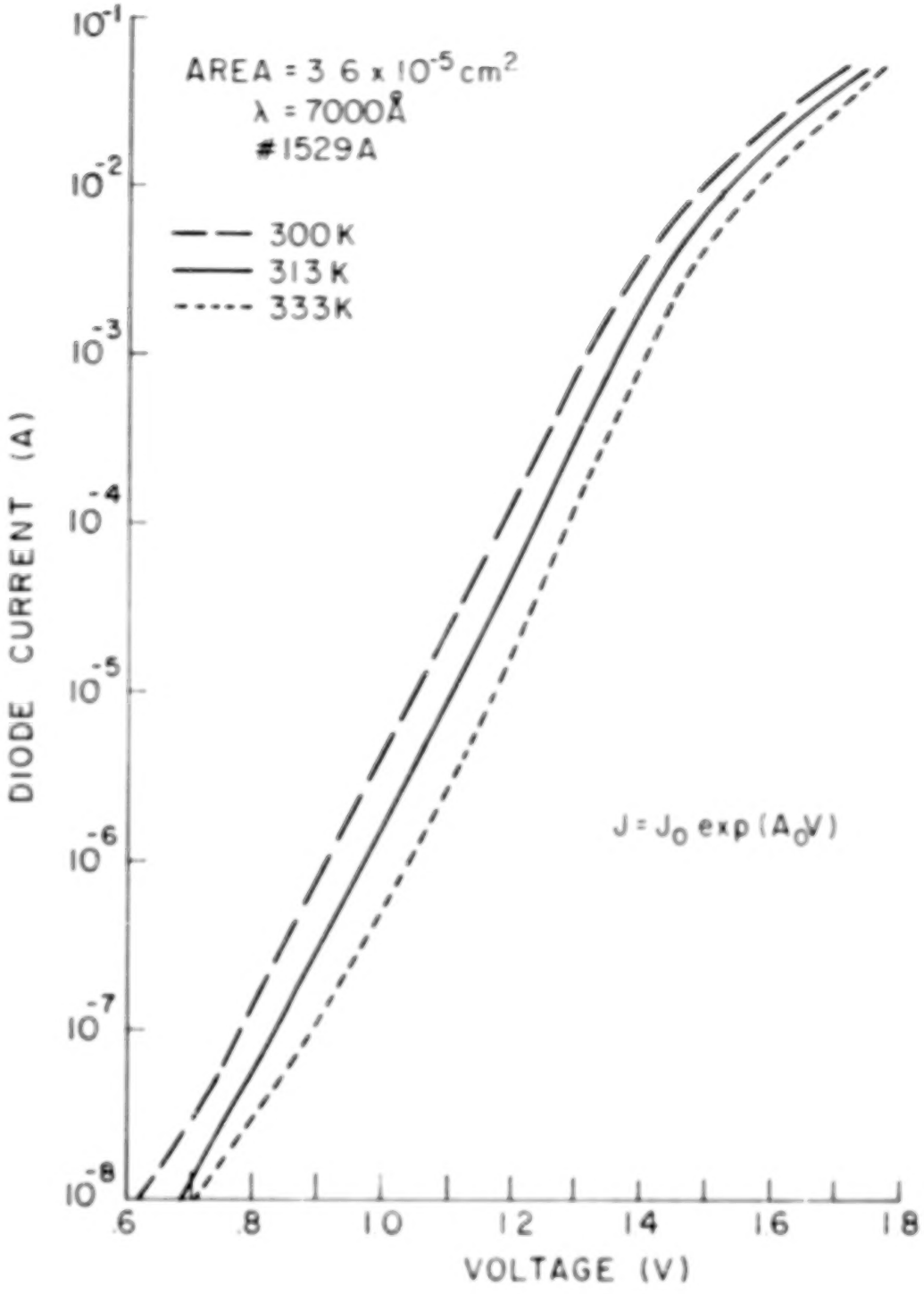

Figure 27. Current-voltage characteristic of 7000 Å Ga(AsP)/(InGa)P heterojunction laser diode at ambient temperatures of 300, 313 and 330 K. Values of A_o and J_o are given in Table 1.

of such an edge-isolated diode is desirable in studying the I-V characteristics because surface leakage is minimized. The only possible surface current source is limited to the two cleaved facets of the device. Thus, the I-V curves shown in Fig. 27 represent "bulk" properties of the diode, with possibly some very minor surface contribution at low bias levels. The current-voltage characteristics over a large range of intermediate current and voltage values follow the expression

$$J = J_o \exp(A_o V), \tag{1}$$

with the values of J_o and A_o shown in Table 3. Without carrier tunneling, A_o can generally be expressed in the form $A_o = q/\eta\, kT$, where η exceeds 2 at elevated temperatures; because the value of η is temperature dependent, the I-V curves probably include a tunneling component in addition to contributions from space-charge recombination (and possibly carrier injection). This type of I-V curve is also observed in (AlGa)As/GaAs heterojunction [22].

TABLE 3. HETEROJUNCTION CURRENT-VOLTAGE CHARACTERISTICS*

T (K)	J_o (A/cm^2)	A_o (V)	η
300	5×10^{-12}	21	1.8
313	3×10^{-10}	19	1.9
333	2×10^{-8}	16	2.2

*Edge-isolated stripe-contact diode (13 μm stripe contact).

22. J. F. Womac and R. H. Rediker, J. Appl. Phys. 43, 4129 (1972).

2. Spontaneous Carrier Lifetime

The spontaneous carrier lifetime at low injection levels is of interest as an indicator of the density of nonradiative centers in the diode recombination region and at the heterojunction boundaries. The carrier lifetime is a function of the carrier density, which eventually limits the radiative lifetime at high current densities via the process of bimolecular recombination. For the present devices, the carrier lifetime was measured as a function of current density by monitoring the change in the decay time of the light output following the end of the current pulse [23,24]. Figure 28 shows the results obtained for a 6800 and a 7000 Å device, respectively. The theoretical curves in Fig. 28 are plots of the equation for the carrier lifetime for bimolecular recombination as a function of current density,

$$\tau = \frac{qdp_o}{2J}\left[\left(1 + \frac{4J}{qB_r dp_o^2}\right)^{1/2} - 1\right] , \qquad (2)$$

where B_r is the band-to-band recombination coefficient and p_o is the hole concentration in the recombination region (taken as 8×10^{17} cm^{-3}). From the data at high current densities, we obtain an estimate for B_r from the expression,

$$B_r \cong (qd)\left[\frac{\partial\tau}{\partial(1/J)^{1/2}}\right]^{-2} . \qquad (3)$$

A reasonable fit to the data is obtained with the values $B_r \cong 0.4 \times 10^{-10}$ cm^3/s for the 6800 Å devices, and $B_r \cong 1.0 \times 10^{-10}$ cm^3/s for the 7000 Å diodes. A similar measurement in GaAs also yields $B_r \cong 10^{-10}$ cm^3/s [24,25]. The smaller value of B_r for the 6800 Å laser is consistent with a reduction in the efficiency of the radiative recombination process as the Ga(AsP) alloy composition approaches that of the direct-indirect transition.

---

23. H. Namizaki, H. Kan, M. Ishii and A. Itoh, Appl. Phys. Lett. 24, 486 (1974).
24. J. P. Wittke, N. Ettenberg and H. Kressel, RCA Rev. 37, 159 (1976).

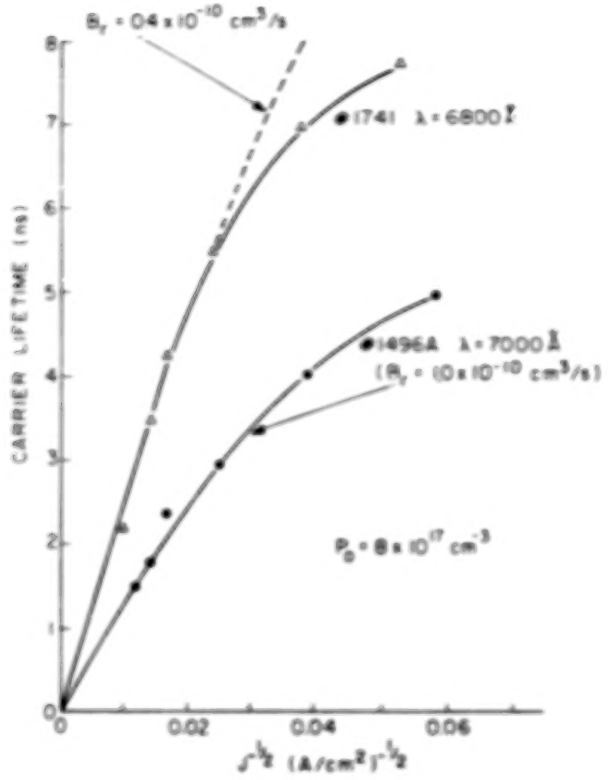

Figure 28. Carrier lifetime determined by luminescence decay measurements vs $(1/J)^{1/2}$. Slope of curves near origin yield value of radiative recombination coefficient B_r, as indicated in Eqs. (2) and (3).

Note in Fig. 28 that the theoretical curve for the 6800 Å diode at low current densities predicts spontaneous carrier lifetimes that are larger than actually observed. The difference is due to the effect of nonradiative centers that depress the carrier lifetime. Nevertheless, the lifetime values of 5 to 8 ns are not much lower than those observed in thin double-heterojunction lasers of (AlGa)As/GaAs [25].

3. Spontaneous Emission

Representative spectra at 22°C of a 6800 Å laser are shown in Fig. 29 as a function of current. Two bands, separated by about 200 Å, are seen below the lasing threshold, with the lasing peak emerging from the longer-wavelength band. The short-wavelength (high-energy) emission band is close in peak energy

25. M. Ettenberg and H. Kressel, J. Appl. Phys. 47, 1538 (1976).

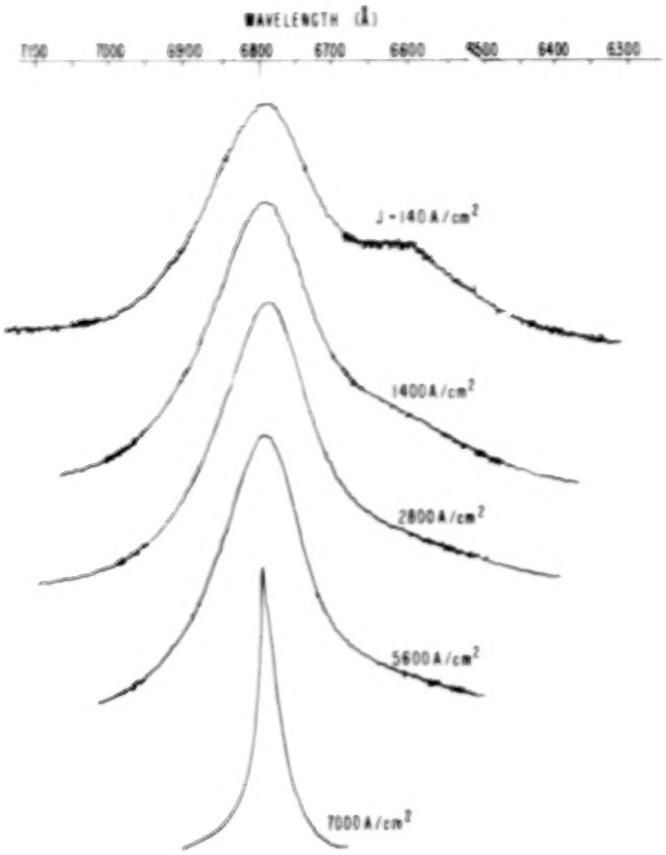

Figure 29. Emission spectra from 6800 Å laser at room temperature for several different values of current density.

to the bandgap energy, and therefore, is associated with transitions involving the conduction and valence bands. The origin of the two peaks and the low-energy emission, from which the lasing occurs, may be related to selective internal absorption combined with effective bandgap reduction and/or band-tailing effects at high injected carrier densities [26]. The 7000 Å lasers exhibited a similar behavior.

4. Pulsed Laser Characteristics

The lasers studied here were fabricated in broad-area form (by sawing two sides of the diodes) and in stripe-contact form, each having Fabry-Perot cavity lengths of ∿ 300 μm. The stripe devices used the oxide-isolated process with stripe widths of about 13 μm. Because we will be concerned only with two

26. H. Kressel, H. F. Lockwood, F. H. Nicoll and M. Ettenberg, IEEE J. Quantum Electron QE-9, 383 (1973), and references therein to earlier work.

mission wavelengths, we will refer to the "7000 Å" and "6800 Å" lasers when their respective properties are discussed. The threshold and efficiency data presented, unless noted otherwise, were obtained in pulsed operation at a duty cycle of 0.1%.

In the following, we describe some of the key characteristics of the lasers as a function of temperature. Figure 30 shows the lasing spectra as a function of increasing temperature for one 6800 Å device whose threshold current density increased from 6600 A/cm^2 at 22° to 12,300 A/cm^2 at 70°C. Figure 31 shows that the lasing peak shifts above room temperature at a rate of -5.7×10^{-4} eV/K.

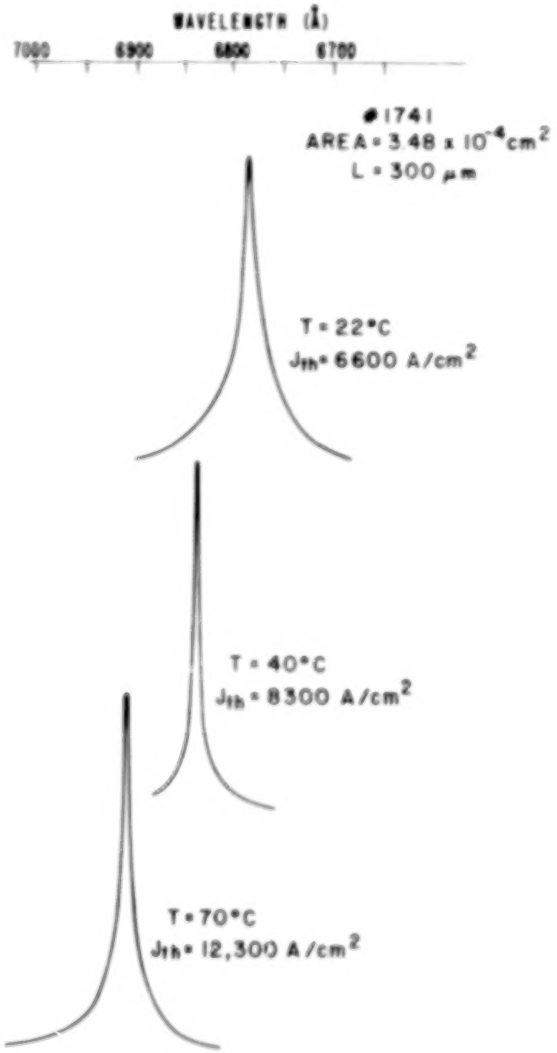

Figure 30. Laser spectra of 6800 Å laser at ambient temperatures of 22, 40 and 70°C.

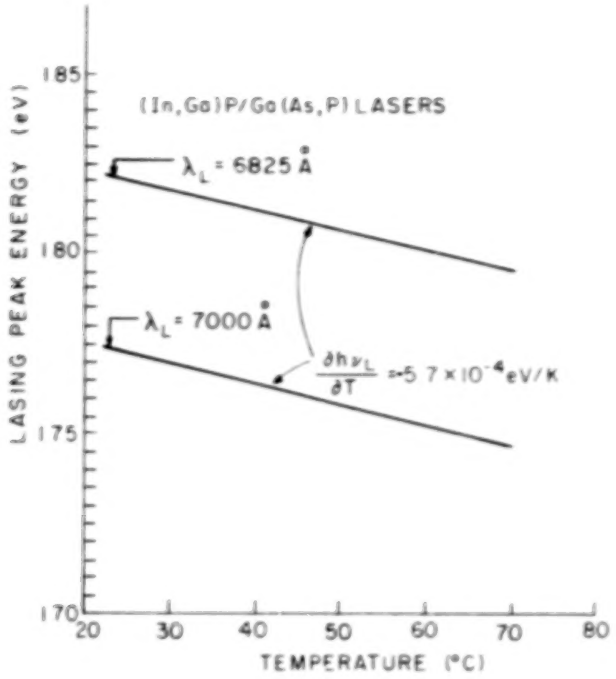

Figure 31. Temperature dependence of laser emission energy for 6800 and 7000 Å heterojunction lasers. Slope value, $\Delta h\nu/\Delta T$ = - 5.7 X 10^{-4} eV/K.

The lowest room-temperature threshold current densities (~ 3400 A/cm^2) were obtained with devices emitting near 7000 Å, as shown in Fig. 32. (Devices made from material similar to the 7000 Å laser were found to be capable of cw operation near room temperature.) A significant difference between the 6800 and 7000 Å lasers is in the temperature dependence of their threshold current density and differential quantum efficiency. Figure 33 shows comparative plots for the two types of lasers. For the 6800 Å lasers, the threshold current density increases by a factor of 1.8 between 22 and 70°C, compared to a factor of 1.5 for the 7000 Å devices. The differential quantum efficiency is also more temperature dependent for the 6800 Å lasers, decreasing from 20 to 12% between 22 and 70°C. The efficiency remains at 26% (emission from both sides) for the 7000 Å lasers. The stronger temperature dependence for the 6800 Å lasers is due to the increased GaP content in their Ga(AsP) recombination region, which brings this material within about 0.16 eV of the direct-indirect transition at room temperature. At elevated temperature, the increased thermal energy as well as the weaker temperature dependence of the (111) indirect conduction-band minima further increases the loss of electrons

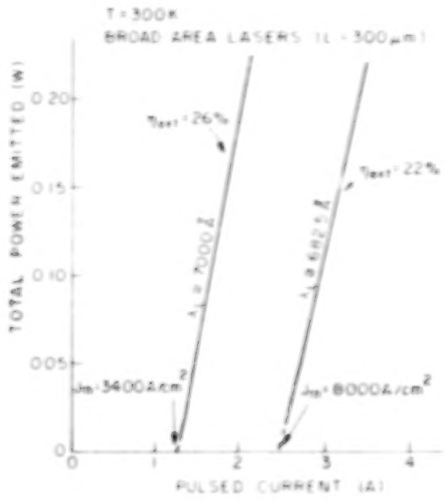

Figure 32. Total power emission (from both facets) vs pulsed current amplitude for representative high quality 6800 and 7000 Å lasers at room temperature.

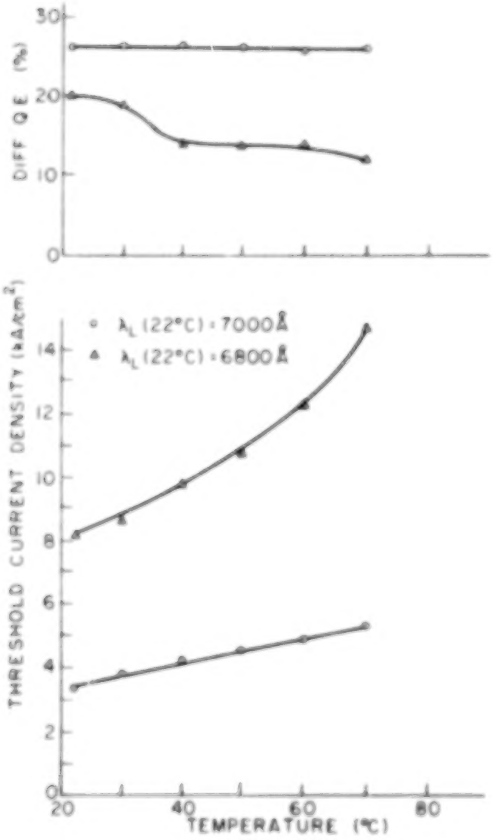

Figure 33. Temperature dependence of threshold current density and differential quantum efficiency for 6800 and 7000 Å Ga(AsP)/(InGa)P heterojunction lasers.

from the direct (000) minimum to the indirect minima, thereby reducing the internal efficiency and increasing the threshold current of the laser. The Ga(AsP) alloy composition of the 7000 Å lasers is far enough removed from the direct-indirect transition to not be appreciably affected by it; the weak temperature dependences observed for the 7000 Å lasers are therefore comparable to those of (AlGa)As heterojunction with similar confining bandgap steps [27].

The angular beam width $\theta_\perp$ of the lasers in the direction perpendicular to the junction plane (the transverse direction) of both types of lasers ranged from 56 to 50° at the half-power point. The radiation is strongly TE polarized, as is generally the case in double-heterojunction lasers, with a ratio of TE to TM polarization of 15 dB. The far-field in the plane of the junction is not particularly noteworthy, having the usual complex structure associated with the many lateral modes of sawed-side lasers.

5. CW Laser Operation

With regard to continuous-wave operation, the only lasers that were capable of such operation near room temperature were stripe-contact devices. Figure 34 compares the pulsed and cw operation of the same laser at a heat sink temperature of 10°C, the highest temperature at which we obtained sustained cw operation [28]. However, such sustained operation was found to produce facet damage. Apparently, the present devices are more susceptible to such damage than (AlGa)As lasers of comparable dimensions and with comparable power emission (about 5 mW from one facet). Facet coatings should reduce this problem [29].

Preliminary life tests have been carried out for a few heterojunction lasers of Ga(AsP)/(InGa)P. In Fig. 35 we illustrate the relative light emission from one edge of a stripe-contact laser biased somewhat below laser threshold at a current density between 2500 and 5000 A/cm^2 at room temperature. The emission is seen to drop to about 70% after a few hundred hours, but to remain near this level for the remaining 2000 hours to date.

27. H. Kressel and M. Ettenberg, J. Appl. Phys. 47, 3533 (1976).
28. H. Kressel, G. H. Olsen, and C. J. Nuese, Appl. Phys. Lett. 30, 249 (1977).
29. I. Ladany, M. Ettenberg, H. F. Lockwood and H. Kressel, Appl. Phys. Lett. 30, 87 (1977).

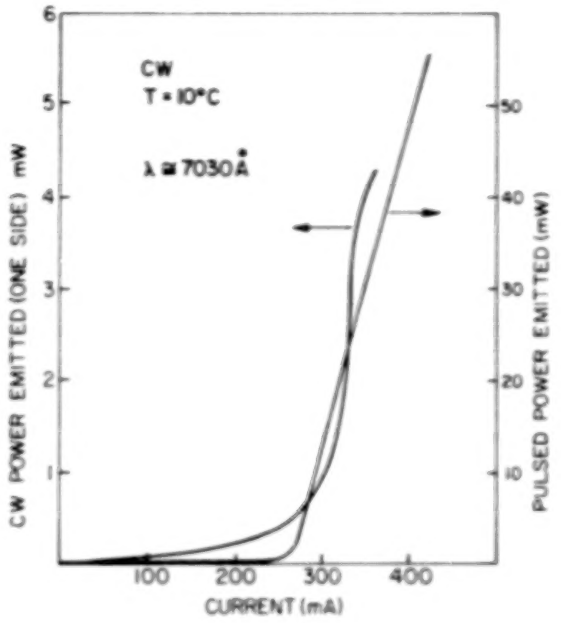

Figure 34. Power emitted as a function of current for a double-heterojunction Ga(AsP)/(InGa)P laser operating pulsed and cw at a heat sink temperature of 10°C.

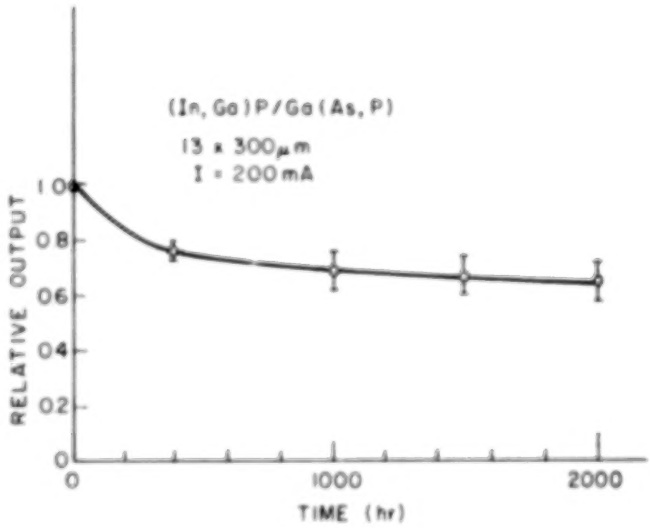

Figure 35. Relative light output vs operating time of four Ga(AsP)/(InGa)P heterojunction diodes biased between 2500 and 5000 A/cm^2 at room temperature. Emission was monitored from one edge of the stripe-contact diodes (13 μm stripe width).

D. DISCUSSION

Because of the larger direct-to-indirect energy bandgap transition of Ga(AsP), (1.99 eV), compared to (AlGa)As, (1.92 eV), the present device structure extends the possibilities of efficient room-temperature operation of laser diodes to wavelengths substantially shorter than those inherently possible with (AlGa)As structures. We estimate that the X and Γ conduction band separation should be at least 0.15 eV to allow for a reasonable internal quantum efficiency; thus, the limit for practical pulsed laser operation at room temperature is about 7000 Å for (AlGa)As, while it is about 6700 Å for a heterojunction structure with Ga(AsP) in the active region. A further reduction in the room-temperature lasing wavelength is possible with the incorporation of InGaAsP in the active region, using lattice-matching (InGa)P bounding layers. In fact, laser operation at 6500 Å with J_{th} = 20,000 A/cm^2 at 300 K has been achieved with such structures [30].

An overview of room-temperature laser diode operation is of interest in placing the present work in perspective. The emission now spans a wavelength range from the near-infrared (out to 1.7 μm) [30a] to the red spectral region. However, threshold current densities sufficiently low for cw operation (under about 4000 A/cm^2) have only been achieved at wavelengths greater than about 7000 Å. The sharp increase in threshold current at short wavelengths is due to the loss of electrons from the direct conduction-band minimum to the indirect minima as the direct-indirect transition is approached. The present Ga(AsP)/(InGa)P lasers have threshold current densities 3 to 8 times less than values for (AlGa)As due to the shorter-wavelength transition in Ga(AsP).

We now turn our attention to limitations present in the Ga(AsP)/(InGa)P structures, and means whereby improvements could be made. The present lasers have strong radiation confinement judging from the broad far-field beam in the direction perpendicular to the junction plane. We estimate on the basis of theory [33] that the radiation confinement within the thin active region bounded

30. L. M. Dolginov, L. V. Druzhinina, P. G. Eliseev, M. G. Mil'vidskii, and B. N. Sverdlov, Sov. J. Quantum Electronics 6, 257 (1976).
30a. J. J. Coleman, N. Holonyak, Jr., M. J. Ludowise, and P. D. Wright, Appl. Phys. Lett. 29, 167 (1976).
31. J. L. Butler and H. Krssel, RCA Rev., Dec. 1977.

by ~0.4 eV heterojunction barriers is approximately 70%. Of course, the carrier confinement is also strong. Thus, changes in the structure to improve either the radiation or carrier confinement cannot substantially reduce the threshold current density. However, metallurgical improvements should be helpful in improving the laser performance, particularly the reliability.

Inclined dislocations propagating from the substrate layer or other defects introduced during growth affect the internal quantum efficiency. Defects are easily introduced during growth. For example, a high density of defect loops has been observed via transmission electron microscopy near the active regions of some Ga(AsP) devices, as shown in Fig. 36. This figure (together with other related ones not shown) leads to the conclusion that the defects are dislocation loops on (111) planes with a vacancy character [32]. The loops were formed by the coalescence of vacancies produced by interfacial decomposition due to preferential evaporation of phosphorus during the preheat of the n-(InGa)P layer prior to growth of the n-Ga(AsP) active region. [33] These loops also can be detected at the top of each (InGa)P layer as a "black-white" contrast in the cross-section photo in Fig. 25; the morphology of the loops cannot be seen here, since the interface projects as a line (rather than a plane, as in the (111) view of Fig. 36). Note that the substrate -(InGa)P interface in Fig. 25 exhibits no decomposition because Ga(AsP) has a higher dissociation temperature than (InGa)P. The dislocation loops can be eliminated by using flows of the Group V carrier gas and lower temperatures during preheat. [33] However, an excess point defect concentration may always be present to some extent, and should be viewed as a potential failure mechanism in any III-V compound light-emitting device prepared at elevated temperatures.

The gradual degradation data presented here suggests that degradation phenomena are more prevalent in the present Ga(AsP) diodes than in conventional (AlGa)As ones. The most plausible reason for this difference in degradation rate is the presence of a higher defect density. There is, therefore, room for improvement in the metallurgy of these structures. It should be possible

---

32. P. B. Hirsch, A. Howie, R. B. Nicholson, D. W. Poshley and M. J. Whelen, *Electron Microscopy of Thin Crystals* (Butterworths, London, 1971).
33. G. Olsen and M. Ettenberg, *Crystal Growth: Theory and Techniques Vol. II*, C. Goodman ed. (Plenum Press, New York, 1978).

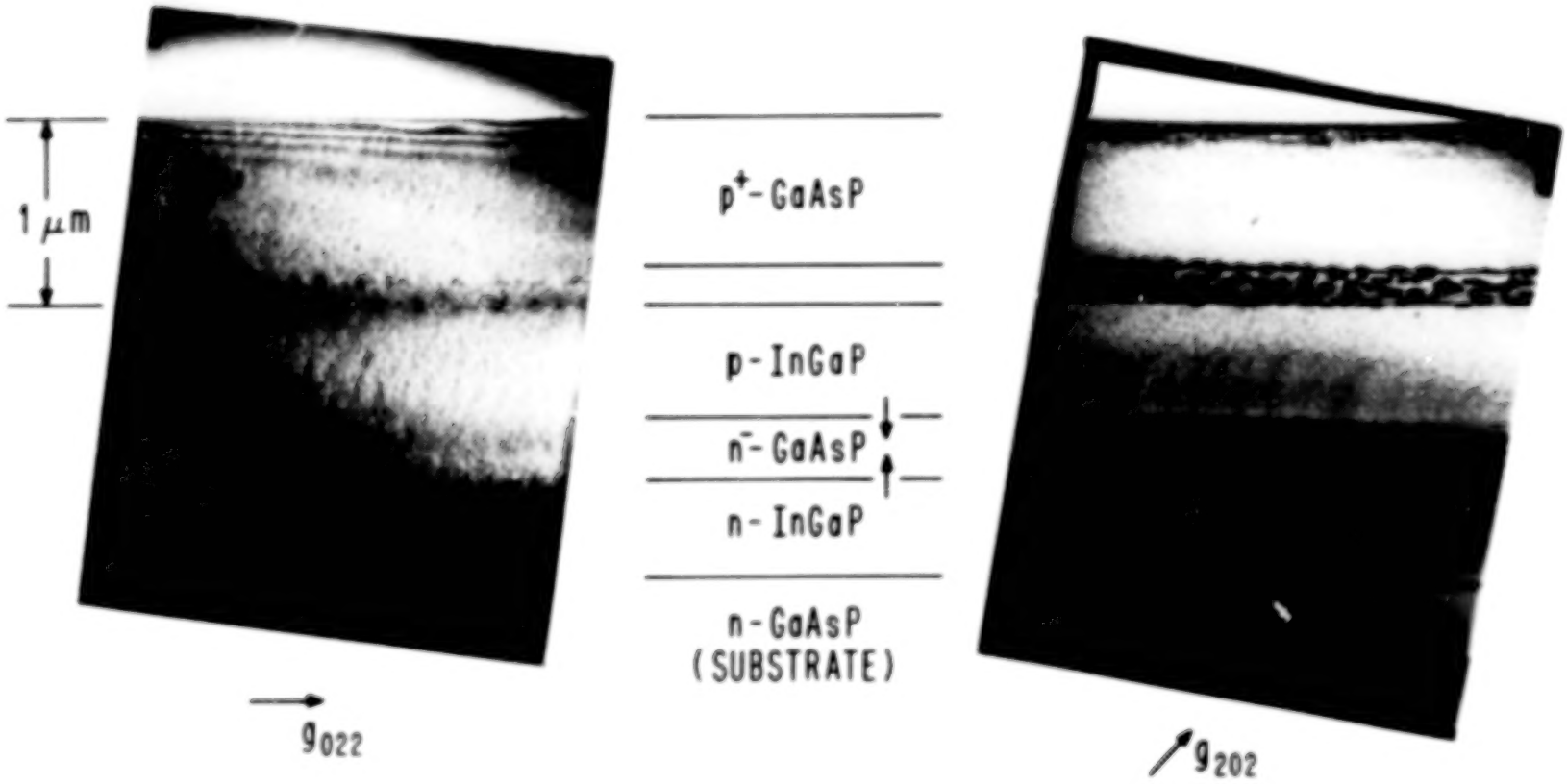

Figure 36. Cross-sectional (011) TEM micrograph of Ga(AsP)/(InGa)P heterojunction structure tilted to <111> to accentuate vacancy loops due to phosphorus during crystal growth.

to reduce the propagation of inclined dislocations from the substrate by using alternate substrate layers, e.g., (InGa)P step-graded in composition from a GaP substrate [34] rather than lattice-matching epitaxial layers to a substrate that contains inclined dislocations.

34. G. H. Olsen, M. S. Abrahams, C. J. Buiocchi, and T. J. Zamerowski, J. Appl. Phys. 46, 1643 (1975).

SECTION IV

LONG-WAVELENGTH (InGa)(AsP) QUATERNARY LASERS

A. INTRODUCTION

Although the (AlGa)As alloy system is presently adequate for many applications, the potential of silica fibers at wavelengths beyond 1.0 μm requires the development of lasers and photodetectors capable of efficient operation at these wavelengths. In particular, at wavelengths between 1.1 and 1.3 μm, silica fibers have reduced transmission losses, reduced pulse dispersion, and increased radiation resistance. For these reasons, a portion of our NASA-sponsored program was dedicated to the extension of the liquid-phase epitaxy process to the preparation of double-heterojunction laser structures of (InGa)(AsP), as described in detail in the sections below.

B. LPE GROWTH TECHNIQUE

With the LPE growth technique, we use a multiple-bin graphite boat provided with sliders, as illustrated schematically in Fig. 37. In our procedure, two InP substrates were used; the first saturated the melt, removed deposits from the bottom, and agitated the melt prior to growth. The second InP substrate served as the starting point for the multiple epitaxial layers forming the heterojunction laser structure. The first substrate, called the "precursor", had a <111> orientation, while the second, the growth substrate, was oriented either in the <111> or <100> direction. The In-rich melts were relatively large, about 5 grams each. Tin was used as the dopant for the n-type InP, Zn was used as the acceptor impurity for the p-type InP layer. The (InGa)(AsP) active layer was either Sn doped or was not intentionally doped (in which case, the background doping level was about 1×10^{17} cm^{-3}). The dopants were added directly to the melts prior to growth.

The process used for the epitaxial growth is illustrated in Fig. 38. The first step was a melt "homogenization", carried out typically at about 670°C for a time ranging between 10 minutes and 2 hours. As we discuss below, the dissociation of the InP substrate wafers during homogenization was found to be

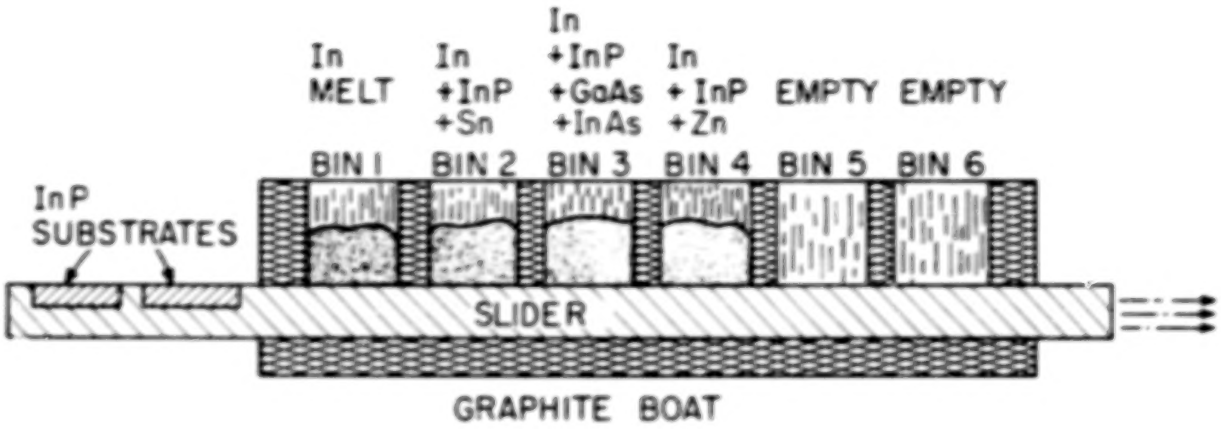

Figure 37. LPE growth technique using a multiple-bin graphite boat with sliders.

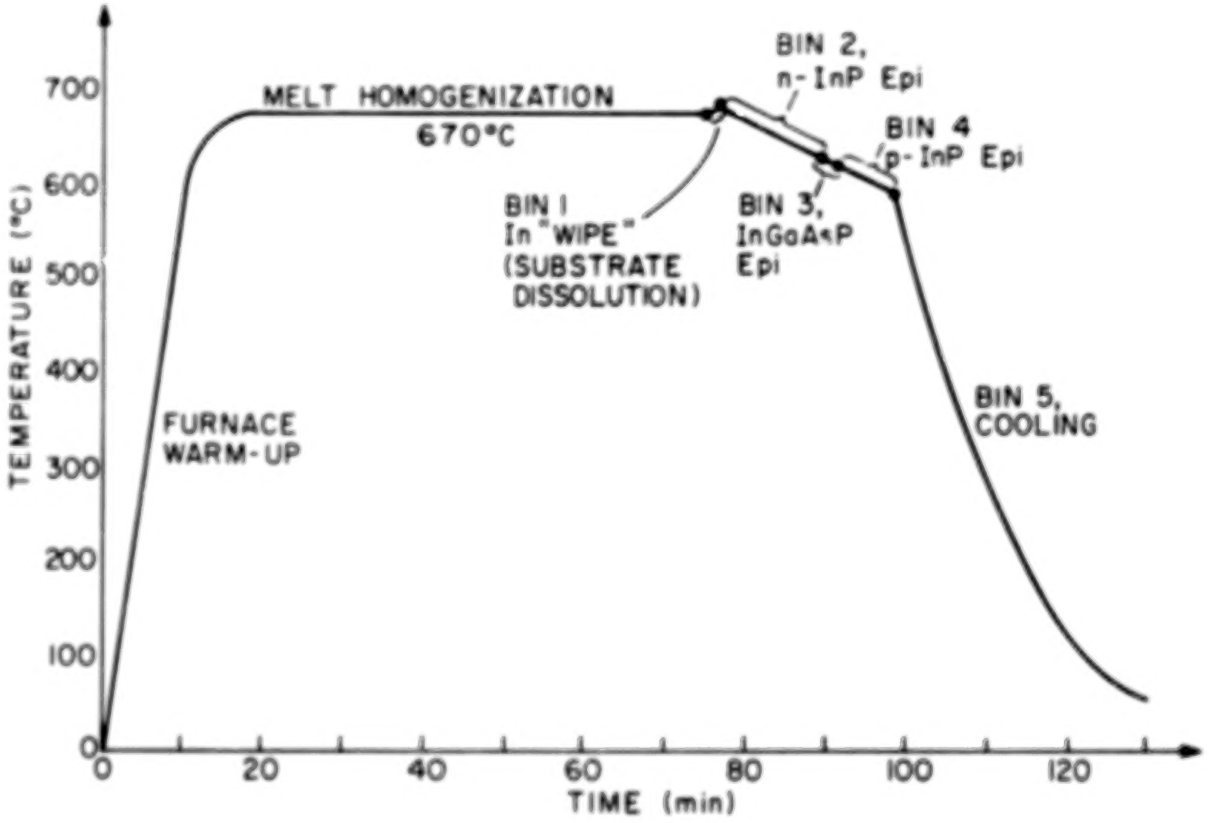

Figure 38. Graph depicting epitaxial growth process.

a severe problem, which we learned how to control during the course of this program. The next step, in bin #1, was an In "wipe", which dissolves some of the substrate and presents a fresh surface to the melt in bin #2, where the growth of the n-type InP confining layer occurs. The quaternary cavity is then grown in bin #3, and the p-type InP in bin #4. Before cooling, we sometimes grew a Zn-doped (InGa)(AsP) "cap" layer on the top of the p-type InP layers, in order to facilitate ohmic contact formation.

In the subsections below, we discuss some of the growth-related aspects of our (InGa)(AsP)/InP heterojunction laser technology. These include the reduction of lattice-misfit dislocation densities, the elimination of InP substrate dissociation, and the difficulty in completely removing In from the surface of the semiconductor after the wafer has passed through a melt.

1. Lattice Mismatch

The energy bandgap and the lattice constant of quaternary (InGa)(AsP) alloys can be independently varied, as shown in Fig. 39. Here, the lattice constant can be held at 5.869 Å to match that of InP (the dashed line), while the bandgap is varied between 1.35 eV (for InP) and 0.73 eV (for $In_{.53}Ga_{.47}As$). Most of the layers in the present program were designed for emission near 1.15 μm (E_g = 1.08 eV), requiring an alloy of $In_{.83}Ga_{.17}As_{.36}P_{.64}$.

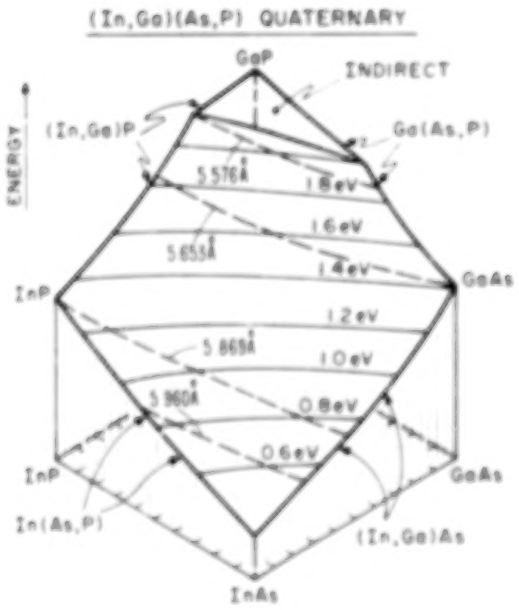

Figure 39. (InGa)/(AsP) quaternary alloys. Lattice constants are shown by dashed lines.

In the early stages of this program, the required amounts of In, InAs, InP, and GaAs placed into bin #3 (Fig. 27) were not known. Consequently, these layers often had either the improper energy bandgap or the improper lattice constant. When the latter occured, misfit dislocations were generated between the InP confining layers and the (InGa)(AsP) recombination region. These dislocations could be observed either by x-ray topography (as shown in Fig. 40)

(Scale = 2.0 mm)

Figure 40. X-ray topograph showing misfit dislocations between InP confining layers and the InGaAsP recombination region.

or by etching the surface with A-B etchant (as shown in Fig. 41). In both figures, the dislocation arrays provide the triangular pattern indicative of (110) slip planes intersecting the (111) surface of the wafer. As our work progressed, the correct melt concentrations for lattice matching were established and misfit dislocations array were no longer observed.

Figure 41. Lattice-mismatch dislocation arrays delineated with A-B etchant.

2. InP Substrate Dissociation

When a III-V compound is heated, the Group V element often has a higher partial vapor pressure than the Group III element, resulting in a preferential loss of the Group V species and resulting in globules of the Group III element left on the crystal surface. This is particularly true of phosphorus-containing compounds because of their high vapor pressure near the growth temperature. From the growth sequence in Fig. 38, it becomes apparent that dissociation

of the InP substrate is likely to occur during the melt-homogenization period; several samples were therefore studied in detail to determine the extent of InP dissociation during liquid-phase epitaxy. In Fig. 42, we illustrate two different InP wafers that were exposed to the melt-homogenization sequence, but were not passed through any of the melts. Figure 42(a) and (b) show the (111) InP surface that was exposed to H_2 at 670°C for 1 hour; Fig. 42(c) and (d) illustrate the same effect for the (100) InP surfaces. In the case of the (111) surface, the decomposition appears irregular, as if it were initiated at random points with no systematic spreading; the (100) surface shows rectangular pits characteristic of other III-V materials, for example GaAs (at higher temperatures).

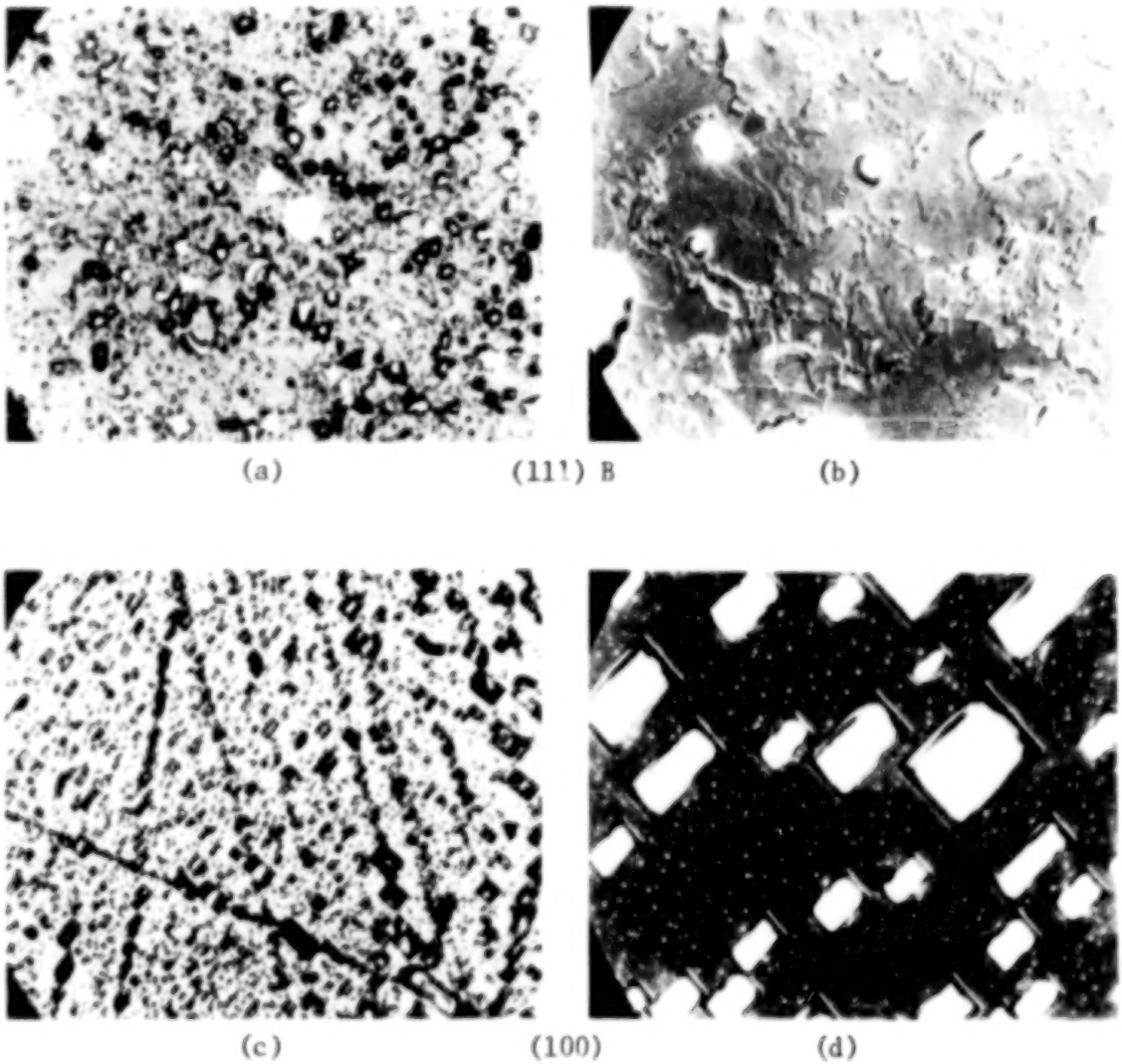

Figure 42. InP substrate dissociation. (a) and (c): 66X; (b) and (d): 825X. (1 hr. at 670°C in H_2).

A drastic reduction in decomposition occurs when the substrate is covered with an InP wafer that is left in place throughout the homogenization period until the substrate is pulled under the melt. As shown in Fig. 43, hardly any dissociation is evident in a <111>-oriented wafer held at 650°C for 30 minutes. Similar results also were obtained for 1 hour exposures and for <100>-oriented wafers.

Figure 43. Reduced dissociation with InP substrate covered (30 min at 650°C in H_2). Magnification: 1120X.

3. Indium Carry-Over

In examining some of the (InGa)(AsP) layers by x-ray topography (for lattice-mismatch dislocations), an unusual feature was observed, shown in Fig. 44(b). Here, a set of "worm-like" tracks are evident that can not be observed under normal optical microscopy, see Fig. 44(a). This observation prompted a study of the surface appearance of each epitaxial layer in the heterojunction structure, where we learned that the "tracks" were due to the motion of globules left on the surface of the wafer each time it passed

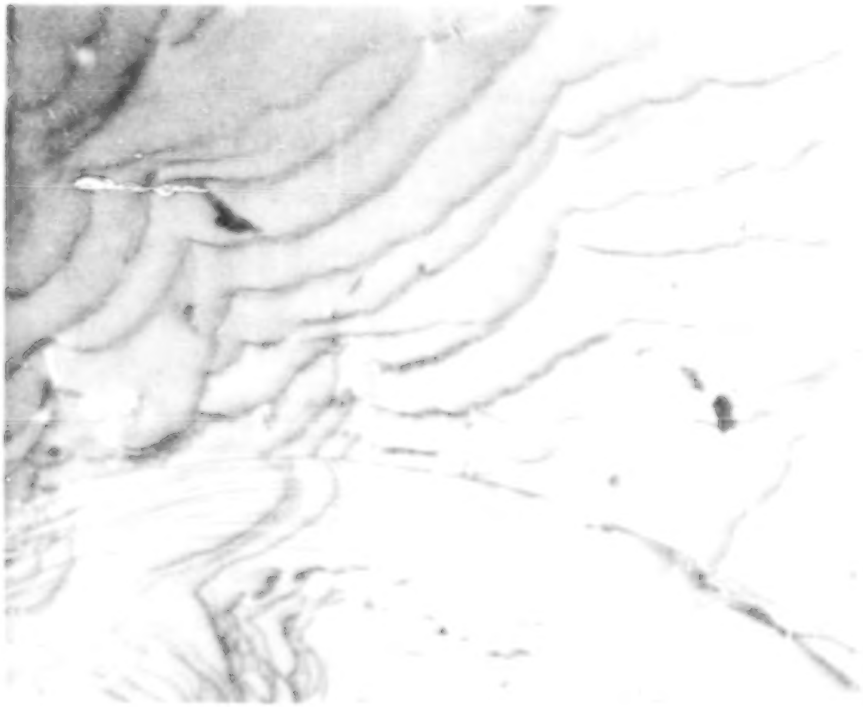

(a)

(b)

Figure 44. InGaAsP layers shown in x-ray topograph (b). "Worm-like" tracks cannot be observed under normal optical microscopy (a).

through a melt. The globules, shown in Fig. 45, have been identified as predominantly In; presumably, because of the high surface tension and relatively high viscosity of In at these temperatures, the boat partition is not always effective in cleaning up the surface. However, it was found that control of dissociation reduces the In carry over somewhat, which suggests that the surface roughness or the surface chemical condition influences the amount of In carry over.

Figure 45. Surface appearance of an undissociated substrate passed through In "wipe" melt for 20 s.

To reduce the carry-over problem described above, we rebuilt our LPE boats to reduce the clearance of the slider. The closer fit was found to reduce the amount of In carried over by decreasing the average size of the globules, however their density did not change appreciably.

C. CONTACTS

In processing our materials into lasers it became apparent that the poor nature of our metal contact to the p-type InP layer was adversely affecting device performance. A considerable effort was made to develop better contacts, leading ultimately to the use of an eutectic alloy of Au-Ge (Au 0.73: Ge 0.27) with a few percent of Zn added to it. These contacts were evaporated in vacuum and sintered in H_2 following evaporation. With the Au-Ge-Zn contacts, we typically obtained a device resistance of 1-2 Ω, which was comparable to those obtained earlier with Au-Zn alone. However, the triple alloy gave much more consistent results, with negligible contact failures, and better yield in diode mounting. A typical I-V characteristic for a standard device is shown in Fig. 46.

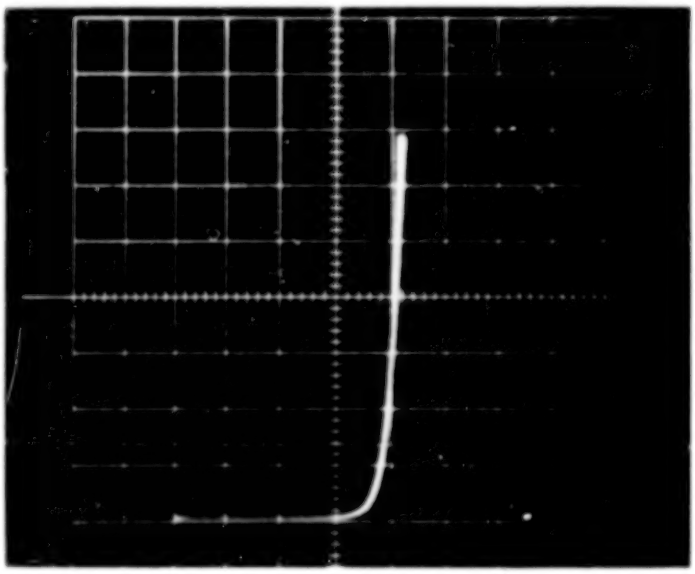

Figure 46. Typical forward bias I-V characteristic for a standard (InGa)(AsP)/InP heterojunction. 1 mA/div, vertical; 200 mV/div, horizontal.

D. DEVICE PROPERTIES

1. General Properties

The structure used for our (InGa)(AsP)/InP double-heterojunction lasers is shown schematically in Fig. 47. Here, the (InGa)(AsP) layer was not intentionally doped during growth, and attained a background doping level of about 1×10^{17} cm^{-3}. The Zn doping in the upper InP confining layer was experimentally optimized: for excessively large Zn concentrations, the Zn would

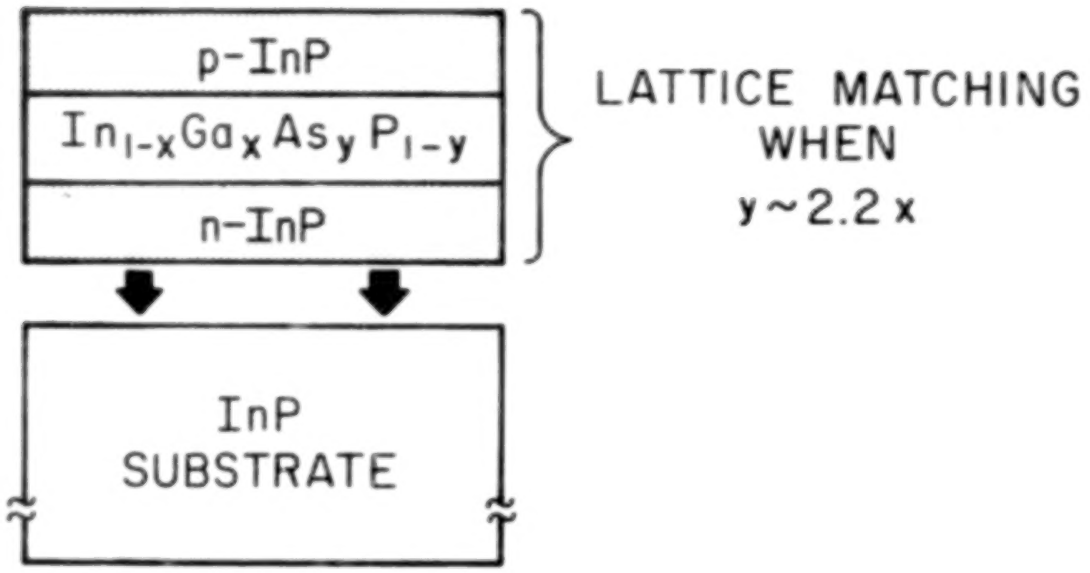

Figure 47. Schematic representation of lattice-matched heterojunction laser structure using quaternary (InGa)(AsP) active layer and InP confining layers.

diffuse through the thin (InGa)(As?) recombination region, thereby positioning the p-n junction in the lower n-type InP layer. For insufficient Zn concentrations in the p-type InP layer, the contact resistance to that layer would become excessive. A final value of about 5×10^{18} cm^{-3} was established as optimal for our structures.

The heterojunction structures were processed into both lasers and LEDs. In Fig. 48, we illustrate a cross section of a (110) cleavage plane that has been etched briefly with A-B etchant to delineate the layers. The planarity of each of the interfaces is seen to be good, with the recombination region being about 1.4 μm thick for this sample. In general, cavity thicknesses between about 0.3 and 2 μm were explored, with best results obtained for value of about 0.5 μm.

Figure 49 shows the emitted power from one edge of a spontaneous emitter (LED) as a function of drive current. The efficiency obtained, ~0.5%, is very good, considering that the output from only one edge was measured. Thus, the

Figure 48. <110> cross section of InGaAsP/InP LPE laser structure delineated with A-B etch.

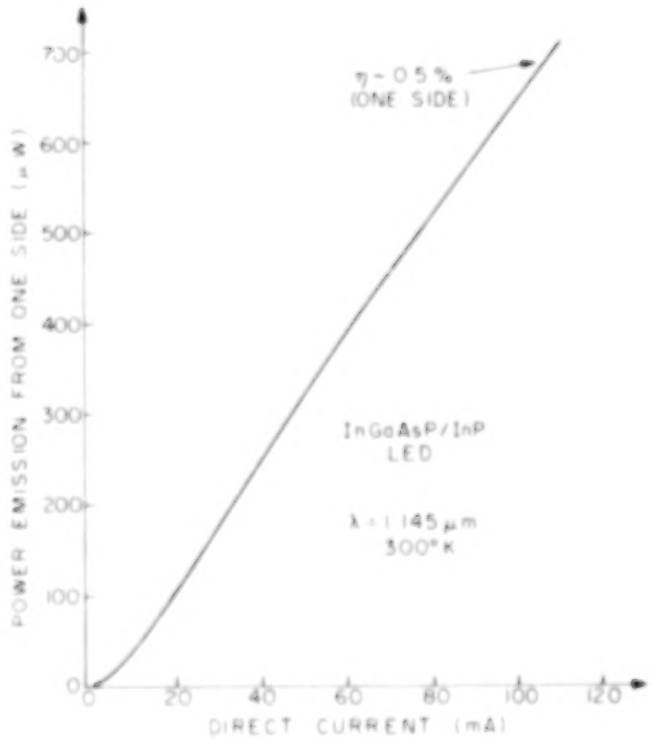

Figure 49. Emitted power from one edge of a spontaneous emitter (LED) as a function of drive current.

output collected from all 4 edges would raise η to about 2%. Furthermore, special contacting processes, such as the ones developed for commercial LEDs, would probably double the output to the 4% range. It appears, therefore, that a very efficient spontaneous emitter can be obtained from our material. In fact, a few such samples were coupled to silica fibers with more than 30 μW of power being measured at the fiber exit.

Turning to laser properties, in Table 4 we show a list of wafers with corresponding threshold currents, wavelengths, and efficiencies where available. Threshold current densities for the last several months of this program have consistently been less than 10,000 A/cm^2 with the best value (Sample 829) being 5000 A/cm^2 at room temperature. External differential quantum efficiencies (from one emitting facet) ranged from 16 to 36%, which is reasonable for these preliminary structures. In Fig. 50(a), we illustrate the power-current dependence for the 5000 A/cm^2 laser, while in Fig. 50(b), we show the longitudinal mode structure from the same laser. The longitudinal modes are separated by about 4.9 Å. For the Fabry-Perot spacing used here (295 μm), an effective refractive index $[n - \lambda(\frac{dn}{d\lambda}) = \lambda^2/2L\Delta\lambda]$ value of 4.27 is calculated. This value is very close to the value of 4.1 reported for our InGaAs/InGaP vapor-grown heterojunction lasers with an emission wavelength near 1.06 μm.

Finally, in Fig. 51, we illustrate the lateral and transverse far-field patterns of sample 829, the lowest-threshold structure. The transverse mode pattern is fundamental, indicative of a cavity thickness less than about 1 μm. The half-width values of 20° and 35° are sufficiently small to be useful for fiber-optic coupling.

2. Temperature Dependence of Laser Characteristics

The magnitude of the energy-bandgap step between the (InGa)(AsP) active layer and the InP confining layers of our heterojunction structures is a strong function of the (InGa)(AsP) alloy composition, or, equivalently, a strong function of the laser emission wavelength. For (InGa)(AsP) alloys selected for emission near 1.1 μm (a typical wavelength for the structures prepared to date), the bandgap step, ΔE_g, is equal to 0.233 eV (1.35 eV - 1.117 eV) at room temperature.

TABLE 4. LPE (InGa)(AsP)/InP LASERS

Material	Orientation	$J_{th}(A/cm^2)$	$\lambda_g(\mu m)$	$\eta(\%)^*$
775B	(111)	8840	1.140	-
782	(111)	9130	1.23	-
821	(111)	8080	1.19	16
822	(100)	8000	1.15	-
825	(100)	7800	1.18	-
827	(100)	6700	1.14	-
829	(100)	5000	1.11	26
831	(100)	6160	1.135	22
832	(100)	7270	1.145	-
834	(100)	6700	1.135	-
836	(100)	7000	1.21	36

*Differential quantum efficiency measured from one facet.

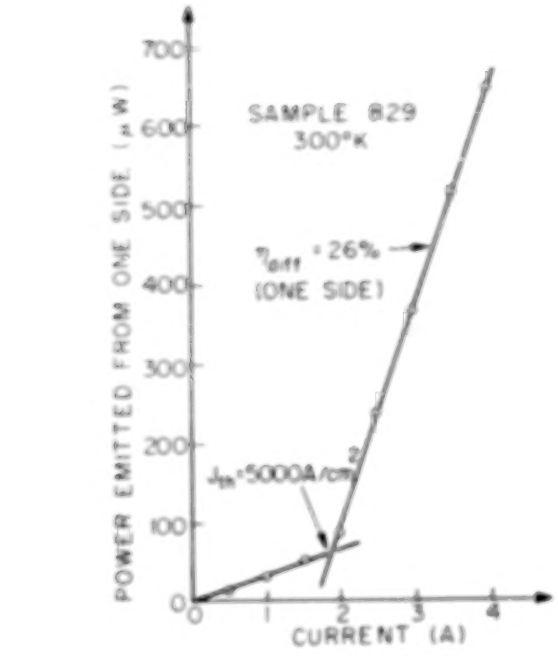

(a)

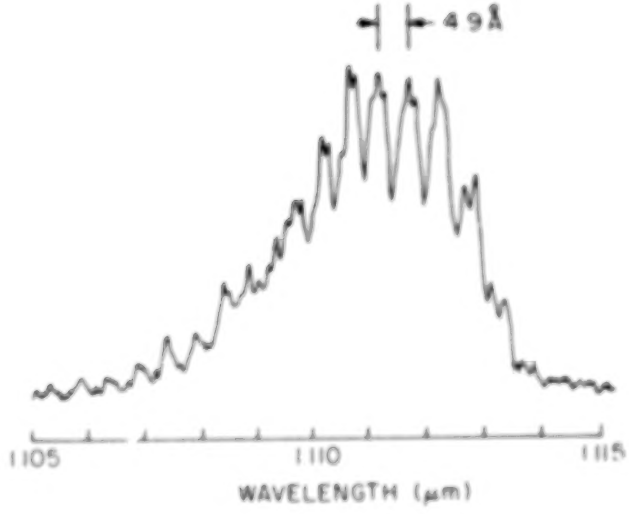

(b)

Figure 50. (a) Power-current dependence for the 5000 A/cm^2 laser. (b) Longitudinal mode structure.

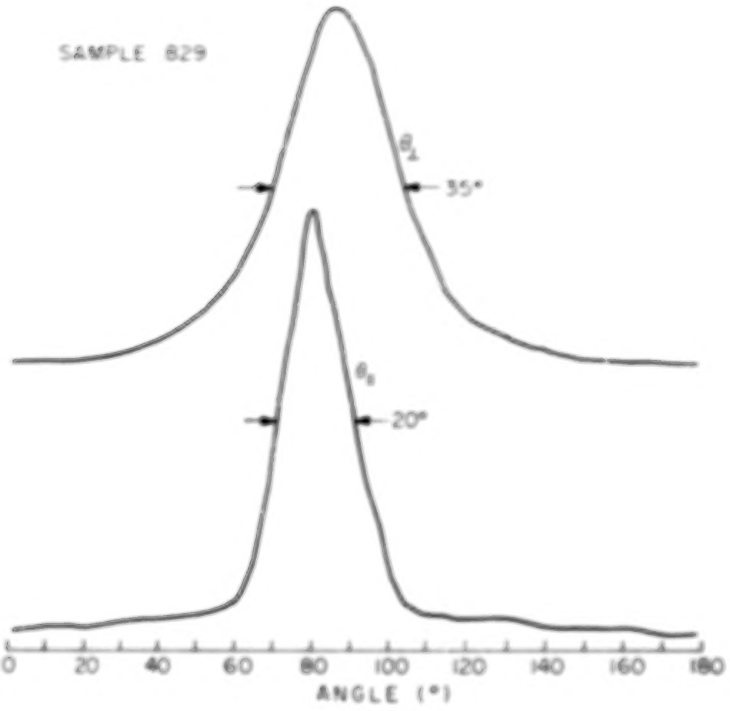

Figure 51. Lateral and transverse far-field patterns of sample 829.

One loss mechanism that becomes significant as the bandgap step becomes small is carrier "leakage" out of the (InGa)(AsP) layer and into the adjoining InP layers. The leakage current, I_ℓ, due to this mechanism is proportional to the term $\exp(-\Delta E_g/kT)$; hence, the leakage current increases appreciably for small E_g or at high temperatures. The increased leakage current results in higher laser threshold currents and lower conversion efficiencies.

To explore this effect in (InGa)(AsP), the (pulsed) threshold current and differential external efficiency were measured between 0°C and 70°C for one of our best (InGa)(AsP)/InP lasers (sample 829); these parameters, normalized with respect to their values at 0°C, are illustrated in Fig. 52. Similar data have been taken for heterojunction lasers of (AlGa)As, and are compared with our (InGa)(AsP) data in Fig. 53. In Fig. 53(a), we summarize the ratio of J_{th} at 70°C to that at 22°C, while in Fig. 53(b) similar ratios of efficiency are plotted. Although these data were originally presented as a function of the step in (AlGa)As alloy composition, Δx, the corresponding step in energy bandgap is easily determined from the known relationship between

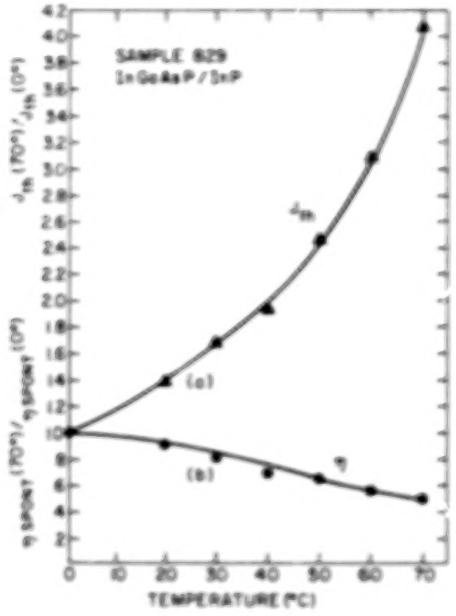

Figure 52. (a) Ratios of J_{th} at 70°C to that at 0°C for (InGa)(AsP)/InP laser at 1.1 μm. (b) Ratio of η at 70°C to that at 0°C for the same (InGa)(AsP)/InP laser.

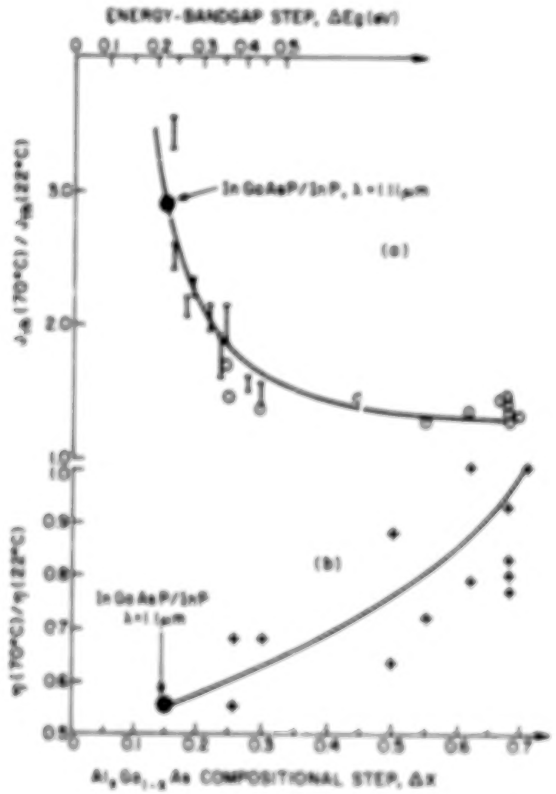

Figure 53. (a) Ratio of threshold current at 70°C to that at 22°C for (AlGa)As heterojunction lasers vs the magnitude of the composition step. Data with error bars are from Goodwin, et al., as the ratio between 65 and 10°C. (b) Ratio of laser efficiency at 70 and 22°C for (AlGa)As heterojunction.

bandgap and composition. The energy bandgap step, ΔE_g, is also shown on the horizontal axis of Fig. 53 so that the threshold current and efficiency ratios for (InGa)(AsP)/InP can be added. It is immediately apparent that our data fit that for (AlGa)As quite well; the large ratios for the (InGa)(AsP)/InP structures are indicative of signicant leakage currents at elevated temperatures, as expected from the relatively small energy-bandgap step.

The experimental (AlGa)As data in Fig. 53 can be applied to the (InGa)(AsP)/InP system by plotting the threshold and efficiency ratios vs ΔE_g and by relating ΔE_g to the emission wavelength for (InGa)(AsP)/InP. This is shown in Fig. 54, where it is apparent that the threshold and efficiency ratios are adversely affected by leakage currents out to wavelengths as long as about 1.3 μm. We hasten to add that this does not mean that reasonable thresholds and efficiencies are precluded at room temperature, but rather that these parameters will suffer at elevated temperatures. However, since a temperature rise necessarily occurs as the duty cycle of heterojunction lasers is increased, Fig. 54 does suggest that cw operation at room temperature might be more difficult to control in (InGa)(AsP)/InP structures with $\lambda \lesssim 1.2$ μm than in conventional (AlGa)As. CW operation at elevated temperatures also would be expected to suffer to some extent.

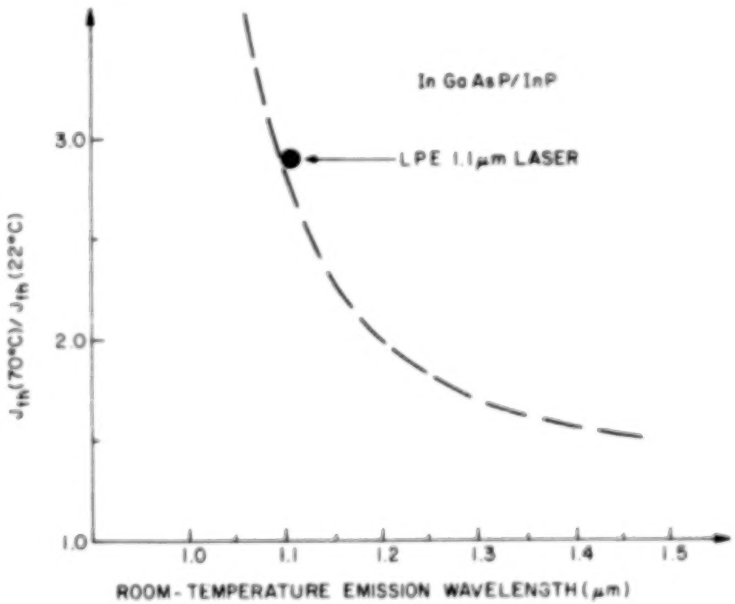

Figure 54. Ratio of laser threshold current at 70 and 22°C for (InGa)(AsP)/InP double-heterojunction lasers vs the room-temperature emission wavelength. The curve is based on experimental observations of such ratios for (AlGa)As/GaAs lasers.

E. RELIABILITY

Although the technology of the (InGa)(AsP)/InP structures is still new, a few of the early devices were placed on lifetest at room temperature. All of the data available so far are for incoherent emitters (LEDs) fabricated by cleaving small chips (with broad contact areas) from the double-heterojunction laser structures. Diodes from two different wafers have been run, the results of which are shown in Figs. 55 and 56. Although, an *initial* drop of 50% occurred for one diode, in general the life is very promising for the 5000 h thus far accumulated in the lifetest.

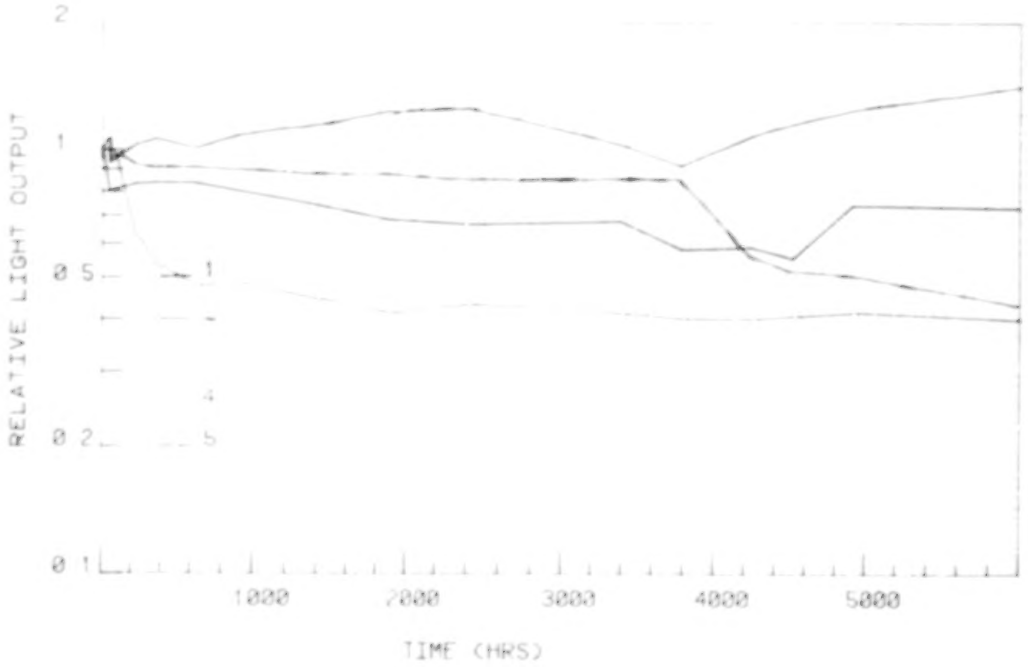

Figure 55. Life test results on (InGa)(AsP)/InP LEDs.

Based on the preliminary results above, we tentatively conclude that our (InGa)(AsP)/InP LED performance is excellent. Since degradation mechanisms for LEDs and lasers are similar, one may eventually expect good laser performance from such devices. The reason we have not yet obtained such data is that the thresholds are somewhat high for cw operation. Our general experience with (AlGa)As lasers suggests that thresholds should be no higher than 3000 A/cm^2 for successful cw operation.

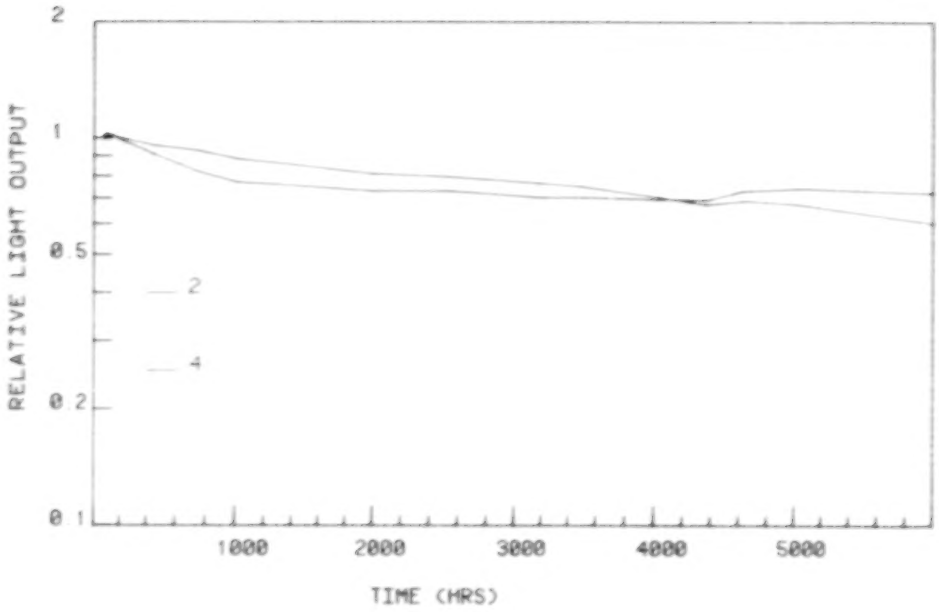

Figure 56. Life test on another (InGa)(AsP)/InP wafer. diodes were operated as LEDs.

SECTION V

CONCLUSIONS

This program deals with the extention of injection laser performance to a wider spectral region than that presently available with (AlGa)As heterojunction lasers (0.75 - 0.90 μm). In the (AlGa)As system, cw laser operation was obtained at wavelengths in the 7200 - 7300 Å range. For these structures, difficulties were encountered in doping and in reliability (for the shortest wavelengths). A double-doping scheme, based on the simultaneous introduction of Zn and Ge dopants into the p-type (AlGa)As confining layer, was shown to lead to dramatic improvements in *incoherent* diode life at short wavelengths, but this scheme has not yet been studied in regard to improving cw laser reliability.

For longer-wavelength (0.8 - 0.85 μm) (AlGa)As lasers, reliability seems to be dependent on facet passivation, which was successfully accomplished using Al_2O_3 half-wave films. Lasers prepared with such facet passivation have accumulated over 25,000 hours of continuous operation to date. From accelerated lifetests on these devices at temperatures up to 90°C, an extrapolated room-temperature life of about 10^6 hours has recently been obtained.

Macroscopic as well as microscopic fluctuations in composition have been found to arise in (AlGa)As ternary materials. Although these are small ($\Delta x \approx 0.016$), the fluctuations might adversely affect device performance; most important is the role they might play in causing variations in device performance within a wafer and in degrading mode stability.

A careful study was made of the effect of stripe width on the threshold current of oxide-isolated stripe-contact (AlGa)As lasers. Design curves were obtained showing the effect of various laser parameters; these aid in the fabrication of lasers with the minimum threshold current, which for our typical structures occurs for a stripe width of ≈8 μm. Below this value some not-well-understood effects cause a rapid increase in threshold current.

The Ga(AsP)/(InGa)P system has been used to extend laser performance to 6800 Å. These structures are vapor deposited epitaxially on commercial $GaAs_{0.7}P_{0.3}$ substrates. Good device performance was obtained, as judged by

TEM studies, diode spontaneous lifetime, and other measurements. Various laser properties were measured and shown to be generally similar to those in (AlGa)As lasers. Threshold current densities as low as 3.4 kA/cm^2 at 7000 Å allowed cw operation close to room temperature. Rapid facet damage was observed during these tests, which we believe can be prevented by facet coatings. In the incoherent mode, reasonable operating life was obtained for 2000 hours to date, although a gradual degradation is evident. This is believed to be due to a higher defect density in this material, compared to (AlGa)As. One type of defect, inclined dislocations propagating from the substrate, can be reduced by using a GaP substrate and (InGa)P step-grading layers.

The third system studied was (InGa)(AsP)/InP grown by liquid-phase epitaxy. Details of our growth process have been described. Attention was drawn to several aspects of the growth technology, particularly indium pullover, substrate dissociation, and lattice matching. A new contact process utilizing Au-Ge-Zn alloys was described. LEDs were fabricated showing ~2% efficiency and no degradation over the 6000 hours accumulated so far. The lowest lasing threshold current density was 5 kA/cm^2, which was somewhat large for cw operation. It is believed that with minor adjustments in our present growth schedule, the threshold current density can be reduced to the 2 kA/cm^2 range required for cw operation.

Finally, the small energy-bandgap step between the (InGa)(AsP) recombination region and the adjoining InP confining layers has been shown to increase threshold currents and decrease laser efficiencies at elevated temperatures. Such effects are particularly deleterious for (InGa)(AsP)/InP lasers with emission wavelengths between 1.05 and 1.1 μm, where the energy-bandgap step becomes quite small.

REFERENCES

1. A. Onton, M. R. Lorenz, J. M. Woodall and R. J. Chicotka, J. Cryst. Growth 27, 166 (1974).
2. D. B. Holt, in *Quantitative Scanning Electron Microscopy*, D. B. Holt, M. D. Muir, P. R. Grant and I. M. Boswarva, eds. (Academic Press, New York, 1974), Chapter 10.
3. D. F. Kyser and D. B. Wittry, in *The Electron Probe*, T. D. McKinley, K. F. J. Heinreich and D. B. Wittry, eds. (Wiley & Sons, New York, 1964), p 691; D. F. Kyser and D. B. Wittry, J. Appl. Phys. 35, 2439 (1966).
4. D. B. Wittry, Appl. Phys. Lett. 8, 142 (1966).
5. H. C. Casey, J. Electrochem. Soc. 114, 153 (1967).
6. H. Johansen and F. P. Herrman, Kristall u. Technik 7, 1135 (1972).
7. H. F. Lockwood and M. Ettenberg, J. Cryst. Growth 15, 82 (1972).
8. M. Cole and D. Ryer, Electro-Optical Systems Design, 6/72, p 16-19.
9. A. Many, Y. Goldstein and N. B. Grover, *Semiconducting Surfaces* (North Holland Publ. Co., Amsterdam, 1965).
10. I. Ladany, H. Kressel and C. J. Nuese, NASA Contractor Report CR-2823, April 1977, (The National Information Service, Springfield, VA. 22151).
11. M. Ettenberg, H. S. Sommers, Jr., H. Kressel, and H. F. Lockwood, Appl. Phys. Lett. 18, 571 (1971).
12. H. Kressel and I. Ladany, RCA Rev. 36, 230 (1975).
13. I. Ladany and H. Kressel, Appl. Phys. Lett. 25, 708 (1974).
14. P. Petroff and R. L. Hartman, J. Appl. Phys. 45, 3899 (1974).
15. For a review of degradation phenomena see H. Kressel and J. K. Butler, *Semiconductor Lasers and Heterojunction LEDs* (Academic Press, 1977), chapter 16.
16. A. R. Goodwin, P. A. Kirkby, M. Pion, and R. S. Baulcomb, IEEE J. Quant Elect. QE-13, 696 (1977).
17. A. R. Goodwin, J. R. Peters, M. Pion, G. H. B. Thompson, and J. E. A. Whiteaway, J. Appl. Phys. 46 3126 (1975).
18. Taibun Kanajima, Koichi Ishida, and Junji Matsui, Japan, J. Appl. Phys. 16, 233 (1977).
19. P. A. Kirkby, IEEE J. Quant. Elect. QE-11, 562 (1975).
20. C. J. Nuese, M. Ettenberg, and G. H. Olsen, Appl. Phys. Lett. 25, 612 (1974).
21. C. J. Nuese, G. H. Olsen, M. Ettenberg, J. J. Gannon, and T. J. Zamerowski, Appl. Phys. Lett. 29, 807 (1976).

22. J. F. Womac and R. H. Rediker, J. Appl. Phys. 43, 4129 (1972).

23. H. Namizaki, H. Kan, M. Ishii and A. Itoh, Appl. Phys. Lett. 24, 486 (1974).

24. J. P. Wittke, N. Ettenberg and H. Kressel, RCA Rev. 37, 159 (1976).

25. M. Ettenberg and H. Kressel, J. Appl. Phys. 47, 1538 (1976).

26. H. Kressel, H. F. Lockwood, F. H. Nicoll and M. Ettenberg, IEEE J. Quantum Electron QE-9, 383 (1973), and references therein to earlier work.

27. H. Kressel and M. Ettenber, J. Appl. Phys. 47, 3533 (1976).

28. H. Kressel and G. H. Olsen, and C. J. Nuese, Appl. Phys. Lett. 30, 249 (1977).

29. I. Ladany, M. Ettenberg, H. F. Lockwood and H. Kressel, Appl. Phys. Lett. 30, 87 (1977).

30. L. M. Dolginov, L. V. Druzhinina, P. G. Eliseev, M. G. Mil'vidskii, and B. N. Sverdlov, Sov. J. Quantum Electronics 6, 257 (1976).

30a. J. J. Coleman, N. Holonyak, Jr., M. J. Ludowise, and P. D. Wright, Appl. Phys. Lett. 29, 167 (1976)

31. J. K. Butler and H. Kressel, RCA Rev., Dec. 1977.

32. P. B. Hirsch, A. Howie, R. B. Nicholsen, D. W. Poshley and M. J. Whelen, *Electron Microscopy of Thin Crystals* (Butterworths, London, 1971).

33. G. Olsen and M. Ettenberg, *Crystal Growth: Theory and Techniques Vol. II*, C. Goodman, ed. (Plenum Press, New York, 1978).

34. G. H. Olsen, M. S. Abrahams, C. J. Buiocchi, and T. J. Zamerowski, J. Appl. Phys. 46, 1643 (1975).

Blank page

APPENDIX A

TOPOGRAPHICAL INVESTIGATION OF THE VARIATIONS IN STOICHIOMETRY IN $Ga_{1-x}Al_xAs$ USING ELECTROLYTE ELECTROREFLECTANCE

By Prof. Fred H. Pollak, Cajetan E. Okeke, and Prof. P. Raccah
Yeshiva University
Belfer Graduate School of Science
2495 Amsterdam Avenue
New York, NY 10033

Work done under
sub-contract with
RCA Laboratories.

Blank Page

ABSTRACT

We have developed a unique approach for evaluating the local compositon x as a function of position on the surface of crystals of $Ga_{1-x}A\ell_xAs$ utilizing electrolyte electroreflectance. The method is non-destructive and can be employed at room temperature. The technique is sensitive enough to determine change of compositon $\Delta x \approx 0.002$ with a spatial resolution of about 100μ. This approach has a number of advantages over the microprobe and luminescence techniques.

I. INTRODUCTION

We have developed a unique approach for measuring the local composition x as a function of position on the surface of crystals of $Hg_{1-x}Cd_xTe$ utilizing electrolyte electroreflectance (EER)[1]. The technique is non-destructive and can be readily employed at room temperature. The method is sensitive enough to determine changes of composition $\Delta x \approx 0.002$ for samples with a spatial resolution of about 100μ. This procedure is very useful for the selection of crystals for solid state lasers and can be used as a convenient analytical tool for evaluating crystalline material grown either in bulk form or as epitaxial layers, thus providing feedback for the adjustment of crystal growing parameters. Our method has a number of advantages over the microprobe and luminescence techniques. The EER approach to the determination of topographical stoichiometry has already been successfully applied to $Hg_{1-x}Cd_xTe$.[2]

It is well known that the energy of features in the optical spectra of semiconducting alloys of the type $A_{1-x}B_xC$ (e.g. $Ga_{1-x}Al_xAs$, $Hg_{1-x}Cd_xTe$, $In As_{1-x}Sb_x$, etc.) depend on the composition, x, in a continuous manner. Therefore, by measuring the changes in energy of a particular optical feature utilizing a small scanned light spot the variations in stoichiometry Δx, can be determined across the face of such a material. EER is particularly suited to such an investigation since it yields a sharp optical spectrum at room temperature, can be performed on a free surface (i.e., nothing need be deposited on the sample surface to apply the electric field) and hence is non-destructive.[1] In $Ga_{1-x}Al_xAs$ the most advantageous feature for our purposes is the E_0 structure (direct gap at $\vec{k} = 0$) since it gives a large EER signal, is in the convenient 2 eV

range and its dependence or composition is known[3]. Shown in Fig. 1 is the variation of the E_0 optical feature with composition x as determined from EER measurements[3] (in Ref. 3 the E_0 structure is labelled as peak #1).

II. EXPERIMENTAL DETAILS

In our investigation standard EER method was employed. This technique has been described extensively in the literature[1,2]. The samples were utilized without polishing or etching the surface. A contact was made to one edge of each sample using silver point and the sample was mounted individually on a glass slide with paraffin wax to insulate all but the front surface from the electrolyte. The slide was rigidly attached to an X-Y stage which was movable with a precision of 0.01 mm. The sample was dipped into an optical cell containing electrolyte and a platinum electrode. The electrolyte used was a 1:4 solution of glycerol in water[3]. Sample thickness were approximately 2μ. Light from a monochromator was focused to a spot size of about 100μ on the sample by means of an f/1.2 camera lens. This was verified by passing the beam through a 100μ slit without any loss of intensity.

Spectra in the region of the E_0 optical feature were taken with the light spot focused onto one portion of the sample. The sample was then moved by means of an X-Y stage and spectra taken in the new position. Step sizes were typically 0.2 mm in the horizontal (X) and the vertical (Y) directions. The shifts in the energy of the spectra were correlated with the known composition dependence of the E_0 peak in order to evaluate the change in composition Δx. (see Fig. 1). Shown in Fig. 2 is the electroreflectance spectra (ΔR/R) of the E_0 peak of a typical sample, i.e. sample #471 with a nominal value of x = 0.42.

III. EXPERIMENTAL RESULTS

Shown in Fig. 3a is a contour map of the variations in composition Δx of $Ga_{1-x}Al_xAs$ sample 471 as displayed by a Tektronix 4051 Basic Graphic system and reproduced by the hard copy unit. This sample was reported to have a nominal value of x = 0.42. The lowest measured value of the composition was arbitrarily taken as $\Delta x = 0.00$ and the contours are at intervals of $\Delta x = 0.002$. The lowest value of x($\Delta x = 0.00$) was found to have an energy of 1.9805 eV. From Fig. 1 this corresponds to x = 0.413. Figure 3a shows a region of relative non-uniformity in the lower left hand corner, with a maximum $\Delta x = 0.028$ (x = 0.441). Thus our determination is in reasonable agreement with the reported nominal. The rest of the crystal appears quite uniform. Shown in Fig. 3b is an expanded section of the lower left-hand section.

In Fig. 4a we have plotted the contour map of sample 472 with a reported nominal concentration of x = 0.54. For this sample $\Delta x = 0.00$ co-found to have an energy of 2.0957 eV, which corresponds to x = 0.490 from Fig. 1. Figure 4a shows a region of non-uniformity in the entire right hand section, the maximum variation in $\Delta x = 0.026$. This corresponds to an x = 0.516. Therefore, for this sample there is a substantial disagreement between the measured range of x and the reported nominal value. An expanded view of the lower right hand quadrant is illustrated in Fig. 4b.

The contours for sample 473, with a nominal reported value of x = 0.65, are shown in Fig. 5a. Note that the contours are taken at intervals of $\Delta x = 0.003$. In this case $\Delta x = 0$ corresponds to 2.3300 eV, which from Fig.1 gives a value of x = 0.620. This sample has large inhomogeneties across the entire region that was investigated. The maximum value of

TABLE OF CONTENTS

Section		Page	
I.	INTRODUCTION	1	1/A14
II.	(AlGa)As LASERS	3	1/B2
	A. Introduction	3	1/B2
	B. Material Properties	4	1/B3
	1. Electroreflectance Studies of Macroscopic Nonuniformities	4	1/B3
	2. Cathodoluminescence Study of Microscopic Nonuniformities	4	1/B3
	C. Analysis of Stripe Configuration	16	1/C1
	D. Laser Diode Properties	17	1/C2
	E. Reliability	23	1/C8
	1. Longer-Wavelength Lasers	23	1/C8
	2. Shorter-Wavelength Lasers	25	1/C10
III.	RED-EMITTING Ga(AsP)/(InGa)P HETEROJUNCTION LASERS	32	1/D3
	A. Introduction	32	1/D3
	B. Structures	32	1/D3
	C. Device Evaluation	35	1/D6
	1. Current-Voltage Characteristics	35	1/D6
	2. Spontaneous Carrier Lifetime	40	1/D13
	3. Spontaneous Emission	41	1/D14
	4. Pulsed Laser Characteristics	42	1/E1
	5. CW Laser Operation	46	1/E5
	D. Discussion	48	1/E7
IV.	LONG-WAVELENGTH (InGa)(AsP) QUATERNARY LASERS	52	1/E12
	A. Introduction	52	1/E12
	B. LPE Growth Technique	52	1/E12
	1. Lattice Mismatch	54	1/E14
	2. InP Substrate Dissociation	56	1/F2
	3. Indium Carry-Over	58	1/F4
	C. Contacts	61	1/F7
	D. Device Properties	61	1/F7
	1. General Properties	61	1/F7
	2. Temperature Dependence of Laser Characteristics	64	1/F10
	E. Reliability	70	1/G2
V.	CONCLUSIONS	72	1/G4
REFERENCES		74	1/G6
APPENDIXES			

$\Delta x = 0.024$ so that $x = 0.644$ in those regions. Thus for this sample there is reasonable agreement between the measured value of x and the reported nominal value. Shown in Fig. 5b is an expanded view of the lower left region.

Plotted in Fig. 6 are the contours for sample 475 [$x = 0.94$ nominal] with contours at intervals of $\Delta x = 0.02$. The value of $\Delta x = 0.00$ corresponds to an energy of 2.6651 eV which from Fig. 1 yields $x = 0.880$. Note that there is a solid narrow dark region running along the right hand side of Fig. 6 . We shall return to this section shortly. Apart from this area the maximum value of $\Delta x = 0.014$ which corresponds to $x = 0.894$. On the positions of the sample corresponding to the dark region it was found that the E_0 electroreflectance peak had an energy of 2.8832 eV which corresponds to $x = 0.940$. Therefore in this region there is good agreement between the measured and reported values of x. We also found another extremely interesting feature in this region, i.e. a change of phase of the EER signal ($\Delta R/R$) relative to the rest of the sample. This clearly indicates that in this region the sign of the carrier concentration is different from the rest of the sample.

IV. DISCUSSION OF RESULTS

We have demonstrated the feasibility of determining the topographical variations in $\Delta x \approx 0.002$ in $Ga_{1-x}Al_xAs$ utilizing the convenient non-destructive technique of EER. At present our spatial resolution is about 100μ but this can be reduced to about 50μ by means of improved optics. The penetration depth of the light in the region of the E_0 optical structure is ≈ 1000Å so that our technique can be used on thin epitaxial layers. It should be pointed out that in addition to relative changes in composition

we can also accurately determine the band gap of the material. This latter information is of interest in evaluating the value of the index of refraction which is relevant to confinement characteristics of lasers.

Our approach has several advantages over the microprobe technique. In effect, the microprobe, while it does yield a surface analysis with a resolution of 1μ, is not entirely satisfactory. This is due to the fact that a nominal composition obtained by a microprobe analysis is no guarantee that the Ga atoms, for example, all occupy their normal site in the lattice and therefore that one can reasonably deduce from the measured composition a value of the optical band gap. In contrast, our method determines an effective composition correlated to the optical band gap. Furthermore, the equipment needed to utilize the EER technique is a factor of 10 less expensive than microprobe apparatus and the scanned spot size is more consistent with array dimensions.

The EER technique has a number of advantages over luminescence techniques.[4] Although the latter methods can tell a great deal about the material considerable supporting information must be available in order to make use of luminescence data. As an example, a great deal of the luminescence of III-V compounds, particularly at temperatures below 300°K, involves donors, acceptors and bound excitors. Thus conclusions about the band structure can be reached only after these impurity effects are properly accounted for.[4] EER, on the other hand, gives direct information about the intrinsic band gap irrespective of the nature of the impurity content. Furthermore, it can be readily utilized at room temperature.

IV. ACKNOWLEDGEMENT

We wish to acknowledge the contribution of Prof. P.M. Raccah to this work.

References

1. M. Cardona, K.L. Shaklee and F.H. Pollak, Phys. Rev. 154, 696 (1967).

2. P.E. Vanier, F. H. Pollak and P.M. Raccah, presented at the "Topical Meeting on Optical Phenomena in Infrared Materials", Annapolis, Maryland, 1976.

3. O. Berolo and J.C. Wooley, Can. J. Phys. 49, 1335 (1971).

4. See, for example, A. Onton, M.R. Lorenz, J.M. Woodale and R.J. Chicotka, J. Crystal Growth 27, 166 (1974).

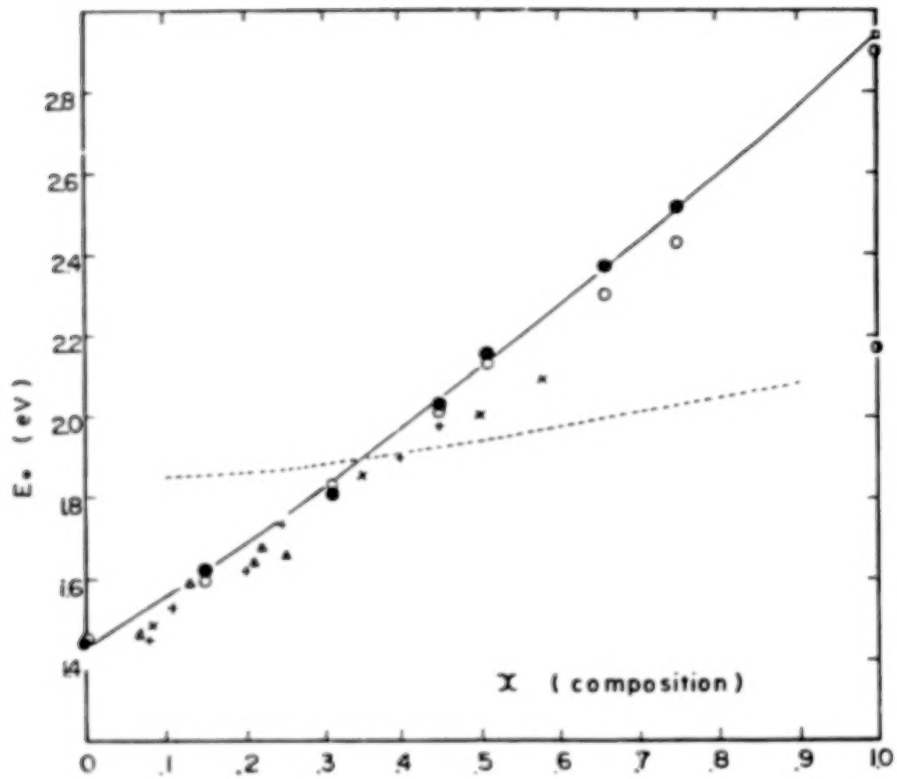

Figure 1. Variation of the E_0 (direct gap) electroreflectance peak with x for $Ga_{1-x}Al_xAs$ alloys. The solid circules represent the work of Ref. 1. The dashed line is the indirect gap.

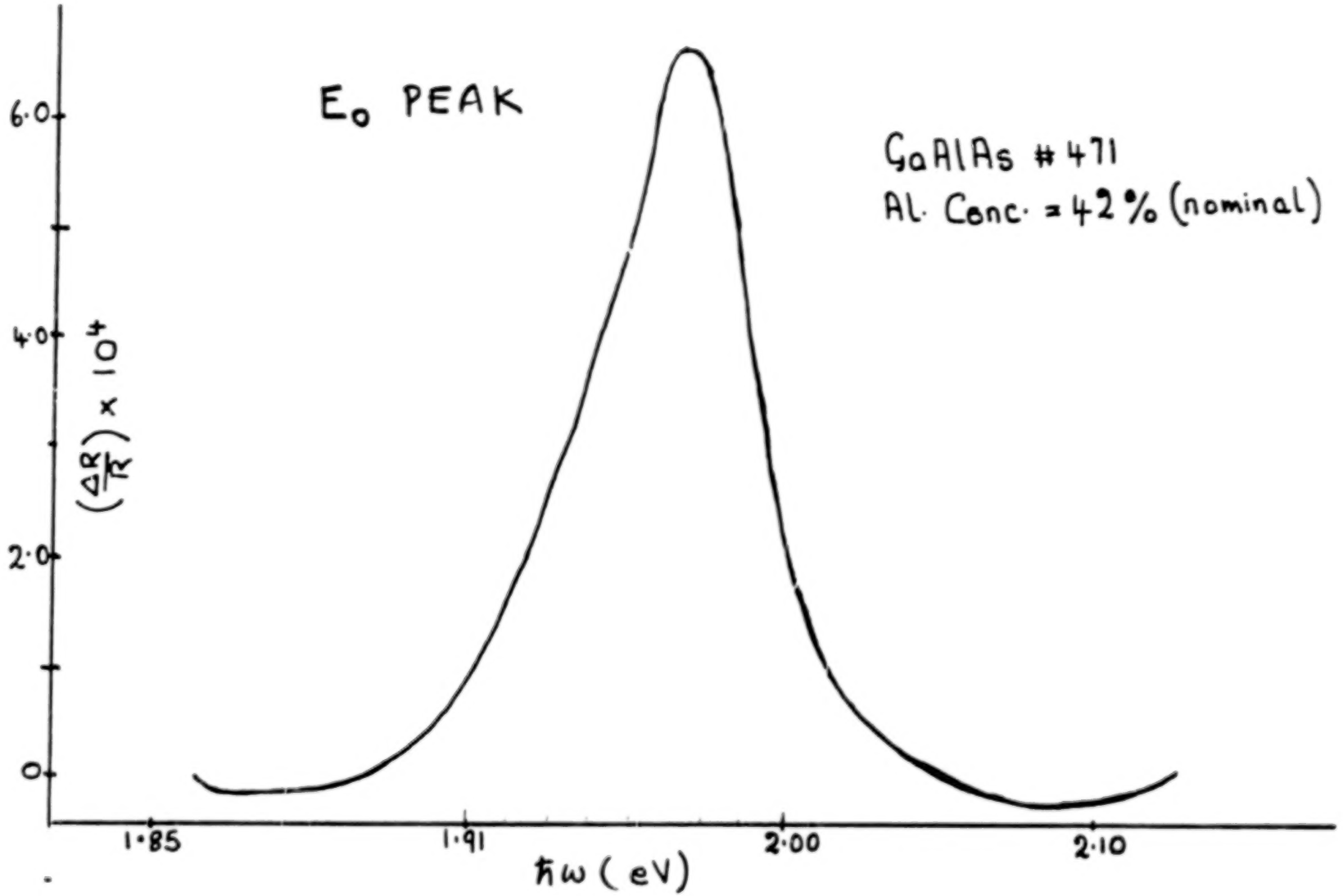

Figure 2. Electroreflectance spectrum ($\Delta R/R$) of the E_o peak (direct edge at $\vec{k} = 0$) of $Ga_{1-x}Al_xAs$ sample 471 ($x = 0.42$ nominal).

GaAlAs # 471 Al Con. = 42% (nominal)

CONTOUR INTERVAL: $\triangle x = 0.002$

$\triangle x = 0 \Rightarrow E = 1.9805eV$

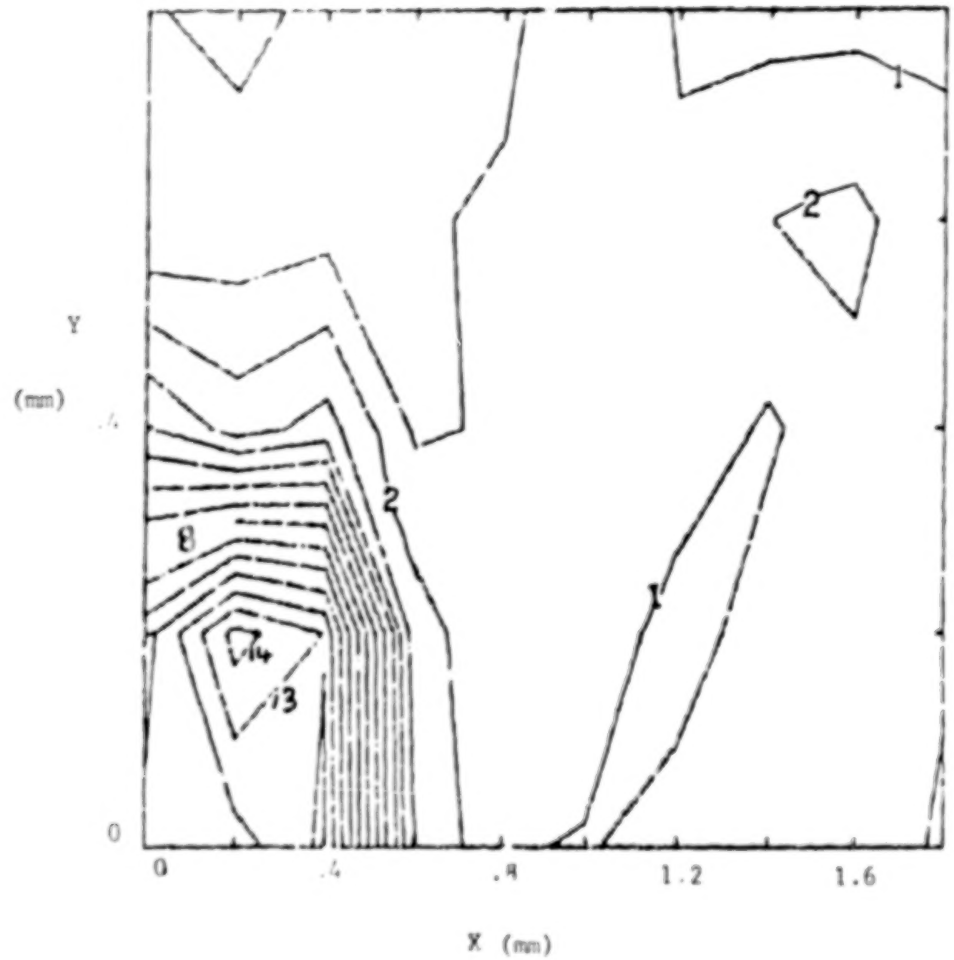

Figure 3a. Contour map of the variations in composition Δx of $Ga_{1-x}A\ell_xAs$ sample 471. The reported nominal value of x = 0.42. The contours are at intervals of Δx = 0.002 with the lowest measured value of the composition taken arbitrarily to be Δx = 0.00.

GaAlAs # 471 Al Con.= 42% (nominal)

CONTOUR INTERVAL: $\Delta x = 0.002$

$\Delta x = 0 \Rightarrow E = 1.9895$eV

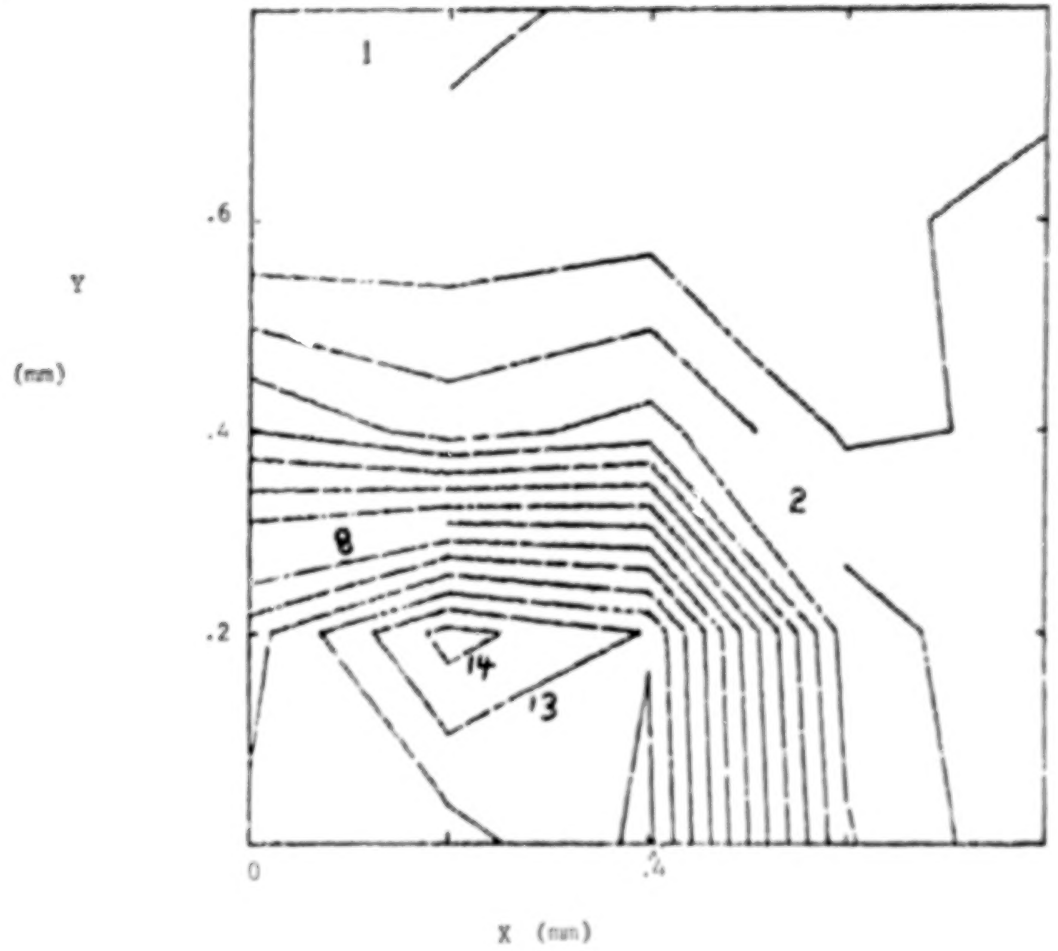

Figure 3b. Expanded section of lower left hand region of Figure 3a.

GaAlAs #472 Al Conc.=54% (nominal)

CONTOUR INTERVAL: $\triangle x = 0.002$

$\triangle x = 0 \Rightarrow E = 2.0957 eV$

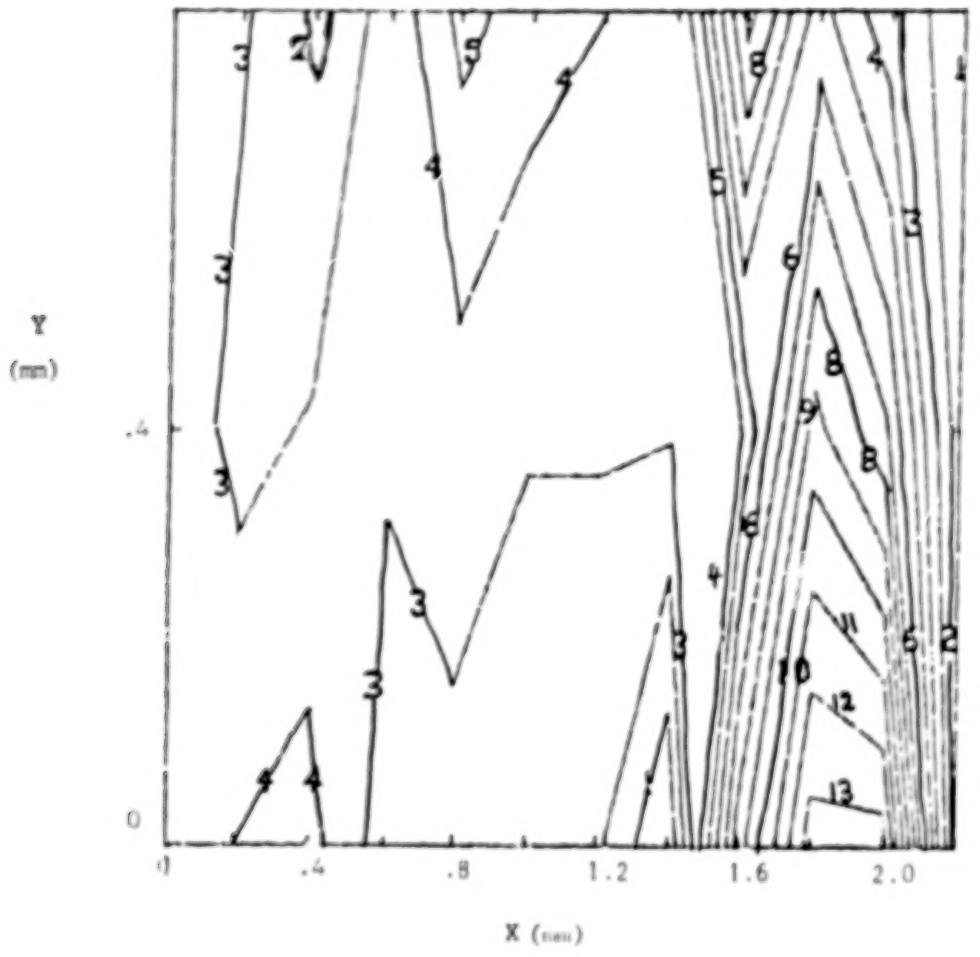

Figure 4a. Contour map of the variations in composition Δx of $Ga_{1-x}Al_xAs$ sample 472. The reported nominal value of $x = 0.54$. The contours are at intervals of $\Delta x = 0.002$ with the lowest measured value of the composition taken arbitrarily to be $\Delta x = 0.00$.

GaAlAs #472 Al Conc.=54%(nominal)

CONTOUR INTERVAL: $\triangle x = 0.002$

$\triangle x = 0 \Rightarrow E = 2.0957$eV

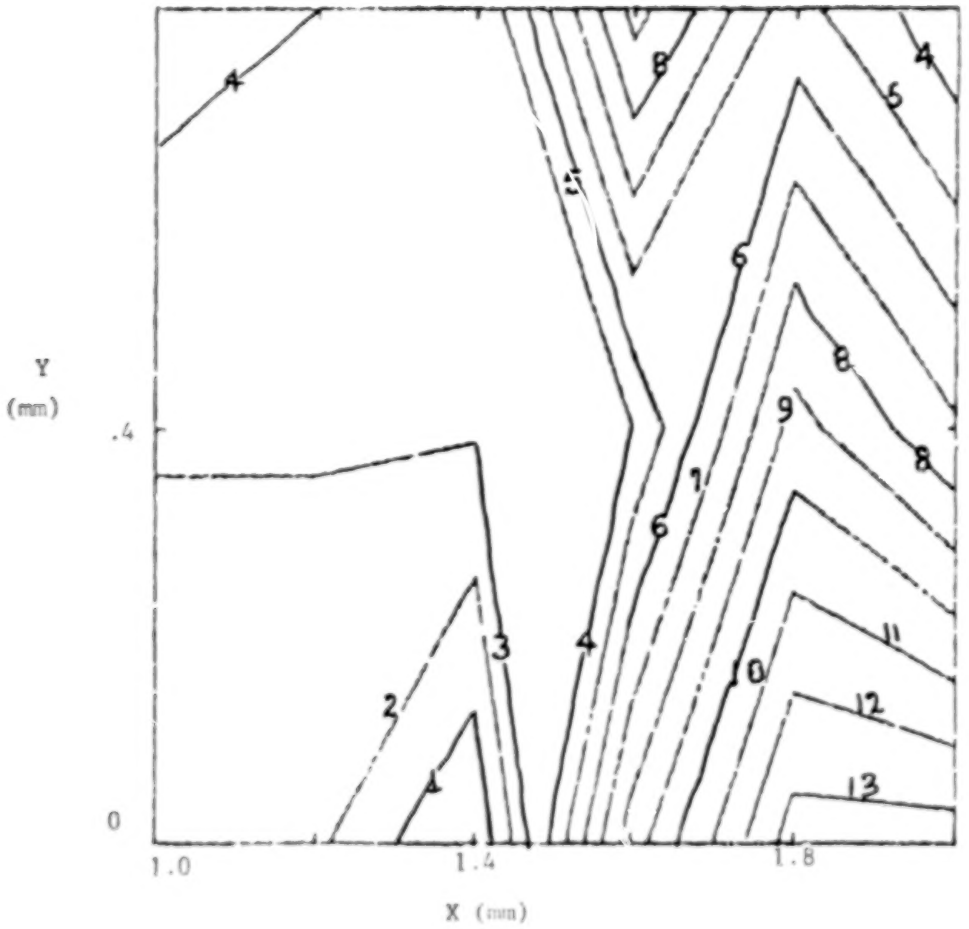

Figure 4b. Expanded view of lower right hand region of Figure 4a.

#473

GaAlAs/Al Con.=65%(nominal)

CONTOUR INTERVAL: $\triangle x$=0.003

$\triangle x$=0 ⇒ E= 2.3300eV

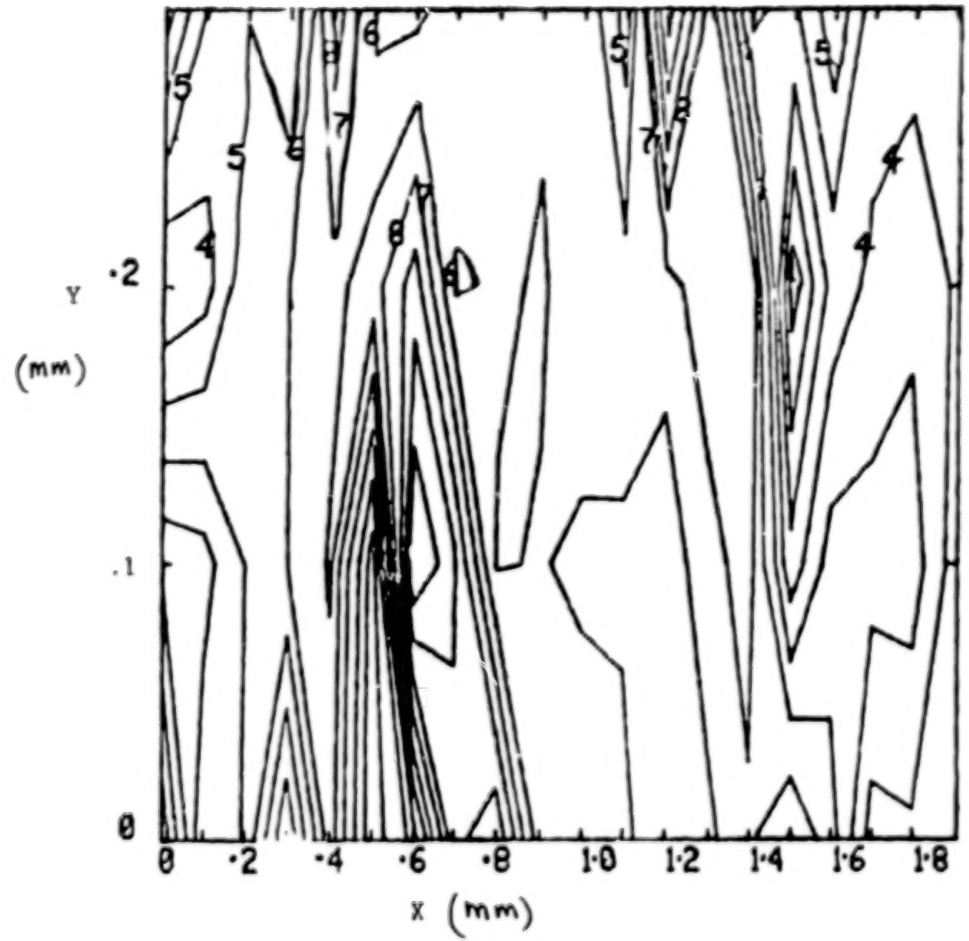

Figure 5a. Contour map of the variations in composition Δx of $Ga_{1-x}Al_xAs$ sample 473. The reported nominal value of x = 0.65. The contours are at intervals of Δx = 0.003 with the lowest measured value of the composition taken arbitrarily to be Δx = 0.00.

#473

GaAlAs/Al Con.=65%(nominal)

CONTOUR INTERVAL: $\triangle x=0.003$

$\triangle x=0 \Rightarrow E= 2.3300eV$

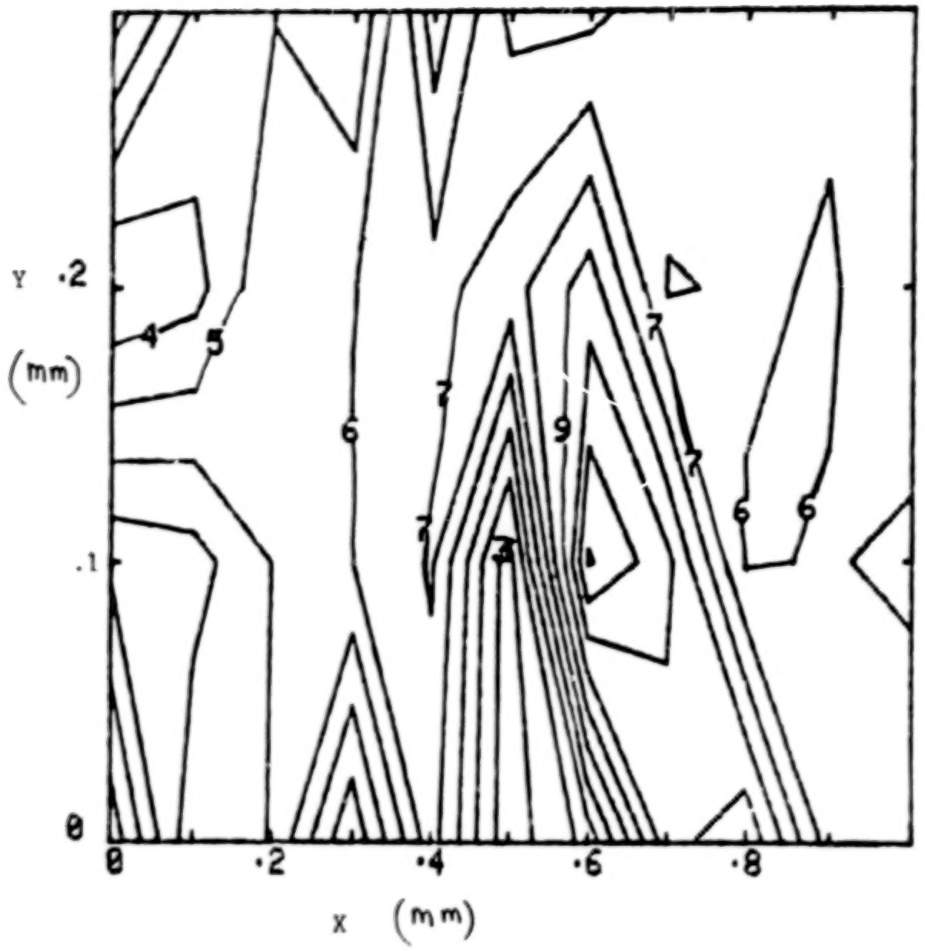

Figure 5b. Expanded view of lower left region of Figure 5a.

93

GaAlAs #475 Al Conc.=94% (nominal)

CONTOUR INTERVAL: $\Delta x = 0.002$

$\Delta x = 0 \Rightarrow E = 2.6651$ eV

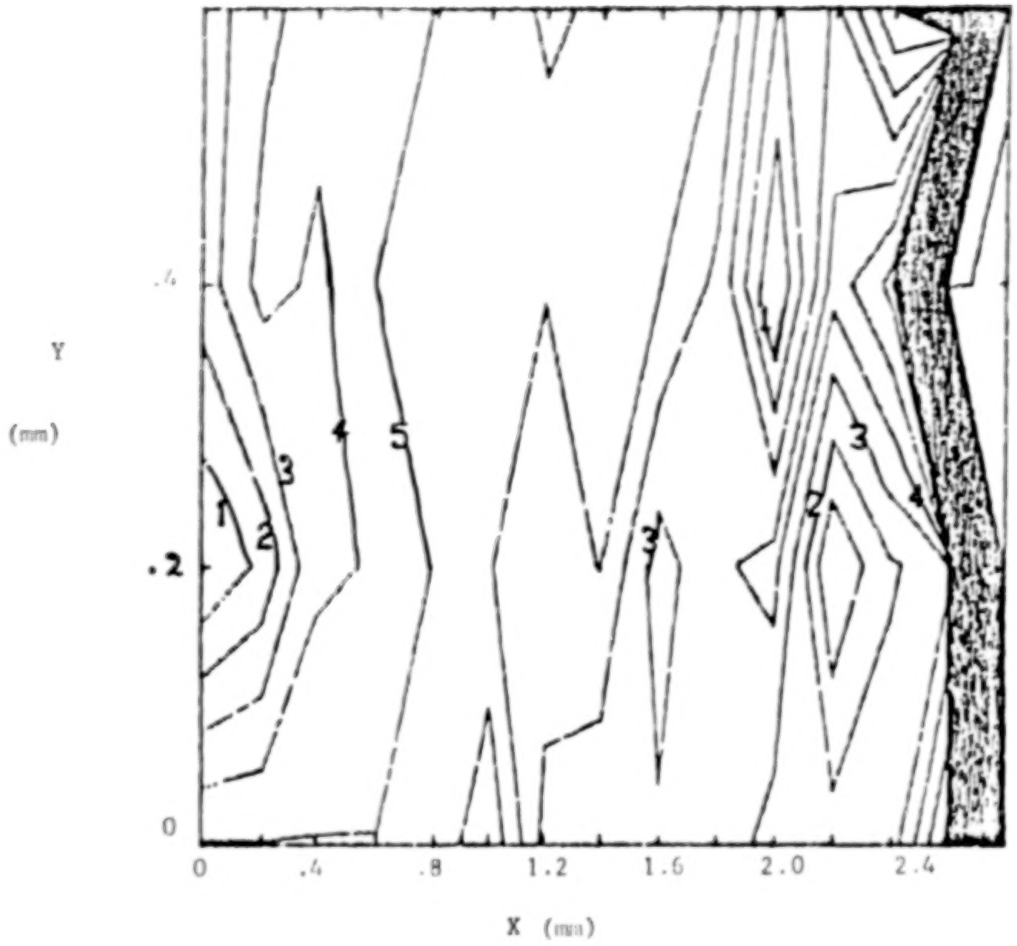

Figure 6. Contour map of the variations in composition Δx of $Ga_{1-x}A\ell_xAs$ sample 475. The reported nominal value of $x = 0.94$. The contours are at intervals of $\Delta x = 0.002$ with the lowest measured value of the composition taken arbitarily to be $\Delta x = 0.00$.

APPENDIX B

THE INFLUENCE OF STRIPE WIDTH ON THE THRESHOLD CURRENT OF DH LASERS*

I. Ladany

Reprinted from
JOURNAL OF APPLIED PHYSICS,
Vol. 48, No. 5, May 1977 (with permission)

*Copyrighted by the American Institute of Physics

Blank Page

The influence of stripe width on the threshold current of double-heterojunction lasers

I. Ladany

RCA Laboratories, Princeton, New Jersey 08540
(Received 3 December 1976; accepted for publication 14 January 1977)

Experimental measurements of the threshold current of oxide-isolated stripe lasers as a function of stripe width and *p*-layer resistivity are presented. A calculation of the influence of carrier outdiffusion has been made, including the effect of current leakage beyond the stripe edges. The calculated threshold increase is in substantial agreement with experiment for stripe widths down to about 10 μm. The data also yield an effective diffusion length of ~7 μm for the lasers studied. Deviations between experimental and calculated thresholds occurring at stripe widths of 4–6 μm are represented by an empirical curve which is compared with previously published calculations of threshold gain.

PACS numbers: 42.55.Px, 85.30.De, 85.60.Jb

It is well known[1] that the threshold current density of stripe lasers increases rapidly when the stripe width is made small enough. Although several theoretical treatments of this effect have been published, little experimental information is available in the literature. The data most often quoted are taken from the paper by Dyment, Ripper, and Zachos[2] who studied homojunction lasers made by diffusion of zinc into *n*-type substrates. Currently manufactured double-hetero junction (DH) lasers of the kind used to obtain cw operation do not seem to have received adequate attention.

In the present work, we study the threshold dependence of DH lasers as a function of stripe width and compare it with existing theory, which was modified as discussed below. The lasers we are dealing with use oxide rather than proton bombardment to define stripe contacts that control the current restriction. This leads to complications since current leakage beyond the stripe edge must be included in the analysis. On the other hand, earlier reported discrepancies between theory and experiment ascribed to uncertainties in the depth of proton bombardment[2] need not be considered in the present case.

In Sec. I we present experimental measurements of the threshold current for different stripe widths using several separately grown wafers for the laser material. In Sec. II we discuss the theoretical basis of the effect, and provide a calculation of the threshold current as a function of stripe width, taking into account current leakage and carrier diffusion, but neglecting optical absorption effects. Section III deals with a comparison between experiment and this calculation and with the magnitude of the neglected optical effects.

I. EXPERIMENTAL TECHNIQUE AND RESULTS

(AlGa)As laser material, emitting near 8200 Å, with an undoped recombination region 0.15–0.25 μm in width was used for the experiments. Heterojunctions were formed from material with aluminum fractions of 0.28–0.30. Metallized stripe contacts were defined by an insulating layer of SiO_2. After cleaving into strips, individual diodes were separated and mounted on headers. Occasionally diodes were not separated but were excited by probing, the metallization between them being first removed. It was found that these two methods gave essentially identical results when applied to a strip which was subsequently sawed apart and the diodes mounted on headers.

The sheet resistivity of the layers between the surface and the *p*–*n* junction was computed from the known doping of the layers and was also measured by determining the resistance between two stripes of known separation. In order to avoid contact resistance in these measurements, a four-terminal arrangement similar to that in Fig. 1 was used. The voltage V obtained between the two inner stripes when a current I is flowing between the outer ones is given by

$$V = I\frac{l}{H}\left(\frac{t_1}{\rho_1} + \frac{t_2}{\rho_2}\right)^{-1}, \tag{1}$$

where l is the distance between the stripes and H is the diode length normal to the plane of Fig. 1. The expression in the large parentheses in Eq. (1) is the combined sheet resistivity R_s and is therefore easily obtained from

$$R_s = \frac{V}{I}\frac{H}{l}. \tag{2}$$

Computed and measured sheet resistivity values were in substantial agreement. The sheet resistivity is the parameter which determines the current leakage and we expect it would have an effect on the threshold current, although not necessarily that given by Dumke.[3] The emission of each laser was monitored using a silicon detector and oscilloscope, and the threshold determined by ascertaining the current where the detected pulse increased superlinearly. Two kinds of data were assembled. In the first, the above-mentioned measurements were taken on diodes or strips from several wafers with different sheet resistivities. For a given wafer, thresholds were measured on several diodes for each width, and the averages recorded. The magnitude of the threshold current is shown in Fig. 2, plotted

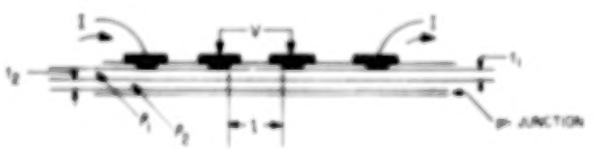

FIG. 1. Geometry of the sheet resistivity measurement.

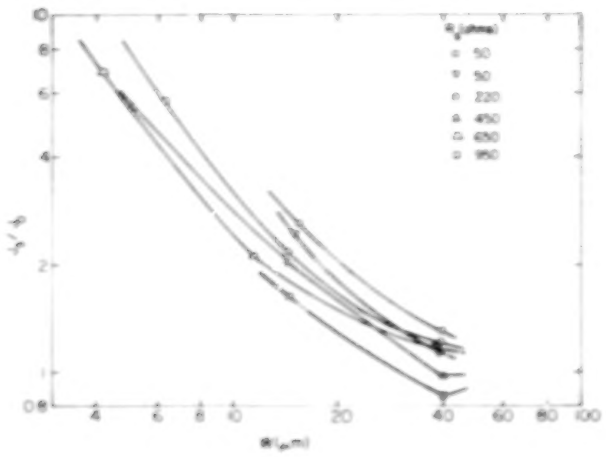

FIG. 2. Stripe threshold current density divided by the broad-area threshold current density as a function of stripe width. Each curve is taken from a different group of diodes having the indicated sheet resistivity.

as the ratio of the stripe threshold current density to the broad-area threshold current density. Stripe current density is defined as the ratio of the threshold current to the stripe area, and the broad-area current density is this ratio for a stripe ~100 μm wide.

With some exceptions, the curves have a similar appearance, with a vertical displacement according to the sheet resistivity associated with them. The importance of this parameter in determining the threshold current is thus clearly indicated. (See Ref. 3a.)

For a detailed comparison with theory a second set of data was obtained. With these, better control of the important device parameters was achieved by means of the following procedures. Measurements were taken on a single wafer to which four separate stripe widths were applied simultaneously. Strips containing some 20 diodes with cyclically repeated stripe widths were probed for threshold and sheet resistivity. Data were recorded serially so as not to lose the correlation between adjacent regions of the wafer. The separation between the stripes was ~330 μm, the expectation being that this would allow comparisons without significant changes in the underlying structure. A further selection was made by searching for unbroken groups of contiguous diodes containing several (at least two) diodes for each width having reasonably close threshold current values.

Data for three such groups of diodes are given in Table I. Discussion of these will be postponed in order to first develop a model which will be needed in the analysis.

II. THEORY

The stripe laser has been the subject of a number of analyses in recent years. Of most concern to the present work are a series of papers by Hakki,[3,4,5] where various properties are calculated, including the influence of stripe width on the threshold current. A detailed comparison of available experimental data was made with proton-bombarded lasers, and certain other results were also given for oxide-isolated stripes with current leakage. Because of the complexity of the analysis, these calculations are not readily compared with experiment. However, it was concluded that the main contribution to the threshold increase comes from carrier outdiffusion and that optical effects only become important at very narrow stripe widths. This suggests a different approach to the study of width dependence than given previously. It turns out that a simple expression can be derived which includes the effects of outdiffusion and current leakage on the carrier concentration within the stripe region. Thus the threshold increase due to outdiffusion can be presented in closed form and plotted as a series of curves which form the framework against which to study the experimental results. Over regions where these curves apply (for stripe widths to 10 μm or less), they may even provide an adequate prediction of the threshold current based on calculations only. Finally, by comparing these curves with experiment, the neglected optical effects can be estimated, and presented as an empirical correction to the calculations.

The approach used in these calculations follows that of Hakki. The main difference is in the way the effect of current leakage is introduced in the equations; it must be included simultaneously with outdiffusion, since it leads to both an increase in threshold due to incomplete current utilization and a decrease in threshold due to suppression of diffusion by the carriers generated by the leakage current. Calling the diffusion-dependent factor F, and representing the optical effects leading to an increase in threshold gain by Z, the ratio of the stripe current density to the broad-area current

TABLE I. Threshold currents for three groups of "adjacent" diodes, selected for uniformity.

	w (μm)	I_{th} (A)	V/I (Ω)	
Group I	96.3	0.95	250	
	38.5	0.52	280	
	11.7	0.3	333	
	4.18	0.53	294	H = 770 μm
	96.3	1.0	313	l = 330 μm
	38.5	0.52	435	$\bar{R}_0$ = 828 Ω
	11.7	0.25	500	
	4.18	0.48	434	
	96.3	1.05	333	
Group II	4.18	0.16	• • •	
	11.7	0.152	• • •	
	38.5	0.26	• • •	H = 322 μm
	96.3	0.6	• • •	l = 330 μm
	4.18	0.176	• • •	$\bar{R}_0$ = 650 Ω
	11.7	0.136	• • •	
	38.5	0.77	• • •	
	96.5	0.52	• • •	
Group III	3.35	0.165	600	
	98.8	0.5	580	
	38.5	0.22	620	
	11.73	0.13	640	H = 301.5 μm
	3.35	0.24	630	l = 320 μm
	98.8	0.56	660	$\bar{R}_0$ = 603 Ω
	38.5	0.36	760	
	11.73	0.16	• • •	
	3.35	0.18	• • •	

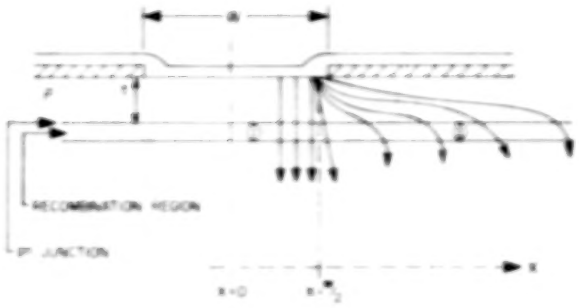

FIG. 3. Schematic diagram of the structure used in the analysis.

density can be written as

$$J_n = J_0 - YZ. \tag{3}$$

The remainder of this section will be devoted to the calculation of Y.

Referring to Fig. 3, carrier motion in region I in the x direction is determined by the diffusion equation

$$\frac{d^2n}{dx^2} - \frac{n}{L^2} + G = 0, \tag{4}$$

where

$$G = J_0/qDd \tag{5}$$

is the carrier concentration generated by the injected current density J_0, which is assumed uniform across region I. Here L is an "effective" diffusion length, D is the diffusion constant, and d is the width of the recombination region. The solution to Eq. (4) is

$$n(x) = [n(0) - L^2G]\cosh(x/L) + L^2G, \tag{6}$$

where $n(0)$, the carrier concentration at $x = 0$, remains to be determined. A similar equation applies in region II:

$$\frac{d^2n}{dx^2} - \frac{n}{L^2} + G' = 0. \tag{7}$$

The generation term G' in this case is determined by current leakage past the stripe edge. As shown by Dumke,[3] the total current flowing through a stripe laser subject to leakage is given by

$$I_{\text{stripe}} = I_0(1 + 2^{2/w}x_0/w), \tag{8}$$

where $x_0 = (mkT\ R_s J_0 q)^{1/2}$, R_s is the sheet resistivity of the top layer given by ρ/l, J_0 is the current density within and at the edge of the stripe, I_0 is the current flowing through a stripe laser if there is no leakage, w is the stripe width, and m is the parameter, taken to be ≈ 2, which appears in the exponent of the diode characteristic. In this equation, as well as in our subsequent development, we take the laser to have unit length along the long axis.

We can now write

$$G' = j(x)/qDd, \tag{9}$$

where $j(x)$ is the leakage current density in terms of current per unit length in the x direction. The diffusion constant D is taken to have the same value inside and outside the stripe. In setting up Eq. (9), we assume that the current which flows parallel to the junction in the layer above it changes direction and then flows downward into the recombination region. Such an assumption is necessary for a one-dimensional treatment, and is sketched in Fig. 3. The location of the p-n junction is also shown and is taken to coincide with the upper heteroboundary. Using further results of Ref. 3, we have

$$j(x) = -\frac{1}{R_s}\frac{dV}{dx} \quad \text{and} \quad \frac{Vq}{mkT} = \ln\frac{2}{(x - x_0 + \sqrt{2})^2},$$

which leads to

$$j(x) = \frac{2mkT}{R_s q(x + x_0\sqrt{2})}, \tag{10}$$

where $j(x)$ is the current flowing laterally beyond the stripe edge. Therefore,

$$j(x) = \frac{dI(x)}{dx} = -\frac{2mkT}{R_s q}\frac{1}{(x + x_0\sqrt{2})^2}. \tag{11}$$

Shifting the origin to the stripe center, and keeping in mind the current flow shown in Fig. 3, we substitute Eq. (11) into Eq. (9) to obtain

$$G' = \frac{2x_0^2 G}{(x_0\sqrt{2} - \frac{1}{2}w + x)^2}, \tag{12}$$

where it is to be noted that since $x > \frac{1}{2}w$, G' always remains finite. Letting

$$G' = \frac{A}{(B + x)^2}, \tag{13}$$

where $A = 2x_0^2G$ and $B = x_0\sqrt{2} - \frac{1}{2}w$, we can write the general solution of Eq. (7):

$$n(x)_{II} = c_1\exp\left(\frac{x}{L}\right) + c_2\exp\left(-\frac{x}{L}\right) + \frac{A}{2}\exp\left(\frac{x}{L}\right) \times \int\frac{\exp(-x/L)}{B + x}dx + \frac{A}{2}\exp\left(-\frac{x}{L}\right)\int\frac{\exp(x/L)}{B + x}dx. \tag{14}$$

The first derivative is

$$n'(x)_{II} = \frac{A}{B + x} + \frac{c_1}{L}\exp\left(\frac{x}{L}\right) - \frac{c_2}{L}\exp\left(-\frac{x}{L}\right) + \frac{A}{2L}\exp\left(\frac{x}{L}\right) \times \int\frac{\exp(-x/L)}{B + x}dx - \frac{A}{2L}\exp\left(-\frac{x}{L}\right)\int\frac{\exp(x/L)}{B + x}dx. \tag{15}$$

Equating carrier concentrations and diffusion currents at $x = \frac{1}{2}w$, using Eq. (6) and its derivative, and similarly Eqs. (14) and (15), we can solve for $n(0)$ to obtain

$$n(0) = L^2G\left[1 - \exp\left(-\frac{w}{2L}\right) + \frac{2c_1}{L^2G} + \frac{A}{LG(B + \frac{1}{2}w)} \times \exp\left(-\frac{w}{2L}\right) + \frac{A}{L^2G}\int\frac{\exp(-x/L)}{B + x}dx\right], \tag{16}$$

where x is to be replaced by $\frac{1}{2}w$ after the integration is carried out. The constant c_1 in Eq. (16) has to be so chosen that $n(x) \to 0$ as $x \to \infty$. Returning to Eq. (14), we recognize that the integrals therein are related to ex-

ponential integrals as follows:

$$\int \frac{\exp(x/L)}{B+x}\,dx = \exp\left(-\frac{B}{L}\right)\left[\ln\left(\frac{L}{B}\right) - \gamma - E_1\left(\frac{B+x}{L}\right)\right], \tag{17}$$

$$\int \frac{\exp(-x/L)}{B+x}\,dx = \exp\left(\frac{B}{L}\right)\left[\ln\left(\frac{L}{B}\right) - \gamma - E_1\left(\frac{B+x}{L}\right)\right], \tag{18}$$

where γ is Euler's constant. Putting the limiting values[6] of E_1 and E_2 into (14), we find that

$$c_1 = \frac{A}{2}\exp\left(\frac{B}{L}\right)\left[\gamma - \ln\left(\frac{L}{B}\right)\right] \tag{19}$$

gives the desired behavior as $x \to \infty$.

In order to calculate the current required to give the same carrier concentration at $x = 0$ in the case of a broad-area device and a stripe device, we set

$$n(0)_{\text{broad area}} = n(0)_{\text{stripe}}. \tag{20}$$

For the broad-area device we have $n(0) = L^2G = L^2J_0/qDd$ where J_0 is the current density obtained by dividing the applied current by the device area. For the stripe, on the other hand, we note that J_0 is not the applied current density, but the current density within the stripe region only. The applied stripe current I_s is the sum of two parts

$$I_s = I_0 + I_{\text{leakage}}, \tag{21}$$

where I_0 is the current flowing within the stripe region. Recalling Eq. (8), we have

$$I_0 = \frac{J_s}{(1 + 2^{\sqrt{2}x_0/w})} \tag{22}$$

and

$$G = \frac{J_s}{qDd(1 + 2^{\sqrt{2}x_0/w})} \tag{23}$$

for the stripe device. Here J_s is the current density obtained by dividing the total applied current by the actual stripe area. Making the indicated substitutions, after some algebraic manipulation, we obtain

$$\frac{J_s}{J_0} = \frac{1 + Q/w'}{1 + \exp(-w')[Q - Q^2\exp(Q)E_1(Q) - 1]}, \tag{24}$$

where

$$Q = x_0\sqrt{2}/L \quad \text{and} \quad w' = w/2L.$$

This equation exhibits the dependence of the threshold current on the combined effect of diffusion and leakage. Calling the term in the square brackets $F(Q)$, we show its magnitude as a function of Q in Fig. 4. Considerable simplification results for $Q \gg 1$ and $Q \ll 1$, where expansions for E_1 can be used. Thus

$$F(Q) \sim -2/Q \quad (Q \gg 3), \tag{25}$$

$$F(Q) \sim -1 \quad (Q \ll 1). \tag{26}$$

A convenient approximation to $F(Q)$, useful for all Q, is

$$F(Q) \approx (1 + 2/Q)^{-1} - 1. \tag{27}$$

Both forms of $F(Q)$ are plotted in Fig. 4. An interesting

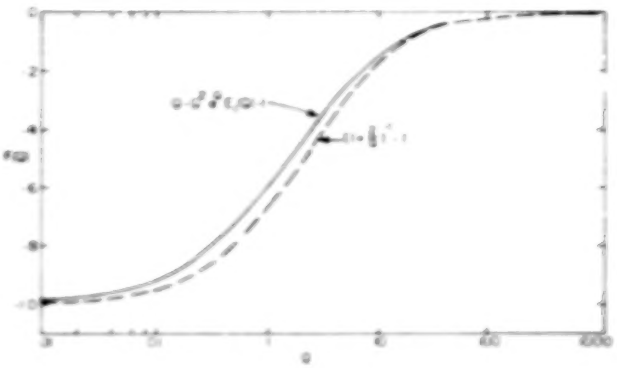

FIG. 4. The function $F(Q)$ derived in the text (solid curve) and an approximation to it (dashed curve).

question concerns the sensitivity of Eq. (24) to a different current spreading law. Equation (27) is precisely the form of $F(Q)$ obtained if the concentration outside the stripe decreases exponentially as

$$G' = G\exp[(\sqrt{2}\,x_0)(\frac{1}{2}w - x)] \tag{28}$$

instead of according to Eq. (12).

A plot of the threshold ratio J_s/J_0 with $x_0\sqrt{2}/L$ as parameter [Eq. (24)] is shown in Fig. 5. The lowest threshold ratios are obtained when $x_0\sqrt{2}/L = 0$, which implies infinite sheet resistivity. For this case, the present equation and that obtained by Hakki are identical.

III. DISCUSSION

A comparison between theory and experiment requires knowledge of L, the effective diffusion length[7] in the recombination region. As discussed recently by

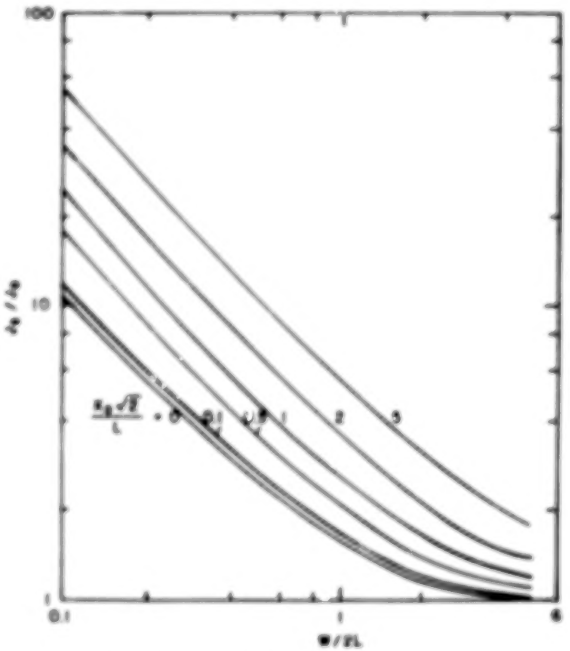

FIG. 5. Calculated threshold ratio for outdiffusion and leakage, but neglecting optical effects.

TABLE II. Data from Table I, recalculated for diffusion lengths obtained by curve fitting at large w.

Group I			Group II			Group III		
$w/2L$	w (μm)	J_s/J_0	$w/2L$	w (μm)	J_s/J_0	$w/2L$	w (μm)	J_s/J_0
0.26	4.18	11.6	0.35	4.18	6.9	0.24	3.35	11
0.73	11.7	2.26	0.98	11.7	2.1	0.84	11.7	2.3
2.4	38.5	1.3	3.2	38.5	1.2	2.75	38.5	1.4
6	96.3	≡1	8	96.3	≡1	7	98.8	≡1
$x_0 = 2.1 \times 10^{-4}$ cm			$x_0 = 2.06 \times 10^{-4}$ cm			$x_0 = 2.16 \times 10^{-4}$ cm		
$Q = 0.37$			$Q = 0.485$			$Q = 0.44$		
$L = 8$ μm			$L = 6$ μm			$L = 7$ μm		
$J_0 = 1348$ A/cm^2			$J_0 = 1805$ A/cm^2			$J_0 = 1780$ A/cm^2		

Ettenberg and Kressel,[8] this is a complex parameter, dependent on bulk properties and the heteroboundary interfacial recombination velocity. It has also been measured,[4] a typical value for DH structures being 6 μm. In the present analysis this parameter is not arbitrary, as it determines both the horizontal and vertical position of the experimental curves, when superimposed on a plot of the threshold ratios as given in Fig. 5. Assuming that Y can be neglected at larger $w/2L$, we look for the best fit by shifting the curves horizontally, and then calculate $x_0\sqrt{2}\,L$ to check the vertical alignment. It is easily established that the three groups of data require L to be 6, 7, and 8 μm in order to obtain reasonable agreement with the calculations at larger $w/2L$.

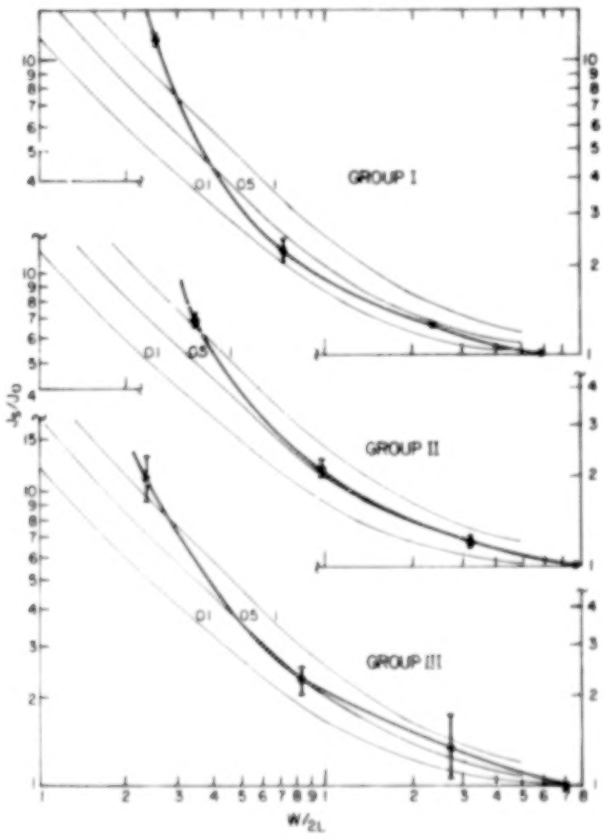

FIG. 6. Experimental threshold ratios fitted to the curves of Fig. 5.

Table II summarizes the relevant data for the three groups, shown plotted in Fig. 6. Error bars are obtained from the maximum and minimum threshold currents measured at each width. In all cases the fit to the calculated curves is within the error bars for $w/2L \gtrsim 0.6$. At smaller $w/2L$ all three curves show an increase beyond that given in the calculations. In line with a number of published studies[2,9] we associate this with absorption of the mode outside the pumped region. Calling the magnitude of this effect Z, as discussed earlier, we may consider its explicit form,[2]

$$Z = \frac{g_{th}(0) + b}{M + b},$$

where $M = (1/H)\ln(1/R)$, $b = 146$ cm^{-1}, and $g_{th}(0)$ is available from Hakki's paper. An empirical expression for Z can be obtained by forming the quotient of the measured and extrapolated threshold ratios for the data for Group II shown in Fig. 6. A comparison of the two versions is given in Fig. 7. The trend in the curves is similar and the magnitudes are of the same order, but the empirical curve begins at smaller w and rises much faster as w decreases. Some of the reasons for this can no doubt be found in differences between the geometries for the two cases, such as the spreading of the mode beyond w for oxide-isolated stripes. Other difficulties arise when the stripe becomes extremely narrow as inhomogeneities in materials lead to unevenness in current flow and pumping.

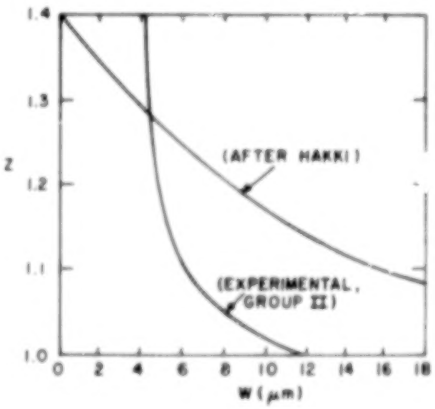

FIG. 7. The function Z representing neglected optical effects. Both the curve calculated by Hakki and an empirical curve are shown.

A prediction of the laser threshold current for narrow stripes can nevertheless be made if the sheet resistivity is known, by taking the appropriate curve from Eq. (24), using $L = 7\ \mu$m as an average value, and multiplying the threshold ratios obtained at a particular stripe width by the experimental Z function given in Fig. 7.

In conclusion, measurements are reported of the threshold current of DH oxide-isolated stripe lasers with different stripe openings. It is shown that the threshold current density increases as the opening is made smaller, and also as the sheet resistivity of the layers between the p-n junction and the opening decreases. Both of these effects are calculated theoretically, and a good agreement is found for stripe openings down to about 10 μm. Below these values, mode absorption beyond the region of population inversion becomes important in further increasing the threshold. The magnitude of this effect has been compared with published calculations, and although the trends are similar, there is disagreement in detail.

ACKNOWLEDGMENTS

Valuable work by V. M. Cannuli in LPE growth, D. P. Marinelli in stripe fabrication, and M. G. Harvey in diode processing is gratefully acknowledged. Dr. M. D. Miller and especially Dr. J. P. Wittke have been most helpful in reviewing the manuscript and offering suggestions for its improvement. The support of H. Kressel during the course of this work has been appreciated.

[a]Work partially supported by National Aeronautics and Space Administration, Langley Research Center, Hampton, Va.

[1]J. C. Dyment, J. E. Ripper, and T. H. Zachos, J. Appl. Phys. **40**, 1802 (1969).

[2]B. W. Hakki, J. Appl. Phys. **46**, 2723 (1975).

[3]W. P. Dumke, Solid-State Electron. **16**, 1279 (1973).

[4]*Note added in proof*. It should be pointed out that whereas the the wafers used in these experiments are in most respects similar to standard DH material, the sheet resistivity is not necessarily that commonly employed, and the contacts are applied without the usual zinc diffusion.

[4]B. W. Hakki, J. Appl. Phys. **44**, 5021 (1973).

[5]B. W. Hakki, J. Appl. Phys. **46**, 292 (1975).

[6]*Handbook of Mathematical Functions*, Natl. Bur. Stand. Appl. Math. Series 55 (U.S. Government Printing Office, Washington, D.C., 1964).

[7]L depends on the carrier concentration, but is assumed constant (see Ref. 4).

[8]M. Ettenberg and H. Kressel, J. Appl. Phys. **47**, 1538 (1976).

[9]F. R. Nash, J. Appl. Phys. **44**, 4696 (1973).

APPENDIX C

Al_2O_3 HALF-WAVE FILMS FOR LONG-LIFE CW LASERS*

I. Ladany, M. Ettenberg, H. F. Lockwood, and H. Kressel

Reprinted from Applied Physics Letters,
Vol. 30, No. 2, 15 January 1977 (with permission)

*Copyrighted by American Institute of Physics

Blank Page

Al_2O_3 half-wave films for long-life cw lasers

I. Ladany, M. Ettenberg, H. F. Lockwood, and H. Kressel

RCA Laboratories, Princeton, New Jersey 08540
(Received 1 September 1976; in final form 15 November 1976)

Long-term operating-life data are reported for (AlGa)As cw laser diodes. The use of half-wave Al_2O_3 facet coatings is shown to eliminate facet erosion, allowing stable diode operation at constant current for periods in excess of 10000 h.

PACS numbers: 42.55.Px, 42.60.Da

It has been shown previously that the operating life of cw (AlGa)As laser diodes can be reduced by facet damage.[1,2] Two possibly related phenomena have been identified. The first is a rapid failure mode, occurring at very high emission levels, termed "catastrophic facet damage"[1] (which has also been studied extensively in the case of pulsed lasers). The second, denoted "facet erosion", has become prominent with the development of cw lasers,[2] and occurs at modest power levels after many hours of operation. Earlier work has indicated that the use of dielectric facet coatings might be useful in minimizing the possibility of cw laser facet erosion.[1] In this paper, we report on devices with Al_2O_3 half-wave facet coatings having stable output at *constant current* operation for times beyond 10000 h.

The main reason for employing half-wave rather than quarter-wave coatings is the need to maintain the normal facet reflectivity and thus keep the threshold current as low as possible. Although this requirement excludes the beneficial effects of antireflection films,[3] we find that significant improvements in diode life and stability are obtainable from half-wave coatings.

The lasers studied were similar to those used in our previous work and consist of $Al_{0.3}Ga_{0.7}As$ $Al_{0.08}Ga_{0.92}As$ double-heterojunction structures with recombination region widths of ~ 0.2 μm. Stripe contacts were made using oxide isolation with a stripe width of about 13 μm and a length typically 300–400 μm. Diodes were mounted on copper headers using In and were operated in a normal laboratory ambient at a fixed heat-sink temperature of 22 °C. Life data for uncoated units were obtained in a dry atmosphere. Aluminum oxide films were deposited in an oil diffusion pumped electron-beam evaporator.

The effect of thickness on reflectivity was measured by evaporating the film on one side of a laser diode and measuring the output power ratio from the two sides at a power level of a few milliwatts above threshold. The expression

$$\frac{P_1}{P_2} = \left(\frac{R_2}{R_1}\right)^{1/2} \left(\frac{1-R_1}{1-R_2}\right) \tag{1}$$

allows the reflectivity, R_1, of the coated facet to be calculated.[3-6] Here P is the output power, the subscripts 1 and 2 refer to the coated and the uncoated side, respectively, and we take $R_2 = 0.32$. In Fig. 1 we plot R_1 as a function of the layer thickness to wavelength ratio, using film thickness data obtained from profilometer measurements (Tallysurf-4) of larger samples coated simultaneously with the diodes. The solid curve shows the expected behavior for $n_{Al_2O_3} = 1.72$ and $n_{GaAs} = 3.6$. It can be seen that the fit is quite satisfactory for the thinner layers although a better fit for the thicker layers is obtained by assuming larger values for $n_{Al_2O_3}$.[5] It is to be noted that power ratios of 1.1–1.2 cannot be distinguished from a ratio of 1.0 since such a range of values is frequently observed on uncoated units. However, properly coated units have the same threshold current both with and without coatings, as ascertained by etching off the film and remeasuring the threshold current.

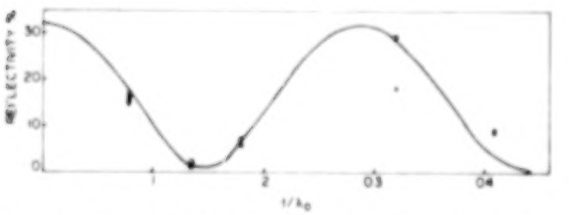

FIG. 1. Reflectivity as a function of t/λ_0 where t is the film thickness and λ_0 is the wavelength in air. The solid curve shows the calculated reflectivity assuming $n = 1.72$ for Al_2O_3 and $n = 3.6$ for GaAs.

The diodes used for life tests were selected from different but similarly grown wafers, and no obvious distinction could be made between them prior to the test. The operating conditions were set by the diode current (limited to 400 mA) and the corresponding power emitted was 5–15 mW from one facet.

The beneficial effects of the facet coatings are evident from Fig. 2 which shows the appearance of the diode facet following 600 h of operation with the emission of 10 mW of power. Parts of the facet were coated with Al_2O_3 while other regions were inadvertently left uncoated. Note that the uncoated regions are definitely damaged. Observable damage similar to that in Fig. 2 was observed on the facets of uncoated diodes operated for various periods of time, usually in excess of 1000 h. However, the time when this appears is extremely variable. In no case did the diodes with coated facets show evidence of this damage. Life tests of representative coated units are shown in Fig. 3. Also shown is the data on an *uncoated* unit operating in an airtight moisture-proof cabinet containing trays of indicating Drierite. Although the moisture content of the ambient is thereby controlled, it is not zero, as shown by the gradual change of Drierite color, necessitating replacement every four to six months. Diodes operating in this environment still show some evidence of facet erosion. While the output of this diode decreased in an irregular

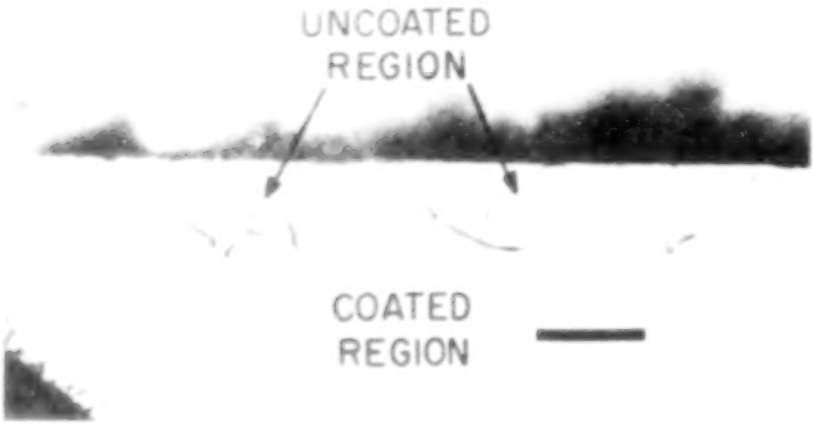

FIG. 2. Photomicrograph of facet of a partially coated diode after 600 h of operation showing regions of facet erosion in the uncoated areas. The length of the bar is 6 μm.

manner, it nevertheless continues to lase (actually having accumulated 18 000 h so far). The coated units show no or slight decrease in output for times in excess of 10 000 h, a result which appears to be quite general as confirmed by many other life tests currently in progress. The diode whose test is shown to terminate at 7000 h actually failed abruptly at that time with no evidence of facet damage. This behavior has not been seen by us in any of our previous studies, and appears due to an internal degradation process.

The mechanism responsible for the improvement in coated cw laser life reported here is believed different from that operating in high-power pulsed lasers where it was established[1] that catastrophic facet damage can be reduced by means of facet coatings of such thickness that the reflectivity is less than that of the uncoated facet. In the case of gradual facet erosion, the damage is eliminated by protecting the crystal surface with films which would have little or no effect on the catastrophic damage threshold. Although the facet erosion mechanism is not yet well defined, it is most likely caused by high optical flux acting on a free surface, with the ambient playing an accelerating role in this process.

In summary, we have shown that Al_2O_3 films can be deposited on laser facets with the thickness influencing the reflectivity in the expected manner. We have also shown that half-wave films which have no effect on threshold current serve to increase cw laser reliability since uncoated lasers have their life expectancy determined by ambient conditions. The half-wave films are thought to reduce the likelihood of facet erosion by impeding photochemical interactions between the diode material and the ambient, which occur under conditions of high optical flux.

The assistance of V. Cannuli, D. Marinelli, D. Gilbert, H.V. Kowger, M. Harvey, and G.R. Auth in various aspects of this work is gratefully acknowledged.

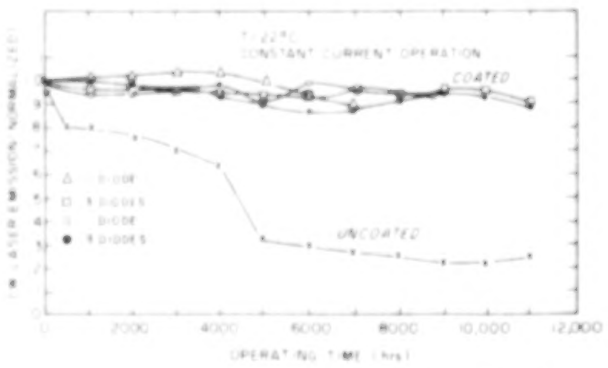

FIG. 3. Lifetests of coated diodes for constant current operation. Performance of an uncoated diode, maintained in a protected dry ambient, is also shown.

*Work supported partly by National Aeronautics and Space Administration, Langley Research Center, Hampton, Va.

[1] H. Kressel and I. Ladany, RCA Rev. **36**, 230 (1975).
[2] I. Ladany and H. Kressel, Appl. Phys. Lett. **25**, 708 (1974).
[3] M. Ettenberg, H.S. Sommers, Jr., H. Kressel, and H.F. Lockwood, Appl. Phys. Lett. **18**, 571 (1971).
[4] The use of this equation implies that mode reflectivity is being measured, whereas Fig. 1 is based on the more usual Fresnel reflectivity. Substitution of one for the other leads to only small error in the present case [J.K. Butler (private communication)].
[5] Different values have been published for the refractive indices: $n_{Al_2O_3}$ 1.66 at 8900 Å in the work of B.W. Hakki and C.J. Hwang [J. Appl. Phys. **45**, 2168 (1974)] and n_{GaAlAs} 1.62 in the work of H.C. Casey, Jr., D.D. Sell, and M.B. Panish [Appl. Phys. Lett. **24**, 63 (1974)]. The accuracy of our method is not sufficient to make use of the more accurate index of GaAs, or to suggest that our index for Al_2O_3 applies to material deposited elsewhere.

APPENDIX D

ACCELERATED STEP-TEMPERATURE AGING OF $Al_xGa_{1-x}As$ HETEROJUNCTION LASER DIODES*

H. Kressel, M. Ettenberg and I. Ladany

Reprinted from Appl. Phys. Lett. 32, 305 (1978)
with permission

*Copyrighted by American Institute of Physics

Blank Page

Accelerated step-temperature aging of $Al_xGa_{1-x}As$ heterojunction laser diodes[a)]

H. Kressel, M. Ettenberg, and I. Ladany

RCA Laboratories, Princeton, New Jersey 08540
(Received 26 September 1977; accepted for publication 29 December 1977)

Double-heterojunction $Al_{0.1}Ga_{0.9}As/Al_{0.36}Ga_{0.64}As$ lasers (oxide-striped and Al_2O_3 facet coated) were subjected to step-temperature aging from 60 to 100°C. The change in threshold current and spontaneous output was monitored at 22 °C. The average time required for a 20% pulsed threshold current increase ranges from about 500 h when operating at 100 °C to about 5000 h at a 70 °C ambient. At 22 °C, the extrapolated time is about 10^6 h. The time needed for a 50% spontaneous emission reduction is of the same order of magnitude. The resulting "activation energies" are ~0.95 eV for laser degradation and ~1.1 eV for the spontaneous output decrease.

PACS numbers: 42.55.Px, 85.60.Jb, 78.60.Fi, 42.80.Sa

The degradation of cw laser diodes may result from mirror (facet) damage, the internal formation of nonradiative centers due to lattice defects,[1] or an increase in the electrical or thermal resistance. Facet damage, which is related to the optical flux density, is controlled by the use of Al_2O_3 facet coatings[2] and by operating lasers at moderate power emission levels. The internal damage mechanism (gradual degradation)[3] is caused by electron-hole recombination. It is generally accepted that the energy released in nonradiative electron-hole recombination enhances point-defect displacement leading to the accumulation of defects in the recombination region.[3–5] The rate of this displacement process is expected to increase with temperature. Since gradual

[a)]Research partially supported by the National Aeronautics and Space Administration, Langley Research Center, Hampton, Va.

degradation is a process which depends on the electron-hole recombination rate, it occurs similarly in both the lasing and the incoherent emission state of diodes[1,3-5] at comparable current densities.

The present experiments were designed to study the threshold current (and spontaneous emission) change with operating time and temperature, as limited by the gradual degradation process. The reference temperature for these parameters is 22 °C, in order to provide a degradation "acceleration factor" useful in laser technology.

The lasers studied were oxide-defined stripe-contact double-heterojunction $Al_{0.3}Ga_{0.7}As$/$Al_{0.06}Ga_{0.92}As$ devices, emitting at 8200–8300 Å at room temperature. This is a widely used type of structure of earlier experiments.[2] The stripe width was 13 μm, the Fabry-Perot cavity length was 300–400 μm, and the facets were coated with a half-wave-thick evaporated film of Al_2O_3.[2]

The present experiments differ in several respects from earlier accelerated aging studies of lasers.[1-5] (1) The present devices are facet coated to eliminate possible surface-related effects on the threshold current. (2) The experiments are designed to test only the gradual degradation phenomena and not other device changes which could influence the threshold current. (3) The stripe technology is different (oxide stripe versus proton-bombarded stripe), a factor which can influence the aging behavior owing to the sensitivity of the devices to the fabrication technique. (4) The present temperature-dependent aging behavior was studied using devices with (AlGa)As in the recombination region rather than GaAs.[5] Because of the probable degradation-rate dependence on alloy composition, it is important to obtain aging parameters on currently important lasers. (Lasers with GaAs in the recombination region are rarely used for optical communications.)

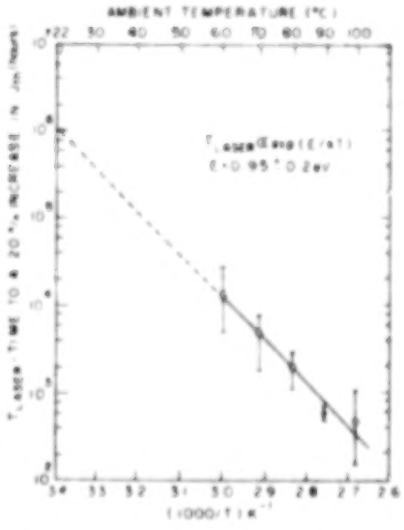

FIG. 1. Time, at various ambient temperatures, needed to reach a 20% pulsed threshold current increase. The circles are the average values determined from the devices operated at a given temperature, whereas the bar give the range of values. The solid line is a linear "best fit" to the average values, the dotted line is an extrapolation to lower temperatures.

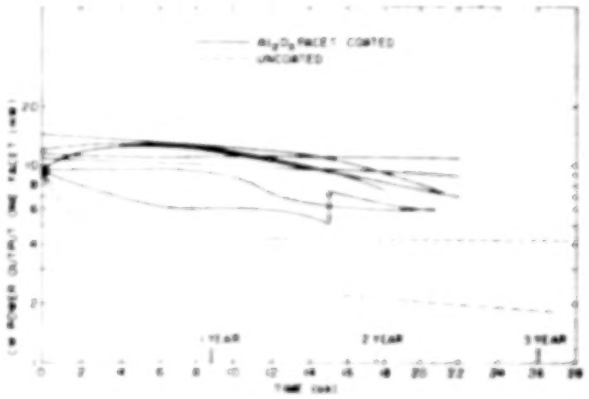

FIG. 2. Power output from one facet of laser diodes operating cw in a laboratory ambient at room temperature at constant current (with one exception discussed in the text where the arrows indicated a 9% increase). Data are shown for Al_2O_3 facet-coated and uncoated lasers.

The following experimental procedure was used. Fifteen lasers were selected from five similarly grown and processed wafers. The "typical" lasers selected had pulsed threshold current densities within about 20% of each other. They were free from obvious anomalies such as low-frequency oscillations and unusual kinks in the cw power-vs-current curve. It was the intent of the experiment to produce device data relevent to room-temperature operation; therefore, after the lasers were operated at various elevated temperatures (60, 70, 80, 90, or 100 °C) the *pulsed* (0.1% duty cycle) threshold current was remeasured at 22 °C to establish the amount of degradation induced by high-temperature operation.

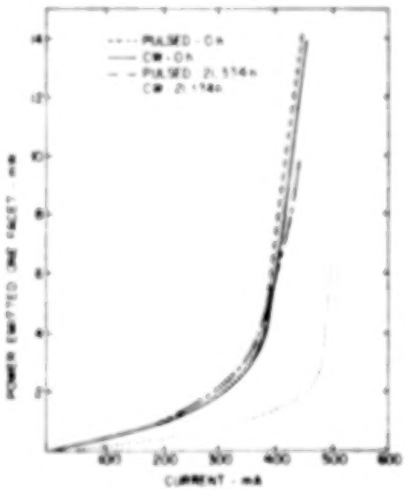

FIG. 3. Power output as a function of pulsed (0.1% duty cycle) and direct current of a laser operating 21 334 h at room temperature with a very high current level of 450 mA. Whereas the pulsed and dc thresholds were very nearly the same initially, a substantial difference is seen after long-term operation because of the diode's thermal resistance increase. As a result, the power emitted in constant-current operation is reduced, although no internal diode degradation has occurred as evidenced by the unchanged pulsed current threshold before and after the life test.

The pulsed (rather than the cw) threshold current was monitored at room temperature because it is directly related to the internal (gradual) degradation process (when facet damage is absent), whereas the cw threshold current is also a function of the thermal and electrical device resistance. Most lasers were operated at several temperatures, but always at the same direct current level of 200 mA, the typical cw operating current of these lasers at room temperature. Only three of the devices lased at 60 °C at 200 mA, and none lased at this current at higher temperatures. (No obvious degradation differences were traced to those devices which lased at 60 °C.) The operating time decreased with increasing temperature, ranging from 5000–6000 h at 60 °C to 150–300 h at 100 °C because the intent was to generally operate the lasers until a substantial threshold increase was observed.

Figure 1 shows $\tau_{1.5dB}$, the time needed for a 20% threshold current increase at various temperatures. The choice of this "figure of merit" is partly arbitrary because such a threshold increase need not terminate the life of a cw laser when the current is adjusted to keep the power output constant. However, because such an increase does represent a very significant level of laser deterioration it is a useful reliability benchmark value. In cases where the measured threshold change was under 20% at a given temperature, $\tau_{1.5dB}$ was obtained by linearly extrapolating to the estimated time for a 20% increase. This extrapolation no doubt adds to the data scatter. The vertical bars in Fig. 1 include our range of $\tau_{1.5dB}$ values, and the circles are the average values for all devices tested at a given temperature. The solid line is the best linear fit to the average values. It falls along a curve $\tau_{1.5dB} \propto \exp(E/kT)$, with $E = 0.95 \pm 0.2$ eV. The dotted line, an extrapolation to temperatures lower than those used in the test, projects to an average time of about 10^6 h to reach a 20% increase in the pulsed laser threshold at 22 °C. In practice, the cw threshold increase with time may be larger than the pulsed value if the thermal resistance of the laser increases (see below).

The credibility of extrapolated lifetime values eventually rests on measured data at the operating temperature of interest. In this regard, other measurements in our laboratory of lasers operating cw at 70 °C support the lifetime values in Fig. 1. Room-temperature (22 °C) cw lasing tests for similar facet-coated lasers have been running for periods in excess of 2×10^4 h in the laboratory ambient. The light output as a function of time *at constant current* is shown in Fig. 2. With the exception of one device which failed abruptly at 7000 h (not shown) and the laser discussed further below where the current was increased by 9%, as indicated by arrows, all of the facet-coated diodes that were placed on test at room temperature have passed 22 000 h of operation with less than a 3-dB drop in output at constant current. We analyzed the laser which showed the largest cw power output change to determine whether the reduction was due to gradual degradation (of the type studied in the experiments which we describe above) or to other factors. Careful microscopic inspection of the facet showed no mirror damage. This leaves a change in the thermal or electrical resistance of the

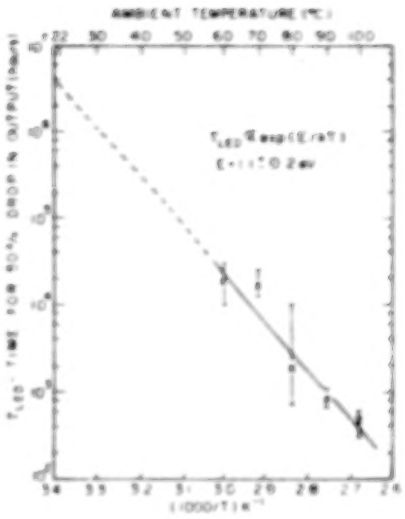

FIG. 4. Times at various ambient temperatures, needed to reach a 50% reduction in spontaneous output from the devices. The X's are the average values, and the bars give the range of values. The solid line is a linear "best fit" to the average values; the dotted line is an extrapolation to lower operating temperatures.

device. The latter effect was found to be responsible, as we now describe.

This laser emitting the highest cw output of the group (14 mW) is also the one operated at the highest current of 450 mA. It was measured before and after 21 334 h; the pulsed and cw operating curves are shown in Fig. 3. The important conclusion from Fig. 3 is that the laser's *pulsed* threshold current has not changed (indicating *no gradual degration*), although the cw threshold increased by 100 mA over the initial cw threshold (which was very close to the pulsed value). This increase is solely due to a substantial increase in the thermal resistance of the diode. This increase in thermal resistance is due to a deterioration of the In solder contact between the diode and the package caused by the excessive current density flowing through the 13-μm-wide contact strip. From this experiment (and others which we conducted) we believe that the high current density flowing through the In/contact metal interface produced changes in the contact which increased the thermal resistance. Therefore, the use of lasers with the lowest possible threshold current density is highly desirable to minimize this "contact degradation". These early stripe devices, due to significant current spreading, had threshold currents substantially higher than those of devices presently made with the same basic technology. It is thus anticipated that currently produced devices operating at much lower current densities, as measured through the contact (factor of 2) will not suffer the "contact degradation" found in the laser shown.

Figure 2 also shows two *uncoated* laser diodes operating in a dry air ambient at fixed current past 26 000 h, but with a degraded power level. These diodes exhibit marked facet erosion,[9] which causes a threshold current increase and differential quantum efficiency decrease. Thus, the reduction in output is not believed to be substantially related to gradual degradation. The

rapid drop in output in the early stages of operation of such uncoated lasers is characteristic of facet erosion.

Concurrently, the reduction of the diode spontaneous emission of all the devices was also measured. The lifetime definition adopted for the LED operation was the time τ_{LED} needed for a 50% reduction in the output at constant current. The data in Fig. 4 show the range of values observed as well as the average value measured at a given temperature. The best fit to the average τ_{LED} values is a linear line with an "activation energy" of 1.1 ± 0.2 eV which extrapolates to 4×10^5 h at 22 °C. Although real time confirmation of these predictions are far off, a group of similar LED's operating in our laboratory have reached 3×10^4 h without reduction in their output.

In conclusion, we have reported the results of step-temperature aging experiments of (AlGa)As double-heterojunction oxide-stripe lasers designed to test their sensitivity to gradual degradation. Extrapolating the high-temperature operation data to 22 °C, the estimated average time for a 20% pulsed threshold current is about 10^5 h, whereas at 70 °C ambient the same degradation occurs in about 5×10^3 h. (With regard to spontaneous diode emission, a 50% reduction in the power emitted is similarly estimated to require substantially more than 10^4 h at 22 °C.) The cw laser threshold can degrade faster than the pulsed threshold current if the thermal resistance of the laser increases. Such changes can occur if the current density through the stripe contact is excessive.

The authors are indebted to D. R. Gilbert, M. Harvey, A. Kan, H. V. Kowger, and D. Marinelli for technical assistance.

[1]For a review H. Kressel and H. F. Lockwood, J. Phys. Suppl. C3 **35**, 223 (1974).
[2]I. Ladany, M. Ettenberg, H. F. Lockwood, and H. Kressel, Appl. Phys. Lett. **30**, 87 (1977); H. Kressel and I. Ladany, RCA Rev. **38**, 230 (1975).
[3]H. Kressel and N. E. Byer, Proc. IEEE **57**, 25 (1969).
[4]D. H. Newman, S. Ritchie, and S. O'Hara, IEEE J. Quantum Electron. **QE-8**, 379 (1972).
[5]Y. Nannichi and I. Hayashi, J. Cryst. Growth **27**, 126 (1974).
[6]M. Ettenberg, H. Kressel, and H. F. Lockwood, Appl. Phys. Lett. **25**, 82 (1974).
[7]R. L. Hartman and R. W. Dixon, Appl. Phys. Lett. **26**, 239 (1975).
[8]R. W. Dixon and R. L. Hartman, J. Appl. Phys. **48**, 3225 (1977).

1 Report No.	2 Government Accession No.	3 Recipient's Catalog No.
NASA CR-3045		

4 Title and Subtitle	5 Report Date
1.1 MICROMETER AND VISIBLE EMISSION SEMICONDUCTOR DIODE LASERS	October 1978
	6 Performing Organization Code
7 Author(s)	8 Performing Organization Report No.
I. Ladany, C. J. Nuese and H. Kressel	PRRL-77-CR-52
	10 Work Unit No.
9 Performing Organization Name and Address	11 Contract or Grant No.
RCA Laboratories Princeton, New Jersey 08540	NAS1-14349
	13 Type of Report and Period Covered
12 Sponsoring Agency Name and Address	Contractor Report (3-16-76 to 2-25-77)
National Aeronautics and Space Administration Washington, D.C. 20546	14 Sponsoring Agency Code

15 Supplementary Notes

Langley Technical Monitor: Herbert D. Hendricks

Final Report

16 Abstract

In (AlGa)As, the first of three alloy systems studied, CW operation has been obtained at room temperature at a wavelength as low as 7260 Å. Reliability in this system was studied in the incoherent mode. Zinc doped devices had significant degradation, whereas Ge or Ge plus Zi doped devices had none. Al_2O_3 facet coatings were shown to significantly reduce facet deterioration in all types of lasers, longer wavelength units of that type having accumulated (at the time of writing) 22,000 hours with little if any degradation. A CL study of thin (AlGa)As layers has revealed micro fluctuation in composition. A macro-scale fluctuation has been observed by electroreflectance. An experimental and theoretical study of the effect of stripe width on the threshold current was carried out. Emission below 7000 Å was obtained in VPE grown Ga(AsP) (In,Ga)P with CW operation at 10°C. Lasers and LED's were made by LPE in (InGa)(AsP). Laser thresholds of 5 kA/cm^2 were obtained, while LED efficiencies were on the order of 2%. Incoherent life test over 6000 hours showed no degradation.

17 Key Words (Suggested by Author(s))		18 Distribution Statement
(AlGa)As lasers (InGa)/(AsP) materials III-V semiconductor Short wavelength (AlGa)As lasers	Laser threshold dependence III-V materials inhomogeneity Quaternary semiconductor	Unclassified - Unlimited Subject Category 36

19 Security Classif. (of this report)	20 Security Classif. (of this page)	21 No. of Pages	22 Price*
Unclassified	Unclassified	122	$6.50

* For sale by the National Technical Information Service, Springfield, Virginia 22161

NASA-Langley, 1978

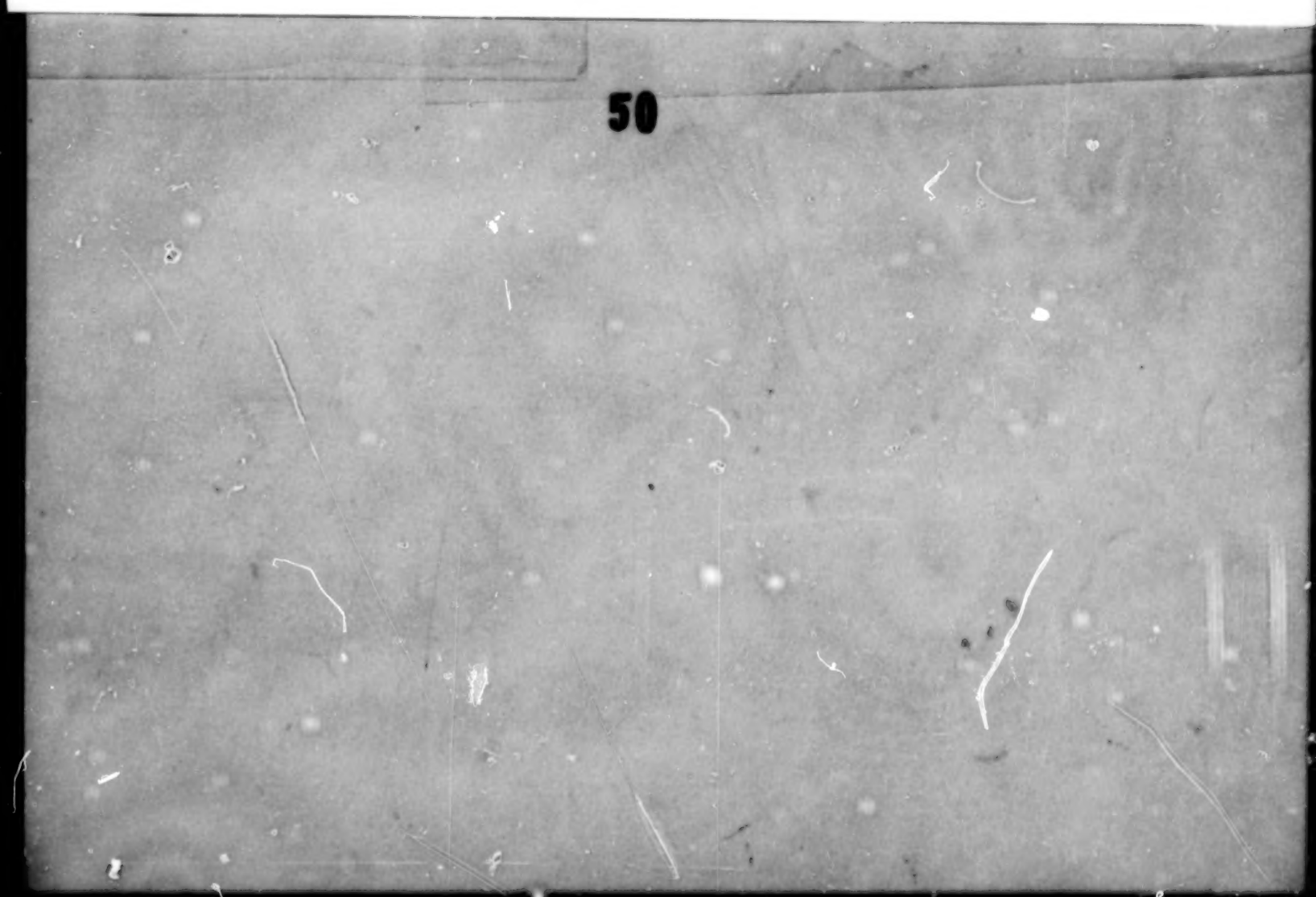
50

END

DEC 12 1978